Spring 2009

Pointwise identification of elastic properties in nonlinear heterogeneous membranes, and application to soft tissues

Xuefeng Zhao
University of Iowa

Recommended Citation

Zhao, Xuefeng. "Pointwise identification of elastic properties in nonlinear heterogeneous membranes, and application to soft tissues." PhD (Doctor of Philosophy) thesis, University of Iowa, 2009.
http://ir.uiowa.edu/etd/222.

POINTWISE IDENTIFICATION OF ELASTIC PROPERTIES IN NONLINEAR HETEROGENEOUS MEMBRANES, AND APPLICATION TO SOFT TISSUES

by

Xuefeng Zhao

An Abstract

Of a thesis proposal submitted in partial fulfillment of the
requirements for the Doctor of Philosophy
degree in Mechanical Engineering
in the Graduate College of
The University of Iowa

May 2009

Thesis Supervisor: Associate Professor Jia Lu

ABSTRACT

Identifying the elastic properties of heterogeneous materials has long been a very challenging problem both theoretically and experimentally. When it comes to biological tissues, this task is even more difficult since biological tissues generally exhibit substantial anisotropic behavior. Moreover, identification is often required to be performed in the service condition of living human tissues and organs, i.e., *in vivo*. Presently, a method capable of performing such tasks is lacking.

The primary goal of this study is to fill this gap by developing a novel experimental method, termed as pointwise identification method (PWIM), for delineating the elastic properties in nonlinear heterogeneous membranes. Fundamentally, the method hinges on a unique feature of membrane equilibrium problems, that is, wall stress can be determined from equilibrium consideration alone (static determinacy). Thanks to the static determinacy, membrane wall stress can be computed numerically by using finite element inverse elastostatics method (FEIEM), and depends minimally on the constitutive model.

In PWIM, an inflation test is conducted for the target membrane with a series of tracking markers, and a series of deformed configurations are recorded by using appropriate motion tracking techniques. Subsequently, the pointwise stress distribution in each deformed configuration can be acquired independently by applying FEIEM, whereas the corresponding strain distribution can be determined from the deformation relative to the reference configuration which contains implicitly the elastic properties of the material. Consequently, the elastic properties at every material point can be extracted by fitting an appropriate constitutive model to the pointwise stress-strain data pairs.

In this work, we have validated the method for nonlinear isotropic and anisotropic materials through numerical simulations on a patient-specific cerebral aneurysm model, developed an experimental system and validated the method experimentally by conducting an inflation test on a rubber balloon, and conducted a test on a rabbit urinary bladder. The situation of the global stress-free configuration being unknown was considered numerically by employing a concept of local stress-free configuration. In this regard, the method holds the promise of identifying *in vivo* the elastic properties of membrane-like living organs, e.g., cerebral aneurysms, using medical images upon the availability of powerful image registration techniques.

Abstract Approved: ______________________________
Thesis Supervisor

____
Title and Department

____
Date

POINTWISE IDENTIFICATION OF ELASTIC PROPERTIES IN NONLINEAR HETEROGENEOUS MEMBRANES, AND APPLICATION TO SOFT TISSUES

by

Xuefeng Zhao

A thesis proposal submitted in partial fulfillment of the
requirements for the Doctor of Philosophy
degree in Mechanical Engineering
in the Graduate College of
The University of Iowa

May 2009

Thesis Supervisor: Associate Professor Jia Lu

Graduate College
The University of Iowa
Iowa City, Iowa

CERTIFICATE OF APPROVAL

PH.D. THESIS

This is to certify that the Ph.D. thesis of

Xuefeng Zhao

has been approved by the Examining Committee for the thesis requirement for the Doctor of Philosophy degree in Mechanical Engineering at the May 2009 graduation.

Thesis Committee: ____________________________________
Jia Lu, Thesis Supervisor

____
Madhavan L. Raghavan

____
Sharif Rahman

____
Colby C. Swan

____
Shaoping Xiao

I dedicate this thesis to my beloved family.

ACKNOWLEDGEMENTS

I would like to express my sincerest gratitude to my advisor, Dr. Jia Lu, for his superb inspiration, encouragements, and guidance in all the time of research for this thesis.

I am deeply indebted to the committee members, Dr. Madhavan L. Raghavan, Dr. Sharif Rahman, Dr. Colby C. Swan, and Dr. Shaoping Xiao, for their technical consultations and valuable suggestions.

I would like to thank Dr. Linda (Xiaolin) Chen at Washington State University, Dr. Salam Ramatalla, Dr. Sultan S. Sultan and Mr. Brian Johns at University of Iowa for their help in exploring motion tracking methods. I also would like to thank my former and current collegues, Dr. Liang Zhang, Dr. Xianlian Zhou, and Ms. Shouhua Hu for their friendship and many helpful discussions.

Sincere thanks must go to my best friends, Dr. Jing Qian and Dr. Yujiang Xiang for their wonderful friendship and support along this journey.

Last but not least, I would like to give my special thanks to my parents and my sister for their endless love and support, and to my wife, Jun, whose love and patience enabled me to complete this work.

ABSTRACT

Identifying the elastic properties of heterogeneous materials has long been a very challenging problem both theoretically and experimentally. When it comes to biological tissues, this task is even more difficult since biological tissues generally exhibit substantial anisotropic behavior. Moreover, identification is often required to be performed in the service condition of living human tissues and organs, i.e., *in vivo*. Presently, a method capable of performing such tasks is lacking.

The primary goal of this study is to fill this gap by developing a novel experimental method, termed as pointwise identification method (PWIM), for delineating the elastic properties in nonlinear heterogeneous membranes. Fundamentally, the method hinges on a unique feature of membrane equilibrium problems, that is, wall stress can be determined from equilibrium consideration alone (static determinacy). Thanks to the static determinacy, membrane wall stress can be computed numerically by using finite element inverse elastostatics method (FEIEM), and depends minimally on the constitutive model.

In PWIM, an inflation test is conducted for the target membrane with a series of tracking markers, and a series of deformed configurations are recorded by using appropriate motion tracking techniques. Subsequently, the pointwise stress distribution in each deformed configuration can be acquired independently by applying FEIEM, whereas the corresponding strain distribution can be determined from the deformation relative to the reference configuration which contains implicitly the elastic properties of the material. Consequently, the elastic properties at every material point can be extracted by fitting an appropriate constitutive model to the pointwise stress-strain data pairs.

In this work, we have validated the method for nonlinear isotropic and anisotropic materials through numerical simulations on a patient-specific cerebral aneurysm model, developed an experimental system and validated the method experimentally by conducting an inflation test on a rubber balloon, and conducted a test on a rabbit urinary bladder. The situation of the global stress-free configuration being unknown was considered numerically by employing a concept of local stress-free configuration. In this regard, the method holds the promise of identifying *in vivo* the elastic properties of membrane-like living organs, e.g., cerebral aneurysms, using medical images upon the availability of powerful image registration techniques.

TABLE OF CONTENTS

LIST OF TABLES ix

LIST OF FIGURES x

CHAPTER

1 INTRODUCTION 1

1.1 Motivation 1
1.2 Objective of the study 3
1.3 Organization of the thesis 5

2 BACKGROUND 9

2.1 Challenges in characterizing soft tissues 9
2.2 Existing material identification methods 12
  2.2.1 Specimen testing 13
  2.2.2 Optimization-based identification methods 16
  2.2.3 Axisymmetric membrane inflation tests 18
2.3 Mechanics of soft tissues 25

3 THEORETICAL FRAMEWORK 30

3.1 Elements of membrane theory 30
  3.1.1 Kinematics 30
  3.1.2 Constitutive theory 32
  3.1.3 Equilibrium equation 36
3.2 Local stress-free configuration 36
3.3 Finite element inverse elastostatics 40
3.4 Inverse elastostatics formulation for membranes 43
3.5 Transforming stress tensor to convected bases 47

4 POINTWISE IDENTIFICATION METHOD 51

4.1 Method 51
  4.1.1 Strain acquisition 54
  4.1.2 Stress acquisition 58
  4.1.3 Constitutive regression 60
4.2 Discussion 61
  4.2.1 Features, speculations 62
  4.2.2 Accuracy issues and solutions 64
  4.2.3 Limitations 65
  4.2.4 Future of *in vivo* identification for biological tissues 65

5 NUMERICAL EXPERIMENTS: ISOTROPIC MATERIAL 68

5.1 Method 68
  5.1.1 Material model and forward analysis 69
  5.1.2 Stress-strain data acquisition 70
  5.1.3 Constitutive regression 71
  5.1.4 Stress gradients 73
5.2 Results 75
  5.2.1 Material insensitivity of membrane stress 75
  5.2.2 Identified elastic parameters 76

6 EXPERIMENTAL VALIDATION: RUBBER BALLOON TEST . . . 85

6.1 Review of rubber elasticity 85
6.2 Method 91
  6.2.1 Finite inflation test for a rubber balloon 91
  6.2.2 Photogrammetric surface reconstruction 94
  6.2.3 Computation of stress 95
  6.2.4 Computation of strain 96
  6.2.5 Isotropy test 97
  6.2.6 Elastic parameter identification 98
  6.2.7 Predictive capability 102
6.3 Results 102
  6.3.1 Reconstructed surfaces and stress results 102
  6.3.2 Stress sensitivity to material model 105
  6.3.3 Isotropy test 107
  6.3.4 Elastic parameter identification 107
  6.3.5 Predictive capability 111
6.4 Discussion 111

7 NUMERICAL EXPERIMENTS: CEREBRAL ANEURYSMS 114

7.1 Introduction 114
7.2 Method 120
  7.2.1 Material model 120
  7.2.2 Forward analysis 123
  7.2.3 Computation of stress 125
  7.2.4 Computation of strain 125
  7.2.5 Elastic parameters identification 126
7.3 Results 130
  7.3.1 Wall stress is insensitive to the material property 130
  7.3.2 Distribution of the identified elastic parameters 133
7.4 Discussion 138

8 EXPERIMENTS: RABBIT URINARY BLADDER 143

8.1 Introduction 143
8.2 Method 144
8.2.1 Materials and experiment 144
8.2.2 Material model 145
8.3 Results 145

9 MATERIAL SENSITIVITY ANALYSIS 148

9.1 Mathematical formulation 149
9.2 Numerical example 154
9.3 Results 156
9.3.1 Linear elements 156
9.3.2 Quadratic elements 159

10 CONCLUSIONS 161

10.1 Summary of major findings 161
10.2 Future work 163

REFERENCES 165

LIST OF TABLES

Table

3.1 Base vectors and metric tensors in different coordinate systems. 49

5.1 The means and standard deviations of identified elasticity parameters of *Model A* and *Model B* *knowing* the reference metric tensor. 84

5.2 The means and standard deviations of identified elasticity parameters of *Model A* and *Model B* *without knowing* the reference metric tensor. . . . 84

6.1 Summary of phenomenological constitutive relations of rubber-like materials. 92

6.2 The identities and corresponding pressure values of the deformed configurations. 103

6.3 The identified parameters α_i and μ_i for the Ogden model at a selected point. 108

6.4 Ranges, means, and standard deviations of the identified elasticity parameters. 110

7.1 Means, minimums and maximums of the identification errors of the *pointwise* identification by assuming the fiber orientation is *known.* 134

7.2 Means, minimums and maximums of the identification errors of the *pointwise* identification by assuming the fiber orientation is *unknown.* 136

7.3 Means, minimums and maximums of the identification errors of the *regionwise* identification by assuming the fiber orientation is *known.* 137

9.1 Means, minimums and maximums of the stress sensitivity with respect to μ_1 using linear elements. 158

9.2 Means, minimums and maximums of the stress sensitivity with respect to μ_2 using linear elements. 158

9.3 Means, minimums and maximums of the stress sensitivity with respect to μ_1 using quadratic elements. 159

9.4 Means, minimums and maximums of the stress sensitivity with respect to μ_2 using quadratic elements. 159

LIST OF FIGURES

Figure

2.1 Deformed and undeformed meridian arc of an axisymmetric membrane. . 19

3.1 Schematic illustration of the kinematic map and base vectors. 31

3.2 Schematic illustration of the kinematic map and the local stress-free configuration. 37

4.1 Flowchart of PWIM. 53

5.1 Undeformed geometry and finite element mesh of the membrane sac: (a) Perspective view; (b) Bottom view. 69

5.2 The distribution of principal stress resultants in the membrane sac: (a) t_1; (b) t_2. 76

5.3 The percentage difference of principal stress resultants under the change of elasticity parameters. Upper row: Increasing both parameters μ_1 and μ_2 by 10 times: (a) t_1, (b) t_2; Lower row: Increasing both parameters μ_1 and μ_2 by 100 times: (c) t_1, (d) t_2. 77

5.4 Identified elasticity parameters of *Model A* knowing the reference metric: (a) μ_1, (b) μ_2. 78

5.5 Absolute values of the relative error (in percentage) between identified elasticity parameters and true parameters of *Model A* knowing the reference metric: (a) μ_1, (b) μ_2. 79

5.6 Identified elasticity parameters of *Model A* without knowing the reference metric: (a) μ_1, (b) μ_2. 80

5.7 Absolute values of the relative error (in percentage) between identified elasticity parameters and true parameters of *Model A* without knowing the reference metric: (a) μ_1, (b) μ_2. 80

5.8 Identified elasticity parameters of *Model B* knowing the reference metric: (a) ν_1, (b) ν_2. 81

5.9 Identified elasticity parameters of *Model B* without knowing the reference metric: (a) ν_1, (b) ν_2. 82

5.10 Comparison between the “experimental” tension invariants and the predictions of *Model B*: (a) J_1, (b) J_2. 83

6.1 Schematic illustration of the experimental system. 93

6.2 A photo of the rubber balloon used in the process of 3-D geometry reconstruction. 104

6.3 Reconstructed meshes of the deformed configurations. 104

6.4 Distribution of principal tensions in deformed configuration 13: (a) t_1, (b) t_2. 105

6.5 The percentage difference of principal tensions under the change of elasticity parameters. Upper row: Increasing both parameters μ_1 and μ_2 to 10 times: (a) t_1, (b) t_2; Lower row: Keeping μ_1 unchanged and increasing μ_2 to 5 times: (c) t_1, (d) t_2. 106

6.6 The distribution of the co-axiality indicator ε in selected configurations: (a) Configuration 1; (b) Configuration 13. Both figures were scaled to fit the canvas for clarity. 108

6.7 Identified elasticity parameters of the Ogden model: (a) μ_1, (b) μ_2, (c) μ_3. 109

6.8 Distribution of the ratio of μ_1 to μ_2. 110

6.9 Comparison between the experimental and the modeled tension curves: (a) t_1; (b) t_2. 112

6.10 Comparison between the deformed configuration computed from finite element method using the identified elastic parameters and the experimentally measured configuration. (a) Thin gray mesh: experimental (whole domain); Thick black mesh: finite element modeled (boundary-effect-free region); (b) Distribution of the position error $e = \frac{\|\mathbf{x}-\hat{\mathbf{x}}\|}{L}$. 113

7.1 Schematic of the validation procedure. 119

7.2 The initial configuration (shaded) a deformed configuration under a pressure of 110 mmHg (mesh) of the cerebral aneurysm sac. 120

7.3 Realistic (assumed) distribution of the elastic parameter k_1. 121

7.4 The distribution of fiber directions at the fundus. 124

7.5 Distribution of the principal stresses on the deformed configuration under the highest pressure (110 mmHg): (a) t_1, (b) t_2. 131

7.6 The absolute percentage difference between the principal stresses computed from inverse and forward FEA: (a) Error(t_1), (b) Error(t_2). 132

7.7 Distribution of the first principal stretch. 132

7.8 Distribution of the identified elastic parameters from pointwise identification by assuming the fiber directions are known: (a) k_1, (b) k_4, (c) k_6. . . 134

7.9 Distribution of the identification errors of the elastic parameters from pointwise identification by assuming the fiber directions are known: (a) Error(k_1), (b) Error(k_4), (c) Error (k_6). 135

7.10 Distribution of identified elastic parameters from pointwise identification by assuming the fiber directions are unknown: (a) k_1, (b) k_4, (c) k_6. . . . 136

7.11 Distribution of identified elastic parameters from "region-wise" identification by assuming the fiber directions are known: (a) k_1, (b) k_4, (c) k_6. . . 137

7.12 Distribution of the identified elastic parameters by assuming the stress-free configuration is unknown: (a) k_1, (b) k_4, (c) k_6. 138

7.13 Distribution of the identified error by assuming the stress-free configuration is unknown: (a) Error(k_1), (b) Error(k_4), (c) Error(k_6). 139

8.1 A photo of the inflated rabbit urinary bladder used in the process of 3-D geometry reconstruction. 146

8.2 Distribution of the identified elastic parameters of the rabbit urinary bladder: (a) k_4, (b) k_6. 147

8.3 Comparison between the experimental and modeled stress invariants-strain invariants curves. 147

9.1 Sensitivity of the stress components with respect to elastic parameter μ_1 in forward analysis: (a) t^{11}, (b) t^{22}, (c)t^{12}. 157

9.2 Sensitivity of the stress components with respect to elastic parameter μ_2 in forward analysis: (a) t^{11}, (b) t^{22}, (c)t^{12}. 157

9.3 Sensitivity of the stress components with respect to elastic parameter μ_1 in inverse analysis: (a) t^{11}, (b) t^{22}, (c)t^{12}. 157

9.4 Sensitivity of the stress components with respect to elastic parameter μ_2 in inverse analysis: (a) t^{11}, (b) t^{22}, (c)t^{12}. 158

CHAPTER 1
INTRODUCTION

1.1 Motivation

In the last several decades, biomechanics has received much attention and enormous research effort. An important branch of biomechanics is to derive constitutive models for biological tissues from experimental observation, and further use these models to predict the mechanical behavior in different situations. Toward this goal, an indispensable step is the identification of constitutive model parameters for certain tissues. Briefly, such an identification process takes as input the experimentally observed material response and conduct numerical computations using varying elastic parameters until the discrepancy between the modeled and experimental responses reaches its local minimum. The elastic parameters rendering such a minimum are considered to be the optimum parameters which reflect the realistic elastic behavior of the material.

Various approaches for identifying the elastic properties of the materials have been developed. Prominent examples include controlled specimen testing, optimization-based identification methods (also known as finite element updating methods), and axisymmetric membrane inflation tests. These methods have their respective advantages and limitations. Controlled specimen testing works directly on stress and strain data, and is versatile for a variety of constitutive behaviors (elastic, viscoelastic, and plastic), but is destructive. The directness allows for separately observing the material response and then selecting appropriate constitutive models, and subsequently identifying elastic parameters of the constitutive models. However, the destructiveness prevents it from being the basis for *in vivo* testing for living tissues.

Optimization-based material identification methods work by coupling model analysis (e.g., by finite element method (FEM)) with parameter regression. The searching of the optimum elastic parameters is driven by the nonlinear regression algorithm based on an objective function which is usually the squared difference between the modeled responses by numerical simulations and the experimentally observed responses. In contrast to specimen testing, optimization-based identification methods are indirect. However, a noteworthy attribute of this type of methods is that they can be rendered non-destructive. These methods have been widely adopted in biomechanical applications [126, 127, 77].

Another type of material identification methods are axisymmetric inflation tests for thin membranes. In axisymmetric membranes, the principal directions of stress and strain are aligned with the meridian and circumferential directions. The principal stretches can be measured from the profiles of the deforming membrane. Moreover, the principal stresses depend only on the deformed shape, independent of the material in question, and can be expressed as analytical functions of the transmural pressure and principal curvatures which can be measured from experiments. By fitting the functions to the experimental data of principal stresses and stretches, the elastic parameters can be identified for specific constitutive models. Axisymmetric membrane inflation tests are direct and non-destructive, however, they are not applicable to membranes of general shape as the definition implies.

It should be noted that none of the aforementioned methods can delineate the elastic property distribution of heterogeneous materials effectively and accurately. The latest development on biaxial test has pushed the size of specimen to the order of a few squared millimeters [122], however, the specimen is still at a finite size. The optimization-based methods can only provide average properties in the test region. It is practically impossible to obtain the distribution of heterogeneous elastic properties. Therefore, in order to characterize accurately the elastic properties of heterogeneous materials, more effective methods are in demand.

1.2 Objective of the study

The objective of this study is to develop a novel experimental method which can delineate the distributive elastic properties in nonlinear, anisotropic, and heterogeneous membrane structures and apply it to thin-walled biological tissues. The ultimate goal is to extract accurate information on the regional material property of diseased human tissues or organs, and to aid disease diagnosis.

Thanks to the static determinacy of a pressurized membrane in equilibrium, membrane wall stress is independent of material property. If we can obtain the pointwise distribution of stress and strain in a series of deformed configurations of a membrane, the elastic property distribution of the membrane can be acquired by identifying the constitutive parameters point by point. Based on this thinking, we set further to generalize the membrane inflation test and make it applicable to membrane structures of arbitrary shape. We term this method as *pointwise identification method (PWIM)*. Towards this goal, we will first seek a method that can be used to determine the wall stress distribution in a deformed configuration without knowing the realistic material property. Then, we will devise a method to obtain the strain distribution in multiple deformed configurations relative to a reference configuration. Finally, a nonlinear regression algorithm will be chosen to conduct elastic parameter identification using the pointwise stress-strain data.

To build up the theoretical ground for the pointwise identification method, we will first revisit the membrane equilibrium and examine the static determinacy of membrane wall stress. Then, we will introduce the finite element inverse elastostatics method (FEIEM) which serves the purpose of determining the stress distribution without knowing the actual material property in question. After constructing the basic procedure of the pointwise identification method, we will validate the method. Firstly, numerical experiments will be used, in which an inflation experiment is simulated by forward finite element analysis on a cerebral aneurysm sac model of predefined elastic property distribution. Since we know the actual elastic property which we presumably assigned to the membrane, we are able to compare the identified one with it to evaluate if the method is valid and effective. Secondly, we will conduct physical experiments on a rubber balloon which is legitimate to be modeled as a membrane, and use the proposed method to identify its elastic property. The identified elastic parameters will be input into a forward finite element analysis to check if they can be used to predict a deformed configuration. This process serves as the validation since we do not know the actual values of the constitutive parameters, and there are not data from other experiments to compare with.

Another major objective is to validate the method for anisotropic materials since the ultimate application of the method is to identify the elastic properties in biological tissues which are generally anisotropic. Due to the extensive effort required to reconstruct the microstructure of biological tissues, the current validation will be limited to numerical experiments. The fiber orientation and material heterogeneity of a cerebral aneurysm model will be predefined to exhibit certain pattern. An inflation process will be simulated followed by elastic parameter identification using PWIM. A very important issue in characterizing anisotropic materials is whether the fiber orientation can be identified from biaxial stress-strain data. We will address that in this work. In addition, the feasibility of *in vivo* identification will be tested by assuming the stress-free configuration is unknown and conducting elastic parameter identification with the aid of local stress-free configuration concept.

In order to demonstrate the feasibility of whole-organ elastic property identification, an inflation test on a rabbit urinary bladder will be conducted. Its elastic property distribution will be identified by making certain assumptions on the fiber orientation. Again, due to the limited experimental capability, validation will be conducted systematically in the future.

1.3 Organization of the thesis

The thesis is organized as follows. Chapter 2 gives an overview of the challenges in characterizing biological tissues and the existing methods for elastic property identification, including specimen testing, optimization-based methods and axisymmetric inflation tests, and their respective advantages and drawbacks as well. A brief review about mechanics of soft tissues is also given in this chapter.

Chapter 3 introduces the theoretical basis of the pointwise identification method. First, the fundamental membrane theory is presented, including kinematics, constitutive theory and equilibrium equation. The equilibrium equation entails the static determinacy of membrane stress which is the basis of the pointwise identification method. Subsequently, the concept of local stress-free configuration and the formulation for isotropic and anisotropic materials are presented. With this concept, the elastic property can still be identified even if the global stress-free configuration is not available, which forms the theoretical basis for *in vivo* elastic property identification. Next, the finite element inverse elastostatics method (FEIEM) and the formulation for membranes are introduced. This method is essentially the cornerstone of the pointwise identification method. Finally, the formulation of transforming the stress tensor to be under convected basis is presented. This is an important step in elastic parameter identification.

Chapter 4 describes the procedure of the pointwise identification method which involves three steps, i.e., strain data acquisition, stress data acquisition and constitutive regression. The advantages and limitations of the method is also discussed.

Chapter 5 presents the validation of the method for isotropic material using a numerical experiment on a cerebral aneurysm of predefined homogeneous material property. Stress sensitivity analysis in inverse stress computation is conducted by varying drastically the elastic parameters in FEIEM, and a boundary-effect-free region is determined. The elastic parameters of a constitutive model different than the assumed one are identified. The distribution of the identified parameters is compared with the assumed homogeneity to evaluate the effectiveness of the method. The same procedure is followed for the situation of the global stress-free configuration being unknown.

Chapter 6 introduces the experimental system designed for PWIM and presents experimental validation using a finite inflation test on a rubber balloon. The rubber balloon is inflated to a series of pressure levels, and the stress-strain data in the deformed configurations are obtained. By observing the stress-strain relation, we choose Ogden's strain-energy function to model the rubber material, and the elastic parameters in the boundary-effect-free region are identified. Material isotropy is verified by testing a universal relation for isotropic materials. The predictive capability of the model and its identified parameters is tested using a configuration which is not used in the identification.

Chapter 7 presents the validation of the method for anisotropic materials using a numerical experiment on a cerebral aneurysm of heterogeneous material property. The procedure is the same as the isotropic case presented in Chapter 5 except that the material anisotropy is assumed. The two families of collagen fibers are assumed to be perpendicular to each other, which renders material orthotropy. The elastic parameters of the anisotropic model are identified under the conditions of known fiber orientation, unknown fiber orientation and unknown global stress-free configuration, respectively. The respective identification error is evaluated.

Chapter 8 describes the anisotropic elastic property identification for a rabbit urinary bladder. We assume the two families of collagen fibers are distributed along the meridian and circumferential directions of the bladder surface, respectively. The strain-energy function proposed by Holzapfel's group is utilized to model the elastic behavior of the bladder wall. The stress distribution in deformed bladder is computed by FEIEM using an isotropic neo-Hookean model.

Chapter 9 presents sensitivity analysis for membrane stress with respect to material property using Direct Differential Method (DDM) for forward and inverse finite element analyses. Low sensitivity of wall stress with respect to material property in inverse analysis reveals again the static determinacy of membrane equilibrium. In order to describe the membrane surface more accurately, 9-node quadratic elements are also used to compute the sensitivity.

Conclusions and future work are presented in Chapter 10.

CHAPTER 2
BACKGROUND

2.1 Challenges in characterizing soft tissues

Thanks to the fast development of powerful numerical methods, such as finite element method, computational fluid mechanics, etc., stress analysis has become a very helpful tool in modeling the mechanical behavior of biological tissues and organs. Nevertheless, there are still quite a number of challenges that researchers are facing due to the intrinsic characteristics of biological tissues. In this section, we will review the challenges pertinent to the work of this thesis.

When conducting stress analysis, three pieces of information must be available, i.e., the stress-free configuration, a constitutive law which is represented with respect to the stress-free configuration, and the specific value of the parameters in the constitutive law. For engineering materials, numerous elastic constitutive models have been proposed by experimenting the material and observing the load-deformation relation. These models are either phenomenological which are based on the macroscopic behavior of the materials regardless of their complex microstructure, or structural which take into account the microstructure and the different properties of the constituent materials. A constitutive model is expected to describe the properties of certain type or class of materials. The value of the model parameters for different materials can be identified by fitting the model to certain experimental data if any material is of interest. This problem is an inverse problem, which is usually termed as *elastic property identification* or *material parameter identification*.

However, for biological tissues, elastic property identification is not a trivial task. There are several reasons. Firstly, the mechanical properties of biological tissues are generally nonlinear, anisotropic and heterogeneous over finite strains. Due to material anisotropy, the elastic responses are different along different directions, and shear stress generally exists. Therefore, an experimental protocol which can measure biaxial loads (including both extension and shear) is needed. However, this requirement is quite stringent for experimentalists. Material heterogeneity is extremely hard to characterize because stress field cannot be measured for most structures (excluding statically determinate structures) without knowing the actual material property. Secondly, the global stress-free configuration of biological tissue is not easy or even impossible to obtain physically, e.g., residually stressed tissues. Thirdly, elastic property identification is often required to be conducted non-destructively, *in vivo*, and subject-specifically.

Biological tissues have very complex microstructures. Take blood vessels as an example. The vessel wall is composed of three consecutive layers from the inner to the outer surfaces, i.e., the intima, media and adventitia. Their microstructures are distinct from each other, which present heterogeneous material property. In addition, along the axial and circumferential directions, the material property may be very different due to microstructural difference, growth, and remodeling. A sharp characterization of pointwise property requires one know the stress-strain data at the point of interest. Nowadays, some full-field measurement techniques are available to measure the strain field, e.g., digital image correlation and speckle interferometry method. But there is no general method to measure the pointwise stress.

More often than not, one assumes that the stress-free configuration is the configuration where external load is absent. However, this is not true for some material bodies, e.g., biological tissues and organs. In the body of a living creature, the organs and tissues are always under physiological pressure, and the load-free configuration is never reached. Even though the load is eliminated after the organs and tissues are taken out of the body, residual stress still exists, e.g., in the heart and arteries. The source of residual stress is believed to be non-uniform growth, resorption and remodeling [38, 130, 131], and the driving force of residual stresses in the heart and arteries is to minimize the peak stresses experienced by these tissues in vivo [40, 84, 22]. The stress-free configuration of such residually stressed bodies cannot be obtained unless the residual stress is relieved completely, generally by a destructive manner, e.g. by cutting the material body into separate pieces. There has been extensive effort in modeling residually stressed bodies. Two major routes have received considerable attentions. One is to derive constitutive equations which include the effect of residual stress and the material properties in the stress-free configuration [57, 72, 58]. The mechanical response in an arbitrary deformed configuration can then be computed from these constitutive equations and the deformation gradient out of the residually stressed configuration. This method is not practically feasible if the constitutive equation is complex. The other one is to identify the material properties and the characteristic (typically topological) parameters of the stress-free configuration from a series of loaded configurations and, then use these parameters to predict other deformed configurations [162, 139, 138, 106, 137, 180].

A second example is a membrane structure that collapses when external load (transmural pressure) is removed. Therefore, for a membrane structure, there is no unique stress free configuration which is attainable from physical experiments. In this work, we are going to introduce a *local stress-free configuration* at a material point on a membrane which is parameterized by a Rimannian metric tensor, and then identify the elastic property and the components of the metric tensor simultaneously from pointwise stress-strain data in multiple deformed configurations. It is worth mentioning that this concept can be applied to residually stressed bodies, which is not the objective of this work because membranes sustain no residual stress.

2.2 Existing material identification methods

Identification of elastic properties is an inverse problem which takes certain experimentally measured mechanical responses as reference, subsequently applies certain mechanical laws and finally output the parameters of the laws. Since this subject is involved in almost all the physical problems, e.g. plasticity, viscoelasticity, etc., it is impossible and unnecessary to include all the aspects in this review. Here, only the identification methods for elastic properties from purely mechanical tests are touched upon. In what follows, the existing material identification methods and relevant works, in particular for the identification of biological tissues, are introduced, and their advantages and limitations are discussed.

2.2.1 Specimen testing

The most well-known and straightforward method for material identification is controlled specimen testing. Briefly, a specimen with certain geometry is prepared by cutting from a large piece of material or directly molding with the material. Then the specimen is mounted onto a specialized test device and loaded. The load and deformation of a small central region distanced enough from the ends of the specimen are recorded, from which one can derive the stress-strain history during the deformation. By observing the trend of the stress-strain curve, an appropriate constitutive model may be chosen and the realistic elastic parameters for the tested material may then be identified by fitting the discrete experimental data with the model.

In specimen testing, boundary loads are carefully applied so that the stress and strain in the central region of the specimen remain approximately uniform during the entire course of loading. Due to the homogeneity, the stress can be computed from the applied boundary traction without knowing the material constitutive equation in question. However, the implication of assuming homogeneous stress and strain in the test region is that the identified elastic parameters are the averaged parameters over the region. If the material is intrinsically homogeneous or nearly so in the macro sense, or only averaged material properties are sought, specimen testing is considered to be valid and effective. By design, specimen testing is a *direct* method where the analytical load-deformation or stress-strain relation is contained in the experimental data. The constitutive relation can be directly observed from the experimental data, and hence the elastic parameters can be identified directly by utilizing regression algorithms.

The most common specimen testing methods include uniaxial extension, biaxial extension, and such. Although uniaxial extension tests are widely used in material science, e.g., in determining the elastic property of polymer materials or metals, the load protocol is not sufficient in characterizing the multi-dimensional behavior of natural biological tissues and tissue-derived soft biomaterials in physiological conditions. The essential reason for this is that the “experimental paths” of uniaxial extension tests with respect to the in-plane strain components do not cover the physiological domain of biological tissues [59]. Since uniaxial extension provides experimental data only for a small domain in the strain space, fitting of multi-dimensional constitutive models to the data may lead to ill-conditioned equations, slow convergence rates, and non-unique solutions. In other words, different sets of constitutive parameters may provide equally good representations of uniaxial data, but predict very different material response for physiological loading conditions [59].

To overcome such difficulties, one frequently employs multi-axial extension tests which simulate the physiological condition more accurately. For incompressible thin biological tissues, planar biaxial testing allows for a two-dimensional stress state that is sufficient in characterizing the elastomechanical behaviors. The original development of biaxial extension testing was initiated by Treloar [153] and Rivlin and Saunders [114] in coping with rubber elasticity problems. Treloar [153] pioneered techniques to apply two independently variable strains in two perpendicular directions with simultaneous measurement of stresses [121]. However, in Treloar’s device the axial stretch ratios λ_1 and λ_2 cannot be controlled separately. This experimental limitation did not facilitate precise determination of the form of W and its derivatives, $\partial W/\partial I_1$ and $\partial W/\partial I_2$. In 1951, Rivlin developed a modified biaxial device that allowed for applying biaxial loads to rubber sheets and more precise experimental control. Using this device, Rivlin developed an integrated theoretical-experimental methodology in which the form of W could be derived and evaluated directly from multi-axial experimental data [121].

The earliest investigations into developing and utilizing biaxial testing to identify the elastic properties of biological tissue were initiated by Lanir and Fung in 1774 [80, 81] as they studied the elastic properties of rabbit skin. The ensuing investigations into the elastic property characterization of a much broader range of soft tissues, including arterial walls, heart valves, pericardium, myocardium, abdominal aortic aneurysms, cerebral aneurysms, cornea, etc., appear to be prosperous and endless.

Although specimen testing has been extensively relied upon in elastic property identification in both material science and biomedical engineering due to its simplicity and directness, a primary limitation is the *destructiveness*. This may confine its applicability in certain situations where the testing process cannot be controlled by the tester. For example, a reliable identification of the elastic properties of biological tissues usually desires the testing be conducted in their living status, or at least in the intact state. In this regard, it is not reasonable to cut a piece of tissue. Moreover, if the material is highly heterogeneous and the distribution of the material heterogeneity needs to be sought, specimen testing is not effective.

2.2.2 Optimization-based identification methods

As mentioned above, in some situations, the experimental condition cannot be controlled, or non-destructiveness is required when the material needs to be characterized in its service condition. In such cases, specimen testing is not applicable. One can employ an alternative, *optimization-based identification methods*, to conduct elastic property identification. Briefly, optimization-based identification methods couple a forward numerical method (e.g., finite element method (FEM)) with a nonlinear regression algorithm. The searching of the realistic elastic parameters is driven by the nonlinear regression algorithm based on an objective function which is usually the squared difference between the modeled responses by the forward numerical simulation and the experimentally observed response. In the literature, optimization-based identification methods are often termed *inverse finite element methods* due to the common usage of finite element methods as the numerical simulation tool. Here, we prefer not to use this name in order for avoiding unnecessary confusion between this method and the *finite element inverse elastostatics methods* among unfamiliar readers.

These methods are based on an *indirect* approach; that is, the constitutive law is not contained directly in the experimental data, but implied in the modeling. In other words, the explicit relationship between the stress and strain is not derived directly form the experimental data, but estimated from the predicted model response. To supplement the data which contain the constitutive relation, a forward numerical simulation needs to be performed using the actual loading condition and an assumed constitutive model. The best-fit parameters are obtained by progressively minimizing the difference between the model prediction (of, say, displacements at some positions) and the physical measurement.

Due to the fact of coupling numerical field solution and constitutive regression, the field problem needs to be solved over and over again as the regression iteration proceeds, until the optimal parameters are found. Therefore, both aspects being usually computationally expensive, extensive computation effort is needed, especially for complex problems. Moreover, the complex coupling makes it difficult to pinpoint the source if some errors occur during the identification. Most importantly, in these methods, one usually assumes the material is homogeneous over the whole domain. Or alternatively, one needs to identify multiple sets of parameters simultaneously at multiple points if material heterogeneity needs to be characterized. This may increase the computational effect enormously, and even worse, a unique combination of parameters may not be determined.

The optimization-based methods were originally proposed by Kavanagh and Clough [74], and further developed by Iding et al. [69] and Kyriacou et al. [79]. Kyriacou et al. [79] utilized this method to characterize the material parameter of neo-Hookean rubber membranes using axisymmetric and nonaxisymmetric finite inflation experiments.

Considering the aforementioned difficulties in dealing with heterogeneous material properties encountered by optimization-based identification methods, Seshaiyer and Humphrey [127] proposed a *sub-domain inverse finite element method* which is an adaptation of general optimization-based identification methods using FEM toward a sub-domain of the whole domain, typically composed of several interconnected finite elements. With this method, the material is assumed to be homogeneous within a small region, and so are the stress and strain. This sub-domain approach avoids difficulties in measuring all the boundary conditions for the entire domain, and much smaller forward FE analysis is needed. Thus it is computationally much more effective than the global counterpart. Most importantly, the region in which material homogeneity is assumed is reduced significantly. This allows one to characterize heterogeneous material more accurately. However, what this method provides is still a local average of the elastic properties. It also inherits afore-mentioned other limitations of the methods.

In summary, for both specimen testing and optimization-based identification methods, a primary limitation is the premise of global or local material homogeneity. The reason for this is the lack of an effective experimental method for determining pointwise stress-strain data in a heterogeneous material body under load.

2.2.3 Axisymmetric membrane inflation tests

A number of researchers have investigated the problem of *axisymmetric* membrane inflation, and employed it to identify the elastic properties of rubber-like materials and biological soft tissues. The method is designed for axisymmetric membranes because the principal directions of stress and strain are aligned with the meridian and circumferential directions, and thus the principal stretches are easy to measure.

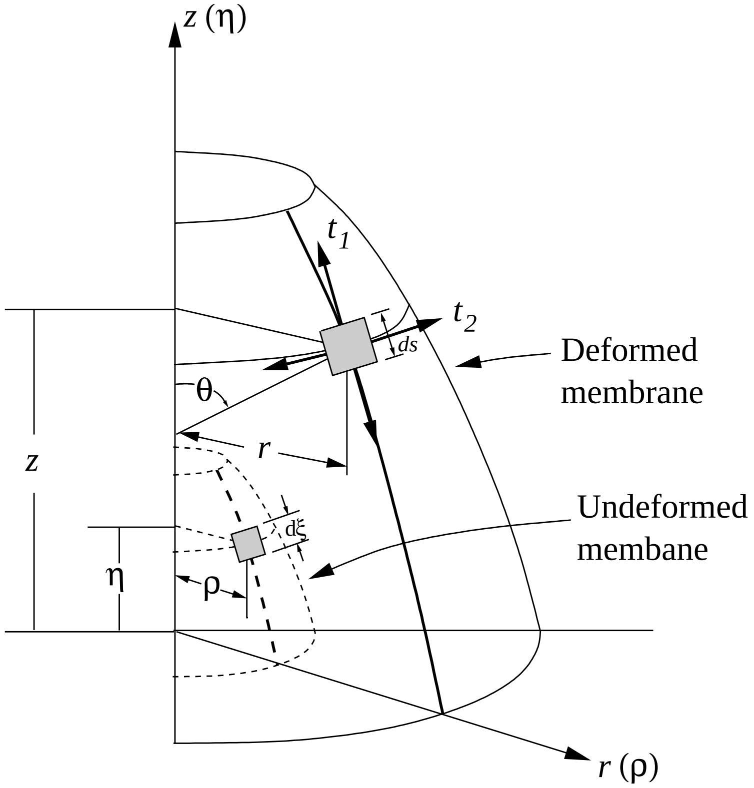

Figure 2.1: Deformed and undeformed meridian arc of an axisymmetric membrane.

Moreover, the principal stresses depend only on the deformed shape, independent of the material in question, and can be expressed as analytical functions of internal pressure and principal curvatures which can be measured from experiments. To name a few works, there have been Treloar [151], Adkins and Rivlin [2], Green and Adkins [48], Klingbeil and Shield [76], Hart-Smith and Crisp [53], Foster [37], Yang and Feng [176], Schmidt and Carley [123], Wineman et al. [173], Vaughan [164] and Hsu [62, 61].

Since the current work spins from the inflation test, it is worthwhile revisiting the axisymmetric membrane inflation problem. Here we follow Klingbeil and

Shield [76]. Figure 2.1 illustrates the undeformed and deformed profiles of an axisymmetric membrane. Its geometry can be described by polar coordinates. In a coordinate plane of constant θ, let $(\rho,\ \eta)$ be a point of the undeformed membrane. The point is displaced to a new position $(r,\ z)$ in the same coordinate plane. The undeformed profile is represented by the relation $\eta = \eta(\rho)$. The objective of the problem is to seek the deformed profile in terms of $r(\rho)$ and $z(\rho)$ under a given load condition.

For the geometry of the surface after deformation, we have

$$\frac{\mathrm{d}r}{\mathrm{d}s} = \cos\theta, \quad \frac{\mathrm{d}z}{\mathrm{d}s} = -\sin\theta, \tag{2.1}$$

with the principal curvatures κ_1 and κ_2 being given by

$$\begin{aligned} \kappa_1 &= \frac{\mathrm{d}\theta}{\mathrm{d}s}, \\ \kappa_2 &= \frac{\sin\theta}{r}. \end{aligned} \tag{2.2}$$

The subscripts (1,2) used here and in the following to denote directions of meridian and circumferential respectively. Implied by Equations (2.1) to (2.2) is the familiar relation

$$\kappa_1 = \frac{d}{dr}\left(r\kappa_2\right). \tag{2.3}$$

Due to axisymmetry, the only non-zero components of stress resultant $\mathbf{t}$ and deformation gradient $\mathbf{F}$, relative to the meridian and circumferential directions, are the principal components. The principal stretch ratios in the meridian and circumferential directions are here denoted by λ_1 and λ_2, respectively, and are defined by

$$\begin{aligned} \lambda_1 &= \frac{\mathrm{d}s}{\mathrm{d}\xi}, \\ \lambda_2 &= \frac{r}{\rho}, \end{aligned} \tag{2.4}$$

where $d\xi$ and ds are the infinitesimal undeformed and deformed meridian arc lengths. The third principal stretch ratio λ_3, for directions normal to the deformed membrane surface, is related to λ_1 and λ_2 through the incompressibility condition

$$\lambda_1\lambda_2\lambda_3 = 1. \tag{2.5}$$

For membranes undergoing only quasi-static normal pressure p, the governing differential equations are

$$\begin{aligned} &\frac{d}{dr}\left(rt_1\right) = t_2, \\ &\kappa_1 t_1 + \kappa_2 t_2 = p \end{aligned} \tag{2.6}$$

where t_1 and t_2 are principal stress resultants.

It remains to relate the principal stress resultants t_1 and t_2 to the principal stretch ratios λ_1 and λ_2. For an incompressible isotropic material these relations are

$$\begin{aligned} t_1 &= \frac{2H}{\lambda_1\lambda_2}\left(\lambda_1^2 - \frac{1}{\lambda_1^2\lambda_2^2}\right)\left(\frac{\partial W}{\partial I_1} + \lambda_2^2\frac{\partial W}{\partial I_2}\right), \\ t_2 &= \frac{2H}{\lambda_1\lambda_2}\left(\lambda_2^2 - \frac{1}{\lambda_1^2\lambda_2^2}\right)\left(\frac{\partial W}{\partial I_1} + \lambda_1^2\frac{\partial W}{\partial I_2}\right), \end{aligned} \tag{2.7}$$

where $W = W(I_1, I_2)$ is the strain energy function for the material,

$$\begin{aligned} I_1 &= \lambda_1^2 + \lambda_2^2 + \frac{1}{\lambda_1^2 \lambda_2^2}, \\ I_2 &= \frac{1}{\lambda_1^2} + \frac{1}{\lambda_2^2} + \lambda_1^2 \lambda_2^2 \end{aligned} \tag{2.8}$$

are respectively the first and second strain invariants, and H is the thickness of the undeformed membrane.

Treloar [151] was the first one to compute the principal strains over an axisymmetric rubber membrane. He used a moving microscope to record the motion of several points aligned on the diameter of the membrane, and compute the principal strains using analytical formula. Adkins and Rivlin [2] employed the Mooney form (Equation (6.4)) and a Taylor's series approach to compute the deformed profiles of a pressurized, clamped, initially flat, circular rubber sheet, and compared them with the experimental profiles measured by Treloar [151]. Agreement was found to be good at low inflation degrees whereas less so at higher inflation degrees (extension ratio greater than 4). It suggested the limited validity of the Mooney form of W in representing the behavior of pure gum rubber vulcanizates at intermediate and high extensions [76]. It was shown in [2] that the solutions for high values of λ become extremely sensitive to the higher derivatives of the strain energy function $W(I_1, I_2)$ with respect to its arguments I_1 and I_2. Hence, for a pure gum rubber material, the inflated diaphragm problem, in conjunction with the available experimental results and a numerical technique to solve the inflation problem, offers an indirect means for further investigations on the nature of W at high extensions and, moreover, provides a stringent test for those forms of the strain-energy function already existing in the literature [76].

Considering the limited validity of the Mooney form, Klingbeil and Shield [76] used the validity of another form of the strain-energy function in terms of principal stretch ratios proposed by Carmichael and Holdaway [15] to model pure gum vulcanizates. They found that good fit to Treloar's experimental data could not be reached if using the material parameters obtained by Carmichael and Holdaway. Hence they adjusted the parameters and reached very agreement between the computational and experimental results.

Rivlin and Saunders [114] first showed that specific forms of response functions for nonlinear, incompressible, hyperelastic, isotropic solids can be determined directly from axisymmetric membrane inflation test.

The work by Hsu et al. [62] was the first investigation into the possibility of determining the response functions of an axisymmetric membrane directly from the experimental data of an inflation test. They performed a numerical experiment of inflation test for a circular clamped flat membrane using a constitutive model (STZC material) originally developed for red cell membranes by Skalak et al. [132], of which the strain energy function is

$$w = \frac{c_1}{8}\left(I_1^2 + 2I_1 - 2I_2 + \Gamma I_2^2\right) \tag{2.9}$$

where w is the 2D strain energy function, $\Gamma = c_2/c_1$, c_1 and c_2 are material parameters,

$I_1 = 2(E_{11} + E_{22})$, and $I_2 = 4E_{11}E_{22} + 2(E_{11} + E_{22})$, E_{11} and E_{22} are Green strain tensor components.

The two response functions are defined by

$$w_{11} = \frac{\partial w}{\partial E_{11}} = \frac{\lambda_2}{\lambda_1} t_1, \quad w_{22} = \frac{\partial w}{\partial E_{22}} = \frac{\lambda_1}{\lambda_2} t_2. \tag{2.10}$$

Sampling "measured" data at three locations where the dimensionless reference radial coordinate $\rho = 0, 0.5, 1$, i.e. the pole, half of the radius, the base, respectively, they were able to determine the dependence of the response functions w_{11} and w_{22} with respect to the strain components E_{11} and E_{22} for three different load protocols, i.e. equibiaxial, proportional and strip biaxial stretching tests.

Membrane inflation tests provide rich multiaxial experimental protocols, which allow one to investigate different mechanical behaviors [173, 62]. However, these tests are only applicable to axisymmetric membranes as designed. A secondary limitation of membrane inflation tests is the inability to separately control the two principal strains or stresses, i.e. varying one and maintaining another. This confines the possibility of observing the individual roles of principal strains or principal strain invariants [62]. Moreover, if the material is heterogeneous, an initially axisymmetric membrane may not remain so during inflation (it remains so only if the material property is also axisymmetric). For this reason, the method is limited to only a subclass of heterogeneous materials.

A key mechanical property that the inflation test exploits is the static determinacy of the membrane equilibrium problem. In the inflation test, the meridian and circumferential stresses are determined from the knowledge of the deformed geometry and transmural pressure, according to the Laplace equation. This is in parallel to specimen test where the stress is also computed directly from equilibrium. We should note that the property of static determinacy is not limited to axisymmetric membranes; in fact any pressurized sac-like thin wall structure has this property.

2.3 Mechanics of soft tissues

In the last several decades, the studies in biological tissues have received extensive attention. Due to the ability to deform in a large deformation and the complex structures, the nonlinear elastic behaviors of soft tissues are especially important. To model tissues, an indispensable step is to develop constitutive models, and then to identify their elastic properties, i.e., the elastic parameters in certain models. Attributing to the significance in human lives, the investigations into the heart, arteries, aneurysms, lungs, and corneas have been extremely active. In the following, the mechanics of arteries will be focused upon.

The development of constitutive models for arterial walls has been based on phenomenological or structural approaches. A phenomenological model describes the artery in a macroscopic sense, regardless its microstructure. Whereas, a structural model is proposed by taking into account certain microstructural features of arterial walls. For a complete review of constitutive models for arterial walls, readers are referred to [64]. Phenomenological models include polynomial form [160], logarithmic form [146], and exponential form [39, 21, 28].

The strain-energy function proposed by Delfino describes the arterial walls as an isotropic material, and it has the form

$$W = \frac{a}{b}\left\{\exp\left[\frac{b}{2}\left(I_1 - 3\right)\right] - 1\right\} \tag{2.11}$$

where W is the strain-energy per undeformed volume, I_1 is the trace of the right Cauchy-Green deformation tensor $\mathbf{C}$, and a and b are positive material constants.

The strain-energy functions used most broadly for arterial walls are Fung-type models, which characterize arterial walls as anisotropic materials, and they have the form

$$W = \frac{1}{2}c\left[\exp\left(Q\right) - 1\right] \tag{2.12}$$

where $c \geq 0$ is a material constant, and $Q = Q(E_{AB})$ is a quadratic function of the components of the Green-Lagrange strain tensor $\mathbf{E} = \frac{1}{2}\left(\mathbf{C} - 1\right)$. Here A or B can be either of R, Θ and Z, which stand for the radial, circumferential, and longitudinal directions of the artery, respectively.

The model was proposed originally by Fung et al. [39] for a two-dimensional case where Q has the form

$$Q = b_1 E_{\Theta\Theta}^2 + b_2 E_{ZZ}^2 + 2b_4 E_{\Theta\Theta} E_{ZZ} \tag{2.13}$$

Based on the experiments in [39], Chuong and Fung [21] generalized the two-dimensional model to three-dimensional case, where they assumed that the principal directions of the stress tensor coincide with the radial, circumferential, and longitudinal directions of the artery in the reference configuration, and the shear stresses vanish. In this case, Q is expressed by

$$Q = b_1 E_{\Theta\Theta}^2 + b_2 E_{ZZ}^2 + b_3 E_{RR}^2 + 2b_4 E_{\Theta\Theta} E_{ZZ} + 2b_5 E_{ZZ} E_{RR} + 2b_6 E_{RR} E_{\Theta\Theta}. \tag{2.14}$$

The most general strain-energy function of Fung's type was formulated by Humphrey [64], where three more terms representing the effect of shear stresses were added to the expression of Q, i.e.,

$$\begin{aligned} Q = b_1 E_{\Theta\Theta}^2 + b_2 E_{ZZ}^2 + b_3 E_{RR}^2 + 2b_4 E_{\Theta\Theta} E_{ZZ} + 2b_5 E_{ZZ} E_{RR} + \\ 2b_6 E_{RR} E_{\Theta\Theta} + b_7 E_{\Theta Z}^2 + b_8 E_{RZ}^2 + b_9 E_{R\Theta}^2. \end{aligned} \tag{2.15}$$

Microscopically, arterial wall is composed of three layers, the *intima*, the *media*, and the *adventitia* from the inner surface to the outer surface. The intima consists of a single thin layer of endothelial cells. The media is the middle layer of the artery and consists of a complex three-dimensional network of smooth muscle cells, elastin and collagen fibrils. The orientation of and close interconnection between the elastin and collagen fibrils, elastic laminae, and smooth muscle cells together constitute a continuous fibrous helix [124, 140]. This structural arrangement gives the media high strength, resilience and the ability to resist loads in both longitudinal and circumferential directions. The adventitia is the outermost layer of the artery and consists mainly of fibroblasts and fibrocytes, histological ground substance and thick bundles of collagen fibrils forming a fibrous tissue. The wavy collagen fibrils are arranged in helical structures and serve to reinforce the wall. They contribute significantly to the stability and strength of the arterial wall [60]. As the deformation increases under internal blood pressure, more and more wavy collagen fibers are recruited to bear load, and the stiffness of the adventitia increases accordingly. However, when only passive behavior of the arteries is of interest, the intima is usually neglected due to its thinness, and low stiffness compared to the media and the adventitia.

Aside from phenomenological models, which do not incorporate the histological structures of the arterial walls, e.g., the collagen fiber content and direction, several researchers have developed some structural models while considering the histological information. Holzapfel et al. [60] proposed a strain-energy function to model the multi-layered structure of the arterial walls based the histological information. The model is based on the theory of the mechanics of fiber-reinforced composites [136] and embodies the symmetries of a cylindrically orthotropic material. They modeled the media and the adventitia as composite materials reinforced by two families of collagen fibers which are arranged in symmetrical spirals, and suggested an additive decomposition of the isochoric strain-energy function W into a part W_{iso} associated with the isotropic behavior of the non-collagenous matrix material and another one W_{aniso} associated with the anisotropic behavior of the collagen fiber network, that is

$$W\left(\mathbf{C}, \mathbf{a}_{01}, \mathbf{a}_{02}\right) = W_{iso}\left(\mathbf{C}\right) + W_{aniso}\left(\mathbf{C}, \mathbf{a}_{01}, \mathbf{a}_{02}\right), \tag{2.16}$$

where $\mathbf{C}$ is the right Cauchy-Green deformation tensor , $\mathbf{a}_{01}$ and $\mathbf{a}_{02}$ characterize the directions of the two families of collagen fibers.

Specifically, they propose the forms of W_{iso} and W_{aniso} as

$$\begin{aligned} W_{iso}\left(I_1\right) &= \frac{c}{2}\left(I_1 - 3\right), \\ W_{aniso}\left(I_4, I_6\right) &= \frac{k_1}{2k_2}\sum_{i=4,6}\left\{\exp\left[k_2\left(I_i - 1\right)^2\right] - 1\right\}. \end{aligned} \tag{2.17}$$

Here $c \geq 0$ and $k_1 \geq 0$ are stress-like material constants, $k_2 \geq 0$ is a dimensionless constant, I_i $(i = 1, 4, 6)$ are the strain invariants defined by

$$I_1\left(\mathbf{C}\right) = tr\mathbf{C}, \quad I_4\left(\mathbf{C}, \mathbf{a}_{01}\right) = \mathbf{C} : \mathbf{A}_1, \quad I_6\left(\mathbf{C}, \mathbf{a}_{02}\right) = \mathbf{C} : \mathbf{A}_2 \tag{2.18}$$

where $\mathbf{A}_i$, $(i = 1, 2)$, are defined as the tensor products $\mathbf{a}_{0i} \otimes \mathbf{a}_{0i}$.

The ensuing development of structural models for arterial walls has been contributed by Zulliger et al. [181, 182], Driessen et al. [31].

CHAPTER 3
THEORETICAL FRAMEWORK

3.1 Elements of membrane theory

3.1.1 Kinematics

A membrane is a thin material body of which the thickness is much smaller than the other dimensions. Due to thinness, a membrane has negligible resistance to bending and transverse shear. Thus, it is modeled as a deformable surface that sustains loads by virtue of surface tension. There are numerous ways to present the membrane equations, but we found the tensorially covariant forms based on convected coordinates to be the most convenient for our exposition. In this representation, the surface is parameterized by surface coordinates ξ^α $(\alpha = 1, 2)$ in which a pair of coordinates $P = (\xi^1, \xi^2)$ is regarded as the same material point during the deformation (Figure 3.1). We denoted by $\mathbf{x} = \mathbf{x}(P)$ the position vector of the material point P in a deformed configuration $\mathscr{C} \in \mathbb{R}^3$. The tangent vectors of the coordinate curves

$$\mathbf{g}_\alpha = \frac{\partial \mathbf{x}}{\partial \xi^\alpha} \tag{3.1}$$

form the basis of the surface tangent space at $\mathbf{x}(P)$. An infinitesimal line element is given by $d\mathbf{x} = \mathbf{g}_\alpha d\xi^\alpha$, and its length is determined from the first fundamental form

$$ds^2 = d\mathbf{x} \cdot d\mathbf{x} = g_{\alpha\beta} d\xi^\alpha d\xi^\beta, \quad g_{\alpha\beta} = \mathbf{g}_\alpha \cdot \mathbf{g}_\beta. \tag{3.2}$$

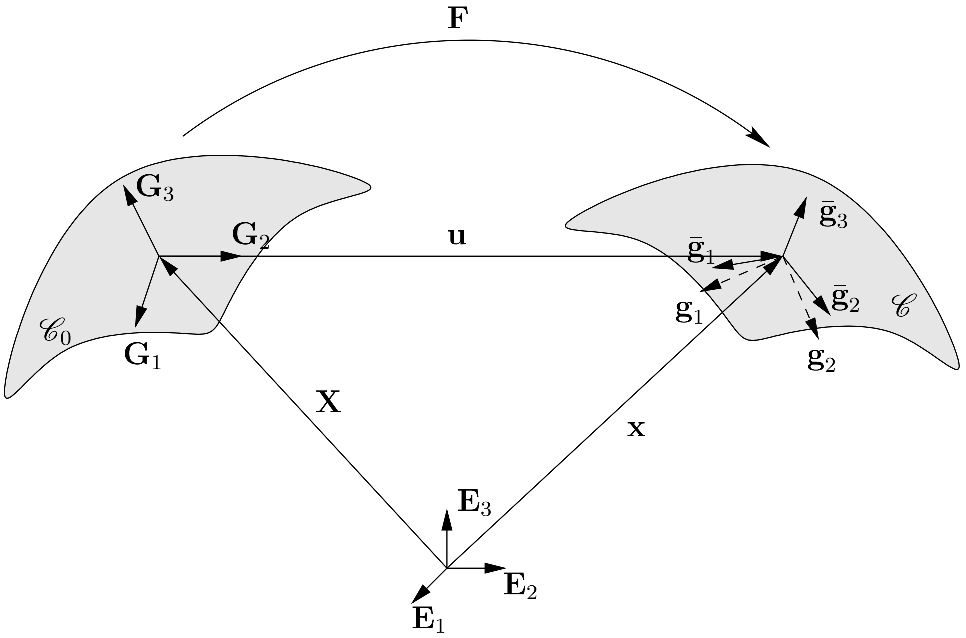

Figure 3.1: Schematic illustration of the kinematic map and base vectors.

The summation convention applies to repeated indices. The coefficients $g_{\alpha\beta}$ constitute the components of the surface metric tensors. The contravariant surface base vectors $\{\mathbf{g}^{\alpha}, \alpha = 1, 2\}$ are defined by the relation $\mathbf{g}^{\alpha} \cdot \mathbf{g}_{\beta} = \delta^{\alpha}_{\beta}$, $\mathbf{g}^{\alpha} \cdot \mathbf{n} = 0$ where $\mathbf{n}$ is the outward unit normal vector of the surface. The dot product $\mathbf{g}^{\alpha} \cdot \mathbf{g}^{\beta}$ gives the components $g^{\alpha\beta}$ of a tensor which is inverse to the metric tensor, i.e. $g^{\alpha\beta} g_{\beta\gamma} = \delta^{\alpha}_{\gamma}$. The kinematic variables depend on the configuration in which they are characterized. The position vector, surface basis, contravariant basis, the components of the metric tensor, and the inverse metric tensor on the stress-free reference configuration $\mathscr{C}_0 \in \mathbb{R}^3$ (if such a configuration can be identified) are denoted by $\mathbf{X}(P)$, $\mathbf{G}_{\alpha}$, $\mathbf{G}^{\alpha}$, $G_{\alpha\beta}$, and $G^{\alpha\beta}$, respectively.

The surface deformation gradient, which maps the surface tangent vectors at

$\mathbf{X}(P)$ in $\mathscr{C}_0$ to the tangent vectors at $\mathbf{x}(P)$ in $\mathscr{C}$, is

$$\mathbf{F} = \mathbf{g}_\alpha \otimes \mathbf{G}^\alpha. \tag{3.3}$$

The tensor $\mathbf{F}$, regarded as a linear operator in 3D space, is singular. However, it can be understood as a nonsingular linear operator on vectors lying in the tangent plane at $\mathbf{X}(P)$. In this sense, the inverse deformation gradient $\mathbf{F}^{-1}$ is

$$\mathbf{F}^{-1} = \mathbf{G}_\alpha \otimes \mathbf{g}^\alpha. \tag{3.4}$$

The Cauchy-Green deformation tensor associated with $\mathbf{F}$ is the surface tensor at $\mathbf{X}(P)$ given by

$$\mathbf{C} = \mathbf{F}^T\mathbf{F} = g_{\alpha\beta}\mathbf{G}^\alpha \otimes \mathbf{G}^\beta. \tag{3.5}$$

The Lagrangian strain tensor is then defined as

$$\mathbf{E} = \frac{1}{2}\left(\mathbf{C} - \mathbf{I}\right) \tag{3.6}$$

where $\mathbf{I}$ is the unit second-order tensor.

3.1.2 Constitutive theory

The constitutive equation of a hyperelastic membrane is described by a strain energy function (energy density per unit undeformed reference area). The specific form of the energy function can be established in several ways. If the 3D strain energy function of the material is known, the surface energy can be deduced by reduction. Alternatively, one can directly postulate a strain energy that depends on the surface deformation gradient [49, 135], and characterize the function form by experiments or some other means. In this work, the second approach is followed. Starting from the assumption $w = w(\mathbf{F})$, the invariant requirement under superposed rigid body motion further requires that $\mathbf{F}$ enter the energy function through $\mathbf{C}$.

If the membrane is isotropic, the material isotropy renders

$$w = w(I_1, I_2), \tag{3.7}$$

where $I_1 = \operatorname{tr}\mathbf{C}$ and $I_2 = \det\mathbf{C}$ are the two principal invariants of tensor $\mathbf{C}$. In our work, it proves to be convenient to express the invariants in tensorially invariant forms:

$$I_1 = g_{\alpha\beta}G^{\alpha\beta}, \quad I_2 = \frac{g}{G}, \tag{3.8}$$

where g and G are the determinants of the matrices $[g_{\alpha\beta}]$ and $[G_{\alpha\beta}]$, respectively.

The fundamental kinetic variable in the membrane theory is the stress resultant (i.e., tension)

$$\mathbf{t} = \int_{-\frac{h}{2}}^{\frac{h}{2}} \boldsymbol{\sigma}\, dh = t^{\alpha\beta}\mathbf{g}_\alpha \otimes \mathbf{g}_\beta, \quad t^{\alpha\beta} = t^{\beta\alpha} \approx h\sigma^{\alpha\beta}, \tag{3.9}$$

where $\sigma^{\alpha\beta}$ are the components of Cauchy stress tensor, and h is the current thickness of the membrane. Properly invariant stress function can be derived with the aid of the *referential* resultant

$$\mathbf{T} = \mathbf{F}^{-1}(J\mathbf{t})\mathbf{F}^{-T}, \quad J = \sqrt{\frac{g}{G}} \tag{3.10}$$

which corresponds to the 2nd Piola-Kirchhoff stress $\mathbf{S}$ in the 3D theory. Since $\mathbf{F}^{-1}\mathbf{g}_\alpha = \mathbf{G}_\alpha$, as evidenced by (3.4), it is clear that $\mathbf{T} = Jt^{\alpha\beta}\mathbf{G}_\alpha \otimes \mathbf{G}_\beta$. Namely, the components $T^{\alpha\beta}$ differ from $t^{\alpha\beta}$ only by the area factor J. The standard argument involving the balance of mechanical power concludes that

$$\mathbf{T} = 2\frac{\partial w}{\partial \mathbf{C}} = 2\frac{\partial w}{\partial g_{\alpha\beta}}\mathbf{G}_\alpha \otimes \mathbf{G}_\beta. \tag{3.11}$$

It follows that, in components,

$$T^{\alpha\beta} = Jt^{\alpha\beta} = 2\frac{\partial w}{\partial g_{\alpha\beta}}. \tag{3.12}$$

For an isotropic membrane we have

$$J\,t^{\alpha\beta} = 2\frac{\partial w}{\partial I_1}G^{\alpha\beta} + 2I_2\frac{\partial w}{\partial I_2}g^{\alpha\beta}. \tag{3.13}$$

If the membrane is anisotropic, say reinforced by two families of fibers whose directions are respectively $\mathbf{N}_1$ and $\mathbf{N}_2$ in the reference configuration, the strain energy function is

$$w = w(I_1, I_2, I_4, I_6), \tag{3.14}$$

where the first and second strain invariants, I_1 and I_2, are given by Equation (3.8), I_4 and I_6 are the fourth and sixth principal invariants which represent the squared stretches of the material line elements along the fiber directions $\mathbf{N}_1$ and $\mathbf{N}_2$, respectively. To derive the explicit form of I_4 and I_6 in the curvilinear coordinate system, we first define two structure tensors as $\mathbf{A}_1 = \mathbf{N}_1 \otimes \mathbf{N}_1$ and $\mathbf{A}_2 = \mathbf{N}_2 \otimes \mathbf{N}_2$. In the reference configuration, $\mathbf{N}_1$ and $\mathbf{N}_2$ can be writen as $\mathbf{N}_1 = N_1^\alpha \mathbf{G}_\alpha$ and $\mathbf{N}_2 = N_2^\alpha \mathbf{G}_\alpha$, respectively. It follows that the invariants I_4 and I_6 are given by

$$I_4 = \mathbf{C} : \mathbf{A}_1 = \frac{N_1^\alpha g_{\alpha\beta} N_1^\beta}{N_1^\delta G_{\delta\gamma} N_1^\gamma}, \quad I_6 = \mathbf{C} : \mathbf{A}_2 = \frac{N_2^\alpha g_{\alpha\beta} N_2^\beta}{N_2^\delta G_{\delta\gamma} N_2^\gamma}. \tag{3.15}$$

In this covariant setting, the fiber vectors in a current configuration are given by $\mathbf{n}_1 = N_1^\alpha \mathbf{g}_\alpha$ and $\mathbf{n}_2 = N_2^\alpha \mathbf{g}_\alpha$, namely, the components remain the same. Thus, the fiber directions are known if their components in a configuration are specified.

Expanding Equation (3.12) for the strain energy function (3.14) gives the stress resultant components

$$\begin{aligned} \frac{J}{2} t^{\alpha\beta} =& \frac{\partial w}{\partial I_1} G^{\alpha\beta} + \frac{\partial w}{\partial I_2} g^{\alpha\beta} + \\ & \left(N_1^\delta G_{\delta\gamma} N_1^\gamma\right)^{-1} I_4 \frac{\partial w}{\partial I_4} N_1^\alpha N_1^\beta + \left(N_2^\delta G_{\delta\gamma} N_2^\gamma\right)^{-1} I_6 \frac{\partial w}{\partial I_6} N_2^\alpha N_2^\beta \end{aligned} \tag{3.16}$$

where $\alpha, \beta, \delta, \gamma = 1, 2$, and repeating index implies summation. For the sake of simplicity, we will use the term “stress” to represent the membrane stress resultant or tension in the remainder of the thesis unless otherwise stated.

In the convected system, the principal invariants of the stress tensor can be computed by

$$J_1 = tr\,(\mathbf{t}) = t^{\alpha\beta} g_{\alpha\beta}, \quad J_2 = det\,(\mathbf{t}) = det\,(t^{\alpha\gamma}) \det\,(g_{\gamma\beta})\,. \tag{3.17}$$

Note that these expressions are invariant under the change of surface coordinates.

3.1.3 Equilibrium equation

The static equilibrium of a membrane is governed by the balance equation [99, 48]

$$\frac{1}{\sqrt{g}} \left(\sqrt{g} t^{\alpha\beta} \mathbf{g}_\alpha\right)_{,\beta} + \mathbf{b} = 0, \tag{3.18}$$

where $g = det\,(g_{\alpha\beta})$, $\mathbf{b}$ is the external force per unit current area. In the traditionally forward sense, the equilibrium equation gives rise to a nonlinear differential equation for the forward deformation.

3.2 Local stress-free configuration

Thin membranes typically collapse when unloaded. They can have multiple stress-free configurations which may not attain a smooth convex shape. To develop a theoretical framework suitable for elastic property identification, it is imperative to have a constitutive description that permits a stressed configuration to be used as the reference configuration. This can be achieved by using the notion of *local stress-free configuration*, which associates each infinitesimal material element with a stress-free configuration that can be reached independently of the surrounding material. The stress-free state of the material body is a virtual configuration composed

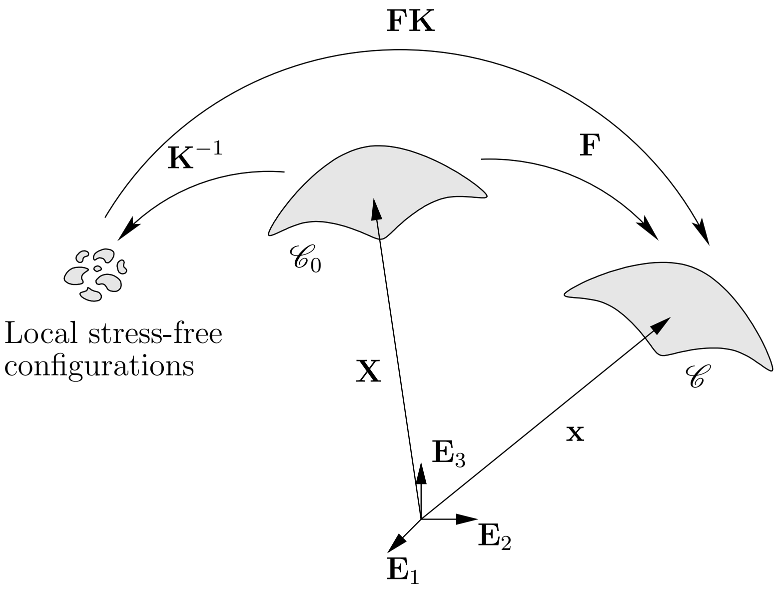

Figure 3.2: Schematic illustration of the kinematic map and the local stress-free configuration.

of the union of the local configurations. The energy function at each material point is characterized with respect to the local stress-free state, whereas the deformation is measured relative to the chosen reference configuration. In this manner, the local stress-free configuration will enter the constitutive law as model parameters. In what follows, we will show that it can be effectively represented by a Riemannian metric tensor endowed to the stress-free configuration. The essential idea of local configuration was initially contained in [156] and further expanded in [100]. This idea has been adapted, in different forms, to describe material inhomogeneity [33, 34], finite plasticity [94, 95, 86, 85], tissue growth [116, 145], residual stress [72, 58], and initial strain [106].

With reference to Figure 3.2, let $\mathbf{K}^{-1}$ be the local deformation that elastically releases the stress in an infinitesimal surface element at point P and brings the material element to a local stress-free configuration. The map $\mathbf{K}^{-1}$ is defined relative to a reference configuration which is not necessarily stress-free. With a slight abuse of notation, this reference configuration is still denoted by $\mathscr{C}_0$, and the associated kinematic variables are denoted by capital letters. The local map $\mathbf{K}^{-1}$, regarded as a linear transformation on the tangent vectors at $\mathbf{X}(P) \in \mathscr{C}_0$, can be determined if its action on two linearly independent tangent vectors are known. If $(\boldsymbol{\mathfrak{G}}_1 d\xi^1, \boldsymbol{\mathfrak{G}}_2 d\xi^2)$ are the images of the line elements $(\mathbf{G}_1 d\xi^1, \mathbf{G}_2 d\xi^2)$, respectively, we can write $\mathbf{K}^{-1}$ as

$$\mathbf{K}^{-1} = \boldsymbol{\mathfrak{G}}_\alpha \otimes \mathbf{G}^\alpha. \tag{3.19}$$

It should be noted that the tensor $\mathbf{K}^{-1}$ is not the gradient of a global mapping. Moreover, since the local configuration is stress-free, any arbitrary re-orientation remains stress-free and thus, the local configuration $\mathbf{K}^{-1}$ is determined to within a left rotation.

Under the local relaxation the line element $d\mathbf{X} = \mathbf{G}_\alpha d\xi^\alpha$ is mapped into $\mathbf{K}^{-1} d\mathbf{X} = \boldsymbol{\mathfrak{G}}_1 d\xi^1 + \boldsymbol{\mathfrak{G}}_2 d\xi^2$. The relaxed length is given by

$$dS_0^2 = (\mathbf{K}^{-1} d\mathbf{X}) \cdot (\mathbf{K}^{-1} d\mathbf{X}) = d\mathbf{X} \cdot (\mathbf{K}^{-T}\mathbf{K}^{-1}) d\mathbf{X}. \tag{3.20}$$

We can interpret the tensor

$$\boldsymbol{\mathfrak{G}} := \mathbf{K}^{-T}\mathbf{K}^{-1} = \mathfrak{G}_{\alpha\beta} \mathbf{G}^\alpha \otimes \mathbf{G}^\beta, \quad \mathfrak{G}_{\alpha\beta} = \boldsymbol{\mathfrak{G}}_\alpha \cdot \boldsymbol{\mathfrak{G}}_\beta \tag{3.21}$$

as a Riemannian metric tensor on $\mathscr{C}_0$ that describes the *unstressed* geometry of material elements. The metric tensor is a local property of the reference configuration; it varies from point to point. The rotation indeterminacy of the local configuration, which presents in $\mathbf{K}^{-1}$, is eliminated in the metric representation.

During a normal deformation $\mathscr{C}_0 \mapsto \mathscr{C}$, the tensor to be used in the constitutive equation is $\mathbf{FK}$ where $\mathbf{F}$ is the regular deformation gradient relative to the reference configuration $\mathscr{C}_0$. For isotropic material, starting from $w = w(\mathbf{FK})$, the invariant requirement renders

$$w = w(\mathbf{K}^T\mathbf{F}^T\mathbf{FK}). \tag{3.22}$$

The rotational indeterminacy implies $w = w(\mathbf{QK}^T\mathbf{F}^T\mathbf{FKQ}^T)$ for any rotation tensor $\mathbf{Q}$. This condition dictates that the energy function depend on the principal invariants I_1 and I_2 of the tensor $(\mathbf{K}^T\mathbf{F}^T\mathbf{FK})$. A straight-forward computation shows

$$\begin{aligned} I_1 &= \mathrm{tr}\,(\mathbf{K}^T\mathbf{F}^T\mathbf{FK}) = g_{\alpha\beta}\mathfrak{G}^{\alpha\beta}, \\ I_2 &= \det(\mathbf{K}^T\mathbf{F}^T\mathbf{FK}) = \frac{g}{\mathfrak{G}}, \quad \mathfrak{G} = \det[\mathfrak{G}_{\alpha\beta}]. \end{aligned} \tag{3.23}$$

Now, we consider the case when the material is anisotropic, say reinforced by two families of fibers. The fiber directions are denoted as $\mathbf{N}_1$ and $\mathbf{N}_2$, respectively, in the reference configuration. The corresponding structure tensors are $\mathbf{A}_1 = \mathbf{N}_1 \otimes \mathbf{N}_1$ and $\mathbf{A}_2 = \mathbf{N}_2 \otimes \mathbf{N}_2$. The fiber directions in the local stress-free configuration are denoted as $\boldsymbol{\mathcal{N}}_1$ and $\boldsymbol{\mathcal{N}}_2$, which, in the current covariant setting, are given as $\boldsymbol{\mathcal{N}}_1 = N_1^\alpha\boldsymbol{\mathfrak{G}}_\alpha$ and $\boldsymbol{\mathcal{N}}_2 = N_2^\alpha\boldsymbol{\mathfrak{G}}_\alpha$, respectively. Again, the components remain the same across different configurations. Denoting the structure tensors in the stress-free configuration as $\boldsymbol{\mathcal{A}}_1 = \boldsymbol{\mathcal{N}}_1 \otimes \boldsymbol{\mathcal{N}}_1$ and $\boldsymbol{\mathcal{A}}_2 = \boldsymbol{\mathcal{N}}_2 \otimes \boldsymbol{\mathcal{N}}_2$, it follows that the components of $\boldsymbol{\mathcal{A}}_i$ are the same as those of $\mathbf{A}_i$, $(i = 1, 2)$.

Then, the strain energy depends on not only the deformation gradient from the local stress-free configuration to the current configuration, but the fiber directions through the structure tensors as $w = w\left(\mathbf{FK}, \boldsymbol{\mathcal{A}}_1, \boldsymbol{\mathcal{A}}_2\right)$. The strain energy function is then dependent on the principal invariants I_4 and I_6 as well. Referred to the local stress-free configuration, I_4 and I_6 are given by

$$\begin{aligned} I_4 &= \left(\mathbf{K}^T\mathbf{F}^T\mathbf{FK}\right) : \boldsymbol{\mathcal{A}}_1 = \frac{N_1^\alpha g_{\alpha\beta} N_1^\beta}{N_1^\delta \mathfrak{G}_{\delta\gamma} N_1^\gamma}, \\ I_6 &= \left(\mathbf{K}^T\mathbf{F}^T\mathbf{FK}\right) : \boldsymbol{\mathcal{A}}_2 = \frac{N_2^\alpha g_{\alpha\beta} N_2^\beta}{N_2^\delta \mathfrak{G}_{\delta\gamma} N_2^\gamma}. \end{aligned} \tag{3.24}$$

It is now clear that the local configuration enters the constitutive equation through the components of the metric tensor $\boldsymbol{\mathfrak{G}}$. This representation is useful for parameter identification. In the case where a global stress-free configuration cannot be attained experimentally, the components $\mathfrak{G}_{\alpha\beta}$ become unknown model parameters which may be identified from experiments. The metric tensor so obtained may not satisfy the geometric compatibility condition even if a globally compatible stress-free configuration exists.

3.3 Finite element inverse elastostatics

In the analysis of finitely deforming elastic bodies, there is a family of problems in which a deformed configuration and the corresponding applied loads are given while the initial configuration or the stress in the deformed state is to be determined [179]. These problems can be tackled from two avenues, one is using duality principles in finite elasticity, the other is using the standard equilibrium equations.

Adkins [1] first established the duality for the particular case of an incompressible, transversely isotropic material in finite plane strain superposed on uniform extension, and he deduced inverse solutions from equilibrium solutions for the same material. Later, Shield [129] showed that for an elastically homogeneous material and zero body force the two sets of equilibrium equations can be written in forms which are identical if initial and final coordinates are interchanged and if the strain energy W_0 per unit volume of the undeformed body is interchanged with the strain energy W per unit volume of the deformed body. This dual property of the elastic equations implied that given an equilibrium deformation with zero body force for one material, the inverse deformation (with initial and final coordinates interchanged in the description of the original deformation) is an equilibrium state for a second material, with strain energy related to the strain energy of the first material [129].

Later, Carlson and Shield [14] showed that the results of [129] can be more easily obtained if one makes use of a variational principle characterizing the equilibrium states, and, moreover, that the results hold for elastic materials of any grade. Succeeding contributions toward this subject were made by Hill [55, 56], Ogden [104, 103], and Chadwick [17].

Yamada [175], and Govindjee and Mihalic [45, 46] proposed the idea of solving the inverse problem using the standard equilibrium equation. This approach hinges on the fact that the stress in an elastic body depends on the deformation gradient, which is a relative measure that involves two configurations. If one configuration is given, the deformation gradient can always be parameterized in terms of the other (unknown) configuration. Consequently, the equilibrium equation, traditionally thought of as a differential equation for the forward deformation, can be expressed in terms of inverse deformation for solving the undeformed configuration in the case of inverse problems. Govindjee named this approach the inverse elastostatics method.

The finite element implementation of inverse elastostatics was introduced by Yamada [175], Govindjee and Mihalic [45] for compressible materials and Govindjee and Mihalic [46] for quasi-incompressible materials. In [45], the authors showed the finite element formulation of the inverse problem entails only minor modifications to the corresponding element for forward problems. Later in [46], they formulated the problem for nearly incompressible materials using a displacement-pressure mixed formulation combined with a penalty method to enforce the quasi-incompressible constraint without locking.

Lu et al. [88] applied finite element inverse elastostatics to compute the stress in a deformed abdominal aortic aneurysm (AAA), which was reconstructed from computed tomography (CT) images, using solid elements and population mean material parameters. In a later paper [87], they extended finite element inverse elastostatics to anisotropic hyperelastic solids. Later, Lu et al. [89, 179] developed inverse formulations for membrane and geometrically exact stress resultant shell models, aiming at particular biomechanical problems of seeking *in vivo* stress in deformed thin-walled biological structures, e.g. cerebral aneurysms. In [89], the authors utilized the inverse membrane element to delineate the stress distribution in a cerebral aneurysm. In light of the static determinacy of stress, they were able to determine the wall tension (stress resultant) without knowing the realistic elastic properties of the cerebral aneurysm and detailed wall thickness information. This work inspired the method in this thesis.

3.4 Inverse elastostatics formulation for membranes

The inverse elastostatics method is a family of methods for solving finite strain elasticity problems in which a deformed configuration and the corresponding loads are given, while the undeformed configuration and the stress in the deformed state are sought. The inverse method employed in this study addresses the following problem: given a deformed configuration of a pressurized membrane and the corresponding pressure, find the stress in the deformed configuration that satisfies the equilibrium equation

$$\frac{1}{\sqrt{g}}\left(\sqrt{g}t^{\alpha\beta}\mathbf{g}_{\alpha}\right)_{,\beta}+p\mathbf{n}=0, \tag{3.25}$$

and appropriate boundary conditions. In the equilibrium equation, $g = det\left(g_{\alpha\beta}\right)$, p is the pressure and $\mathbf{n}$ is the outer unit normal vector of the surface.

The membrane equilibrium problem has a remarkable property, that is, the wall stress depends on the load and the deformed geometry (static determinacy). For a fully convex membrane with known deformed geometry, Equation (3.25) furnishes three partial differential equations that suffice to determine the three components of the stress tensor in a Neumann boundary value problem. In other words, the wall stress in this case is completely independent of material models. For a deep membrane, even if clamped boundary or other displacement boundary conditions present, the influence of material behavior exists only in a thin boundary layer [118, 174].

In the inverse approach, the weak form is formulated directly on the given deformed configuration, hence, the method is expected to sharply capture this static determinacy in pressurized deep membranes. In [89], the stress in the deformed state is determined by means of finding an inverse motion under an assumed elasticity model. The stress free configuration so obtained corresponds to a kinematically compatible configuration which can be brought back to the given deformed configuration upon the application of the given load. It has been demonstrated that, for a clamped deep membrane, the wall stress in regions sufficiently distanced from the clamp boundary is practically independent of the material models chosen to perform the computation. Thus, the "static stress" can be effectively predicted despite the introduction of elasticity models and the ignorance of actual elasticity parameters.

The inverse finite element formulation for membrane problems was presented in [89]. Briefly, the finite element formulation starts with the standard weak form,

$$F := \int_{\Omega} t^{\alpha\beta}\mathbf{g}_{\alpha} \cdot \delta\mathbf{x}_{,\beta} da - \int_{\partial\Omega_t} \bar{\mathbf{t}} \cdot \delta\mathbf{x} ds - \int_{\Omega} p\mathbf{n} \cdot \delta\mathbf{x} da = 0, \tag{3.26}$$

where Ω is the current surface, $\partial\Omega_t$ is the boundary upon which the traction $\bar{\mathbf{t}}$ is applied, and $\delta\mathbf{x}$ is any kinematically admissible variation to the current configuration. In the finite element space the configurations and the variation are approximated by

$$\mathbf{x} = \sum_{I=1}^{Nel} N_I \mathbf{x}^I, \quad \mathbf{X} = \sum_{I=1}^{Nel} N_I \mathbf{X}^I, \quad \delta\mathbf{x} = \sum_{I=1}^{Nel} N_I \delta\mathbf{x}^I. \tag{3.27}$$

Here, the superscript I indicates the nodal number, Nel is the total number of nodes in the element, and N_I is the shape function for the I^{th} node.

Introducing the matrix forms of stress and strain variables, we may write the finite element equation as

$$\int_{\Omega} \mathbf{B}^T \mathbf{t} da - \mathbf{f}^{ext} = 0. \tag{3.28}$$

Here $\mathbf{B} = [\mathbf{B}_1, \mathbf{B}_2, ..., \mathbf{B}_{Nel}]$ is the assembled strain-displacement matrix in which

$$\mathbf{B}_I = \begin{bmatrix} N_{I,1}\mathbf{g}_1^T \\ N_{I,2}\mathbf{g}_2^T \\ N_{I,1}\mathbf{g}_2^T + N_{I,2}\mathbf{g}_1^T \end{bmatrix}_{3\times 3}, \tag{3.29}$$

and $\mathbf{f}^{ext}$ is the external nodal force vector. For a membrane undergoing only normal pressure, $\mathbf{f}^{ext}$ takes the form

$$\mathbf{f}^{ext} = \int_{\Omega} \mathbf{N}^T p \mathbf{n} da \tag{3.30}$$

where $\mathbf{N} = [N_1\mathbf{I}, N_2\mathbf{I}, ..., N_{Nel}\mathbf{I}]$, $\mathbf{I}$ being the identity matrix.

In the inverse setting, the constitutive equation (3.11) is regarded as a function of the referential metric tensor $G_{\alpha\beta}$, which in turn depends on the reference configuration via the relation $G_{\alpha\beta} = \frac{\partial \mathbf{X}}{\partial \xi^\alpha} \cdot \frac{\partial \mathbf{X}}{\partial \xi^\beta}$. The FEM system therefore gives rise to a set of nonlinear algebraic equations for the nodal values of $\mathbf{X}$. In our implementation, these nonlinear equations are solved iteratively using the Newton-Raphson procedure.

Several remarks on the inverse membrane method are in order:

1. In the context of parameter identification, the inverse method replaces the Laplace equation as the stress solver to provide a "static" stress solution independently of the material model to be characterized. The ability to compute the static stress in general convex structures, albeit approximately, is the cornerstone of the methodology. It substantially expands the scope of early inflation tests.

2. The inverse method, however, has several limitations. The method does not apply to membranes that have flat or concave regions. If a membrane has a flat or nearly flat surface area, the ensuing finite element system becomes ill-conditioned or even singular, reflecting the fact that a flat membrane cannot sustain a transverse load. If the surface is concave, equilibrium requirement may render compressive wall stress which should be ruled out by stability consideration. Therefore, the inverse method is not a general method for membrane problems. Rather, it should be applied with close discretion of the user.

3. The inverse solution may not converge if the material model is not chosen properly. For example, if the material is too compliant, the ensuing reference configuration may revert the original surface curvature thus causing numerical diffi-

culty. Nevertheless, our experience indicated that stiffer material models often lead to converged solution. Once the solution converges, the stress depends minimally on the material parameters.

3.5 Transforming stress tensor to convected bases

If stress tensor components are to be used to construct the objective function in the constitutive regression, they need to be represented under convected basis. Similarly, the metric tensors also need to be described under convected basis. This can be done using the same transformation rule, or alternatively one can directly compute the metric tensors from the convected base vectors. In the following, the construction of convected base vectors and the transformation of stress tensor and metric tensors are discussed.

Let's define the coordinate systems involved in the analysis. First, the covariant and contravariant bases vectors of the reference configurations are denoted as $\mathbf{G}_\alpha$ and $\mathbf{G}^\alpha$, respectively. For the sake of simplicity, $\mathbf{G}_1$ and $\mathbf{G}_2$ are set to be orthonormal at every Gauss point. Hence the covariant metric tensor is an identity tensor, i.e.

$$G_{\alpha\beta} = \mathbf{G}_\alpha \cdot \mathbf{G}_\beta = \delta_{\alpha\beta} \tag{3.31}$$

where $\delta_{\alpha\beta}$ is the Kronecker delta. It follows from $G_{\alpha\beta}G^{\beta\gamma} = \delta_\alpha^\gamma$ that the contravariant metric tensor $G^{\alpha\beta} = \delta^{\alpha\beta}$.

Second, in the inverse computation the stress $\mathbf{t}$ is computed at each Gauss point in a local orthonormal coordinate system $\bar{\mathbf{g}}_\alpha$, which leads to

$$\bar{g}_{\alpha\beta} = \bar{\mathbf{g}}_\alpha \cdot \bar{\mathbf{g}}_\beta = \delta_{\alpha\beta}, \quad \bar{g}^{\alpha\beta} = \delta^{\alpha\beta} \tag{3.32}$$

where $\bar{g}_{\alpha\beta}$ and $\bar{g}^{\alpha\beta}$ are respectively the covariant and contravariant metric tensors under basis $\bar{\mathbf{g}}_\alpha$.

It follows that the stress tensor components are the physical components which we denote as t_{11}, t_{22}, $t_{12} = t_{21}$. The principal stresses can be directly computed by

$$\begin{aligned} t_1 &= \frac{t_{11}+t_{22}}{2} + \frac{\sqrt{\left(t_{11}-t_{22}\right)^2 + 4t_{12}^2}}{2}, \\ t_2 &= \frac{t_{11}+t_{22}}{2} - \frac{\sqrt{\left(t_{11}-t_{22}\right)^2 + 4t_{12}^2}}{2}. \end{aligned} \tag{3.33}$$

Either principal stresses t_1 and t_2 or stress invariants J_1 and J_2 in Equation (3.17) could be used to construct the objective functions for the regression algorithms used in the constitutive regression process.

Third, the covariant convected base vectors $\mathbf{g}_\alpha$ emanating from the local orthonormal basis $\mathbf{G}_\alpha$ are computed from

$$\mathbf{g}_\alpha = \mathbf{F}\mathbf{G}_\alpha \tag{3.34}$$

where $\mathbf{F}$ is the deformation gradient from the reference configuration to the deformed configuration. In finite element computation, the deformation gradient is computed with the aid of the isoparametric mapping, as will be described in §4.1.1. The con-

Table 3.1: Base vectors and metric tensors in different coordinate systems.

	Referential	Non-convected	Convected
Configuration	Reference	Current	Current
Base vectors	$\mathbf{G}_\alpha$, $\mathbf{G}^\alpha$	$\bar{\mathbf{g}}_\alpha$, $\bar{\mathbf{g}}^\alpha$	$\mathbf{g}_\alpha$, $\mathbf{g}^\alpha$
Metric tensors	$G_{\alpha\beta} = \delta_{\alpha\beta}$, $G^{\alpha\beta} = \delta^{\alpha\beta}$	$\bar{\mathbf{g}}_{\alpha\beta} = \delta_{\alpha\beta}$, $\bar{\mathbf{g}}^{\alpha\beta} = \delta^{\alpha\beta}$	$g_{\alpha\beta}$, $g^{\alpha\beta}$

travariant convected base vectors $\mathbf{g}^\alpha$ is related to the referential contravariant base vectors $\mathbf{G}^\alpha$ by

$$\mathbf{g}^\alpha = \mathbf{F}^{-T}\mathbf{G}^\alpha. \tag{3.35}$$

The aforementioned various types of base vectors are summarized in Table 3.1 for clarity. For illustration, refer to Figure 3.1.

The underlying motivation of constructing convected basis for each deformed configuration is to represent the covariant and contravariant metric tensors and stress tensor under convected basis, which are required in constitutive regression if stress components are used to construct the objective function.

Write the stress tensor $\mathbf{t}$ in terms of the non-convected base vectors $\bar{\mathbf{g}}_\alpha$ and the convected ones $\mathbf{g}_\alpha$ by

$$t^{\alpha\beta}\mathbf{g}_\alpha \otimes \mathbf{g}_\beta = \bar{t}^{\alpha\beta}\bar{\mathbf{g}}_\alpha \otimes \bar{\mathbf{g}}_\beta. \tag{3.36}$$

Taking the dot product of both side of Equation (3.36) with $\mathbf{g}^\alpha \otimes \mathbf{g}^\beta$, and letting

$Q^{\beta}_{\alpha} = \mathbf{g}^{\beta} \cdot \bar{\mathbf{g}}_{\alpha}$, we obtain

$$t^{\alpha\beta} = Q^{\alpha}_{\delta} \bar{t}^{\delta\gamma} Q^{\beta}_{\gamma}. \tag{3.37}$$

The transformation of the contravariant metric tensors follows the the rule as the stress tensor shown in Equation (3.37), i.e.

$$g^{\alpha\beta} = Q^{\alpha}_{\delta} \bar{g}^{\delta\gamma} Q^{\beta}_{\gamma}, \tag{3.38}$$

where $g^{\alpha\beta}$ are the contravariant metric tensor components under convected basis, and $\bar{g}^{\alpha\beta}$ are the contravariant metric tensor components under non-convected basis. It follows from Equation (3.38) and $g_{\alpha\beta} g^{\beta\gamma} = \delta^{\gamma}_{\alpha}$ that the transformation rule for the covariant metric tensors is

$$g_{\alpha\beta} = \left(Q^{\delta}_{\alpha}\right)^{-1} \bar{g}_{\delta\gamma} \left(Q^{\gamma}_{\beta}\right)^{-1}. \tag{3.39}$$

CHAPTER 4
POINTWISE IDENTIFICATION METHOD

As presented in §3.4, the pointwise stress distribution in a deformed membrane can be determined solely from the deformed shape of the membrane and the internal pressure using the finite element inverse elastostatics methods (FEIEM). Imagine that a finite inflation experiment for a membrane structure can provide multiple deformed configurations, among which the deformation or strain can be recorded as well, one is able to obtain pointwise stress-strain data pairs by applying FEIEM to each deformed configuration. Obviously, the stress-strain data at multiple points in the membrane allows one to examine the elastic behavior of the material, and select an appropriate constitutive model based on such observation, just like specimen testing does. Naturally, one is able to identify the elastic parameters of the selected model by fitting it to the stress-strain data. In this chapter, the general methodology of the proposed pointwise identification methods (PWIM) is described, and it will be validated through numerical experiments and membrane inflation test in the following chapters.

4.1 Method

In PWIM, a membrane structure in its entirety will be mounted to a test stand and inflated to several pressure levels. A mesh will be drawn on the surface or a subregion of interest. The positions of the nodes in each deformed configuration will be recorded by a motion acquisition system to establish a deforming mesh that corresponds through all the deformed states. Stress and strain distributions in each configuration will be computed independently. The analysis consists of the following steps which are also summarized in Figure 7.1:

1. Computing the stress in each configuration individually using FEIEM. The stress components and the orthonormal base vectors are recorded for each deformed configuration. These base vectors are not convected basis and will be made convected after the relative deformation gradients among them are determined.

2. Performing sensitivity analysis to identify the region where the stress is insensitive to material models. This region should be distanced enough (at least several layers of elements) from the essential boundary conditions.

3. Computing the kinematic variables $g_{\alpha\beta}$, $g^{\alpha\beta}$, $\mathbf{g}_\alpha$ and $\mathbf{g}^\alpha$ in each configuration. If the global stress free configuration is known, compute $G_{\alpha\beta}$ and $G^{\alpha\beta}$ from the reference geometry, and then compute the strain invariants I_1 and I_2. If the fiber directions are known, the invariants I_4 and I_6 for anisotropic material are computed accordingly. These strain invariants will be input into the stress function to compute the modeled stress.

4. Describing the stress tensors from Step 1 under the convected bases obtained in Step 3 by applying the linear transformation presented in §3.5.

5. Examining the stress-strain property and selecting appropriate constitutive models.

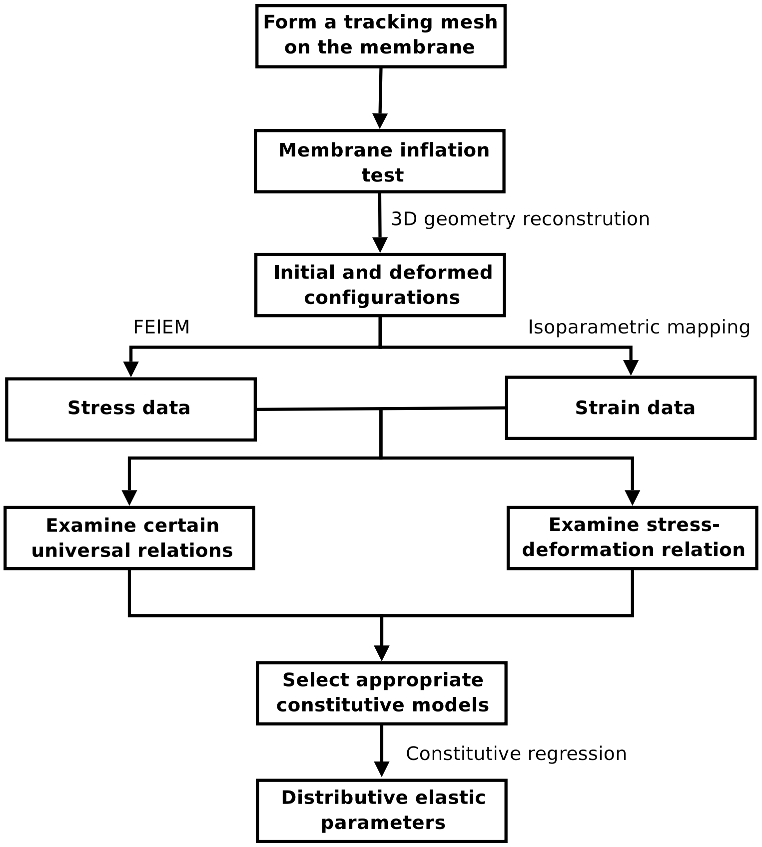

Figure 4.1: Flowchart of PWIM.

6. Obtaining the best-fit model parameters at each Gauss point by fitting nonlinearly the pointwise stress-strain data with the model.
7. Obtaining the distribution of the identified model parameters over the interested domain, and examining the material heterogeneity.

The three core steps of PWIM, i.e., strain acquisition, stress acquisition, and elastic parameter identification, are illustrated in Algorithms 4.1, 4.2 and 4.3. More details will be provided in the ensuing sections.

```
Data: The undeformed and $N$ deformed configurations (FE meshes) of the membrane
Result: Convected base vectors in the undeformed and deformed configurations
begin
    for $i = 1 \leq N$ do
        Conduct finite element interpolation to $\mathscr{C}_i$
        Output $\mathbf{G}_\alpha$, ${}^{(i)}\mathbf{g}_\alpha$ at every Gauss point
    end
end
```

Algorithm 4.1: Strain acquisition for the deformed configurations.

4.1.1 Strain acquisition

Based on the measured nodal positions in the reference and deformed configurations, the position vectors of a point inside the meshed region can be approximated via the finite element interpolation

$$\mathbf{X} = \sum_{I=1}^{Nel} N_I(\xi^1, \xi^2)\mathbf{X}^I, \quad \mathbf{x} = \sum_{I=1}^{Nel} N_I(\xi^1, \xi^2)\mathbf{x}^I. \tag{4.1}$$

Here, the superscript I indicates the nodal number, Nel is the total number of nodes in the element, and N_I is the shape function for the I^{th} node. The natural coordinates (ξ^1, ξ^2) serve as the (element-wise) convected surface coordinates. The displacement field is $\mathbf{u} = \mathbf{x} - \mathbf{X}$. It follows that the covariant base vectors of the reference and current configuration are computed respectively as

$$\mathbf{G}_\alpha = \frac{\partial \mathbf{X}}{\partial \xi^\alpha} = \sum_{I=1}^{Nel} \frac{\partial N_I}{\partial \xi^\alpha} \mathbf{X}^I, \quad \mathbf{g}_\alpha = \frac{\partial \mathbf{x}}{\partial \xi^\alpha} = \sum_{I=1}^{Nel} \frac{\partial N_I}{\partial \xi^\alpha} \mathbf{x}^I. \tag{4.2}$$

```
Data: $N$ deformed configurations (FE meshes) of the membrane
Result: Stress components and non-convected basis in the deformed configurations
begin
    for $i = 1 \leq N$ do
        Apply FEIEM to $\mathscr{C}_i$
        Output ${}^{(i)}\bar{t}^{\alpha\beta}$, ${}^{(i)}\bar{\mathbf{g}}_\alpha$ at every Gauss point
    end
end
```

Algorithm 4.2: Stress acquisition for the deformed configurations.

The components of the covariant metric tensors on the reference and current surface, respectively, are given by

$$G_{\alpha\beta} = \mathbf{G}_\alpha \cdot \mathbf{G}_\beta, \quad g_{\alpha\beta} = \mathbf{g}_\alpha \cdot \mathbf{g}_\beta. \tag{4.3}$$

Other geometric entities such as the contravariant base vectors ($\mathbf{g}^\alpha$, $\mathbf{G}^\alpha$) and the contravariant metric tensor components ($g^{\alpha\beta}$, $G^{\alpha\beta}$) are computed in the standard manner (cf. §3.1.1). Subsequently, the deformation gradient $\mathbf{F}$ and the right Cauchy-Green deformation tensor $\mathbf{C}$ are computed at every Gauss point according to Equations (3.3) and (3.5), respectively. In our implementation, a local orthonormal basis was constructed at every Gauss point in the reference configuration, rendering $G_{\alpha\beta} = \delta_{\alpha\beta}$ and $G^{\alpha\beta} = \delta^{\alpha\beta}$. The components of $\mathbf{C}$ with respect to this basis are the physical components.

```
Data: Pointwise stress-strain data in the $N$ deformed configurations
Result: Pointwise distribution of the elastic parameters
begin
    for $i = 1 \leq N_g$ (Number of Gauss points) do
        for $j = 1 \leq N$ do
            Read stress data and non-convected basis: ${}^{(j)}\bar{t}^{\alpha\beta}$, ${}^{(j)}\bar{\mathbf{g}}_\alpha$ for $\mathscr{C}_j$
            Read convected basis: $\mathbf{G}_\alpha$, ${}^{(j)}\mathbf{g}_\alpha$ for $\mathscr{C}_j$
            Transform stress tensor to be under convected basis: ${}^{(j)}t^{\alpha\beta}$
        end
        Call regression algorithm (SNOPT) to identify elastic parameters
    end
    Obtain the distribution of elastic parameters
end
```

Algorithm 4.3: Pointwise elastic property identification.

The principal stretches λ_1 and λ_2 of the membrane are defined as the eigenvalues of the right stretch tensor $\mathbf{U}$, which is related to the right Cauchy-Green deformation tensor $\mathbf{C}$ through $\mathbf{C} = \mathbf{U}^2$. Thus, the square stretches λ_1^2 and λ_2^2 are the eigenvalues of $\mathbf{C}$, which are given, in terms of the physical components of $\mathbf{C}$, by

$$\begin{aligned} \lambda_1^2 &= \frac{g_{11}+g_{22}}{2} + \frac{\sqrt{\left(g_{11}-g_{22}\right)^2 + 4g_{12}^2}}{2}, \\ \lambda_2^2 &= \frac{g_{11}+g_{22}}{2} - \frac{\sqrt{\left(g_{11}-g_{22}\right)^2 + 4g_{12}^2}}{2}. \end{aligned} \tag{4.4}$$

It follows that the 2D membrane strain invariants are then expressed by

$$\begin{aligned} I_1 &= tr\mathbf{C} = g_{11} + g_{22} = \lambda_1^2 + \lambda_2^2, \\ I_2 &= det\mathbf{C} = \frac{1}{2}\left[\left(tr\mathbf{C}\right)^2 - tr\left(\mathbf{C}^2\right)\right] = g_{11}g_{22} - g_{12}^2 = \lambda_1^2\lambda_2^2. \end{aligned} \tag{4.5}$$

Different constitutive models may use different arguments. For example, Rivlin's approach uses strain invariants as the independent variables in the strain-energy function, whereas Ogden's model uses principal stretches as the independent variables. In this work, both types of constitutive models were used.

It should be noted that the constructed base vectors ${}^{(i)}\mathbf{g}_\alpha$ $(i = 1, 2, ..., n)$ in the n deformed configurations are convected bases. In other words, they share the same inverse mapping $\mathbf{G}_\alpha$ in the reference configuration. In the next section, the stress tensors computed from FEIEM in the deformed configurations will be represented under these convected bases. This process is essential in identifying the elastic parameters in the constitutive model. More details will be given in the following section.

4.1.2 Stress acquisition

Take the multiple deformed configurations as input, the stress resultants (tension) can be determined by using FEIEM. As mentioned above, the stress distribution is independent of material property in the region distanced enough from the boundary. This fact allows us to use an arbitrary constitutive model during stress computation. In this work, a neo-Hookean type hyperelastic strain-energy function is employed, which will be presented later.

In the current setting of FEIEM, a local orthonormal basis is chosen which renders the computed Cauchy stress to be the physical stress in a deformed configuration. For the purpose of elastic parameter identification, the strains in different deformed configurations are required to be measured relative to a common reference configuration. This has been done in the last section. We have constructed the referential base vectors $\mathbf{G}_\alpha$ in the reference configuration $\mathscr{C}_0$, and the current base vectors ${}^{(i)}\mathbf{g}_\alpha$ in the ith deformed configuration $\mathscr{C}_i$. These base vectors are convected basis, and they are related through

$$ {}^{(i)}\mathbf{g}_\alpha = {}^{(i)}_{(0)}\mathbf{F}\mathbf{G}_\alpha, \quad {}^{(j)}\mathbf{g}_\alpha = {}^{(j)}_{(0)}\mathbf{F}\mathbf{G}_\alpha \tag{4.6} $$

and

$$ {}^{(j)}\mathbf{g}_\alpha = {}^{(j)}_{(i)}\mathbf{F}\,{}^{(i)}\mathbf{g}_\alpha \tag{4.7} $$

where ${}^{(i)}_{(0)}\mathbf{F}$ and ${}^{(j)}_{(0)}\mathbf{F}$ are the deformation gradient from the reference configuration $\mathscr{C}_0$ to the ith and jth deformed configurations ($\mathscr{C}_i$ and $\mathscr{C}_j$), respectively, and ${}^{(j)}_{(i)}\mathbf{F}$ is the deformation gradient from $\mathscr{C}_i$ to $\mathscr{C}_j$.

The referential and current covariant metric tensor components are computed according to $G_{\alpha\beta} = \mathbf{G}_\alpha \cdot \mathbf{G}_\beta$ and ${}^{(i)}g_{\alpha\beta} = {}^{(i)}\mathbf{g}_\alpha \cdot {}^{(i)}\mathbf{g}_\alpha$, respectively. They are directly input into the functional form of stress derived from the strain energy function to compute the stress induced by the deformation, i.e.,

$$ {}^{(i)}t^{\alpha\beta} = t^{\alpha\beta}\left(G_{\delta\gamma}, {}^{(i)}g_{\alpha\beta}\right). \tag{4.8}$$

It turns out that the computed stress tensors in two different deformed configurations $\mathscr{C}_i$ and $\mathscr{C}_j$ are described under convected base vectors, i.e.,

$$ {}^{(i)}\mathbf{t} = {}^{(i)}t^{\alpha\beta}\,{}^{(i)}\mathbf{g}_\alpha \otimes {}^{(i)}\mathbf{g}_\beta, \quad {}^{(j)}\mathbf{t} = {}^{(j)}t^{\alpha\beta}\,{}^{(j)}\mathbf{g}_\alpha \otimes {}^{(j)}\mathbf{g}_\beta. \tag{4.9}$$

The underlying requirement is that the corresponding referential stress tensors are described under the same basis $\mathbf{G}_\alpha$. To clarify that, we further write down the referential counterparts of ${}^{(i)}\mathbf{t}$ and ${}^{(j)}\mathbf{t}$ as

$$ {}^{(i)}\mathbf{T} = {}^{(i)}T^{\alpha\beta}\mathbf{G}_\alpha \otimes \mathbf{G}_\beta, \quad {}^{(j)}\mathbf{T} = {}^{(j)}T^{\alpha\beta}\mathbf{G}_\alpha \otimes \mathbf{G}_\beta. \tag{4.10}$$

The relations between the referential and current stress tensors are

$$ {}^{(i)}\mathbf{t} = \frac{1}{J}\left[{}^{(i)}_{(0)}\mathbf{F}\right]\left[{}^{(i)}\mathbf{T}\right]\left[{}^{(i)}_{(0)}\mathbf{F}^T\right], \quad {}^{(j)}\mathbf{t} = \frac{1}{J}\left[{}^{(j)}_{(0)}\mathbf{F}\right]\left[{}^{(j)}\mathbf{T}\right]\left[{}^{(j)}_{(0)}\mathbf{F}^T\right], \tag{4.11}$$

which are the push-forward operation.

Since we need to match the computed stress with the experimental stress (components or invariants), the experimental stress tensor must be described under the same convected base vectors. However, when we acquire stress data for each deformed configuration using FEIEM, the selection of the base vectors is arbitrary. In addition, the deformed configurations are coped with independently. Obviously, the base vectors in each deformed configuration do not form a convected basis. Since we already had a set of convected bases from the deforming mesh, all we need to do is to describe the stress tensors under these bases. By following §3.5, the convected components of the stress can be computed through a linear transformation.

4.1.3 Constitutive regression

As soon as the data of stress and strain are obtained, and an appropriate constitutive model is selected based on the stress-strain relation, we can identify the constitutive constants, i.e. the elastic property using regression algorithms. A regression algorithm requires the user provide an objective function which represents the discrepancy between the numerically modeled and experimentally measured material responses, and needs to be minimized during the regression process. In this work, in order to realize the pointwise feature of the method, we utilized pointwise defined stress to construct the objective function. However, there is a great flexibility to construct such an objective function. For example, one can use stress components, stress invariants, and principal stresses to construct the objective function. Since we used different stress measures to construct the objective function in the numerical experiments and actual experiment, we will present in detail the constitutive regression process in respective chapters.

4.2 Discussion

Inspired by the property of stress static-determinacy in pressurized convex membranes, we devised a new method for pointwise delineating the elastic property of membrane structures. The key feature of the method is the utility of finite element inverse elastostatics methods (FEIEM) for the numerical solution of wall stress. For convex membranes, FEIEM enable us to determine the wall tension using an assumed material model without *a priori* knowledge of the actual elastic properties. Thus, the stress and strain data are acquired independently without being coupled by the constitutive law. However, the elastic properties are contained implicitly in the strain data, and they can be extracted by fitting the stress-strain data with appropriate constitutive models.

Unlike the traditional specimen tests which rely on controlled homogeneous deformations, the present method does not require the uniformity of stress and strain in the allowable protocol. Instead, the actual stress and strain generated during an finite inflation motion of a membrane are employed to characterize the distributive properties. To the best knowledge of the authors, this paradigm of parameter identification has not been fully explored in the literature. In this study, we will verify numerically and experimentally that the method can effectively delineate the pointwise distribution of the elastic properties in nonlinear membranes. The true value of the method, of course, lies in the capability of delineating the heterogeneous property distribution. So far, there are no effective experimental methods that can sharply characterize heterogeneous materials.

4.2.1 Features, speculations

It is instructive to compare the method with other methods for characterizing thin materials, such as the specimen tests [80, 81, 121, 144] and the optimization-based identification methods [74, 79, 69, 66], and axisymmetric membrane inflation test [114, 173, 62, 61].

In the specimen tests, material samples are subjected to load protocols designed to create in the specimen central region an approximately uniform stress state which can then be determined from force equilibrium alone. The experiments essentially create controlled motions that replicate tractable boundary value problems which can be solved without invoking material models. from stress-strain data. In this regard, the current method retains the spirits of static stress computation, and yet carries it to a family of more complicated problems.

In contrast to the optimization-based approaches such as the inverse finite element methods [74, 79, 69, 66], the present method decouples the stress solution and the parameter regression. This not only renders a simpler computation structure, but also leads to, at least in theory, the capability of sharply delineating the distributive properties in heterogeneous membranes. As in the specimen test, the independent acquisition of stress and strain gives us the advantage of examining the stress-strain properties prior to parameter regression. This feature is valuable to the determination of proper constitutive models for the material. For example, one can examine the coaxial condition between stress and strain to evaluate whether or not the material should be modeled as isotropic (if the material is isotropic, the response satisfies the universal relation $\mathbf{SC} = \mathbf{CS}$, see e.g. [9]). The availability of stress-strain protocols to support such a test puts the method to an advantageous position over optimization-based methods.

Another noteworthy feature of the method is its non-destructiveness. Due to the elimination of edge force measurement, the membrane does not need to be cut into pieces. The structure in its entirety is tested. This experimental approach provides a framework for designing non-invasive identification methods for thin biological tissues. When augmented with a suitable method for deformation data acquisition, the method may even lead to a non-invasive approach for extracting the *in vivo* elastic properties of thin living organs.

Owing to the application of fixed displacement boundary condition and the utility of unrealistic elasticity parameters in FEIEM, there is inevitably a thin boundary layer where the inverse stress solution is not accurate. The boundary layer should be avoided in parameter regression. The same issue exists for the specimen test identification methods albeit in a different manner. The boundary effect in the biaxial testing of planar tissues was studied experimentally by Waldman et al. [166, 167] and computationally by Sun et al. [144]. They demonstrated that the gripping methods, e.g. suturing and clamping, or even the number of suture attachments have significant influence over the stress field near the sample edges and even the central region of the sample. This may lead to inaccurate characterization of the material properties.

The current method has the advantage of being suture-free. Boundary effect may be alleviated by using a larger mesh area, or by employing finer mesh near the boundary.

4.2.2 Accuracy issues and solutions

The accuracy of the method depends critically on the quality of stress and strain data. The former, in turn, is highly sensitive to the surface curvature and thus may be strongly influenced by the inaccurate characterization of the surface geometry. If a reconstructed surface has spurious local undulations, it may be necessary to smooth the surface prior to stress computation. Since the strain is computed from the nodal positions via interpolation, its quality is also affected by the aforementioned error. However, the influence on strain accuracy is much minor.

The issue of accuracy can be addressed from several avenues. The first possibility is to use accurate surface data acquisition techniques such as laser scan. Commercial laser scanners can reconstruct solid surfaces to within sub-micron accuracy. The scanners often output triangulated surface or CAD models that can be readily meshed. Secondly, within the present setting one may increase the mesh density by drawing more nodes on the surface. A finer mesh will capture the surface curvature better and produce more accurate stress results. As a by-product, it will also help sharpen the boundary layer identification. Alternatively, one may use high-order elements or other intrinsically smooth approximation methods such as the mesh-free methods [11, 83] or the isogeometric method [63]. These methods are more accurate in geometric description, which in turn render more accurate stress solution.

4.2.3 Limitations

While the method presents a significant advance in thin tissue property identification, it has some inevitable limitations. Firstly, grounded on the static-determinacy of membrane stress, the application is limited to membrane structures. Moreover, the membrane structures must have convex shape in deformed states. An investigation toward the extension to thin-walled shell structures of arbitrary surface characteristics is undertaken in Lu's group. We believe that, in certain situations, the method can be used to identify the in-plane elastic properties of thin-shell structures. Secondly, like the axisymmetric membrane inflation test, one does not have a complete control over the deformation of the membrane to get a desired deformation protocols, e.g., varying a principal stretch while maintaining another. Therefore the individual role of the principal stretches cannot be fully explored. In this regard, the protocols belong to a somewhat restricted subspace in the response surface. The identified material parameters may not accurately reproduce other type of response such as uniaxial tension. Nevertheless, for biological organs the elastic properties identified by this method may contain enough information about the material behavior in its actual function, because the identification is conducted using deformations that closely mimic its mechanical motion in the service environment.

4.2.4 Future of *in vivo* identification for biological tissues

Since the acquisition of stress and strain data is based solely on the deformed geometries in different deformed configurations of a membrane structure, the current method allows for nondestructive identification when combined with optic-based or image-based 3-D geometry reconstruction techniques. In addition, as will be presented in Chapter 5 and 7, this method is capable of identifying elastic properties without the knowledge of the stress-free configuration. Therefore, this method holds the promise of application into *in vivo* identification of the elastic properties in thin-walled biological tissues and organs.

However, due to the non-invasive requirements of *in vivo* identification, it is infeasible to use physical markers to track the deformation. Therefore, a non-invasive deformation measuring method using medical images is needed. Rabbit et al. [109], Weiss et al. [169], Veress et al. [165] and Weiss et al. [170] utilized a deformable image registration method termed Hyperelastic Warping to measure the strain in various tissues, e.g. distal femur using X-ray computed tomographic (CT) images [109], intervertebral disc using MR images [169], coronary arteries using intravascular ultrasound (IVUS images) [165], , and left ventricle using MRI images [170]. Sonka et al. [134] reported an automatic nonrigid segmentation method that allows for motion tracking of an aorta from 4D MR images.

Tagged MR images have been employed to directly acquire displacement data of the heart, which can be used to calculate strain [178, 7, 6, 97]. However, current MR tagging techniques are not adequate to measure aortic wall displacements and strain accurately [29]. Pelc et al. [107] and Draney et al. [30] described a method to quantity vessel wall motion and strain using velocity data acquired with cine phase contrast MRI (PC-MRI). Draney et al. [29] further investigated the capability of the method in quantifying vessel train using *in vivo* images. Nevertheless, their studies were concerned with 2-D deformation. These approaches are promising in tracking the motion of thin aneurysm wall, although they are yet mature enough. To the author's best knowledge, there has been no report on tracking the motion of cerebral aneurysm wall using medical images. Upon the availability of advanced image segmentation and registration techniques capable of tracking the wall motion of cerebral aneurysms, *in vivo* identification of elastic properties may be feasible by utilizing PWIM.

CHAPTER 5
NUMERICAL EXPERIMENTS: ISOTROPIC MATERIAL

5.1 Method

In order to validate the pointwise identification method for isotropic material, a numerical experiment was conducted for a cerebral aneurysm model of homogeneous material. Specifically, the procedure of the numerical experiments consists of

1. Constructing a finite element model for a cerebral aneurysm along with assumed elastic properties including material homogeneity and the values of the elastic parameters, and specific loading and boundary conditions;

2. Generating a series of deformed configurations of a cerebral aneurysm by conducting forward FE analysis using different physiological pressure values;

3. Computing the stress distribution in each deformed configuration by applying FEIEM, and using unrealistic elastic property;

4. Computing necessary kinetic variables and strain measures of each deformed configuration with respect to a chosen reference configuration, which is not necessarily stress-free;

5. Identifying the elastic parameters using a regression algorithm, and reconstructing a distribution of the parameter values over the interested region;

6. Comparing the distribution of the identified elastic parameters to that of the originally assumed one.

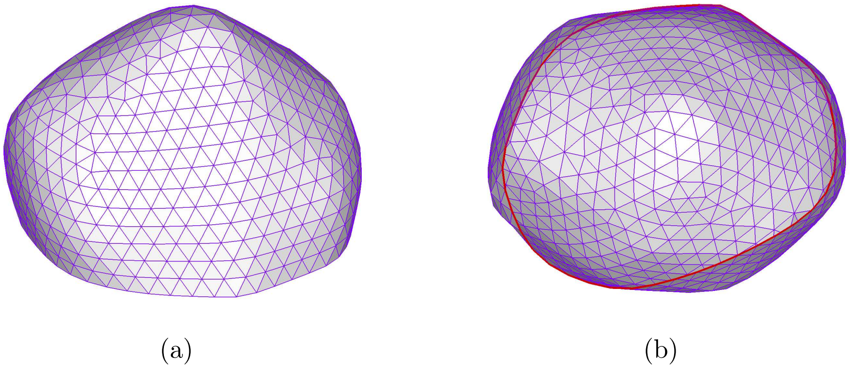
(a) (b)

Figure 5.1: Undeformed geometry and finite element mesh of the membrane sac: (a) Perspective view; (b) Bottom view.

5.1.1 Material model and forward analysis

The membrane structure of the cerebral aneurysm shown in Figure 5.1 was considered. The mesh was originally constructed from the images of a cerebral aneurysm sac which is convex but does not have any particular geometric symmetries. We assume that the wall was described by the strain energy function

$$w_A = \frac{\mu_1}{2}\left(I_1 - 2\log J - 2\right) + \frac{\mu_2}{4}\left(I_1 - 2\right)^2, \tag{5.1}$$

where μ_1 and μ_2 are effective elastic parameters. Without the second term, the energy function corresponds to the classical neo-Hookean material, which is known to suffer a limit-point instability during inflation motions [65]. The second term is introduced as a remedy to stabilize the deformation.

The elastic parameters were set to be

$$\mu_1 = 0.06521739 \text{ N/mm}, \quad \mu_2 = 0.1521739 \text{ N/mm}. \tag{5.2}$$

This model is referred to as *Model A* in the sequel. The parameters μ_1 and μ_2 are the multiplication of the 3D elasticity constants with the wall thickness. Parameters like these are referred to as *effective* elasticity constants. To simulated the clamped boundary constraint typically used in experiments, we assumed that the base of the sac is fixed. Eleven deformed configurations were computed by applying pressures ranging from 60 to 110 mmHg at an interval of 5 mmHg. This was conducted using the (forward) nonlinear membrane finite element in FEAP, a nonlinear finite element program originally developed at the University of California, Berkeley [147]. The maximum surface stretch, which occurs at 110 mmHg pressure, is about 110%.

5.1.2 Stress-strain data acquisition

Subsequently, we took these generated deformed configurations as input, and applied PWIM to identify the elasticity parameters. The stress distribution in each configuration was computed by the inverse finite element method using a material model which has the same energy function as *Model A* but 10 times elevated material constants. We also computed the stress using 100 times elevated parameters to assess the sensitivity of stress to material parameters. The strain distribution was determined by finite element interpolation as described in §4.1.1. If the global stress-free reference configuration was given, the quantities $\mathbf{G}_\alpha$ etc. and subsequently the deformation tensor $\mathbf{C}$ and its invariants I_1 and I_2 were computed accordingly.

5.1.3 Constitutive regression

As seen from equation (3.13), the surface tension components are functions of the components of the reference and the current metric tensors, and the elasticity parameters appearing in the constitutive law. As described above, at every integration point we can obtain the stresses in each of deformed configurations and at least the convected components $g_{\alpha\beta}$ of the current metric tensor. Choosing an appropriate constitutive model, we can express the model stress as functions of the metric tensors and elasticity constants. We denoted the model stress in the i-th configuration by

$$^{(i)}t^{\alpha\beta} = t^{\alpha\beta}(\mu, {}^{(i)}g_{\delta\gamma}, G_{\delta\gamma}), \tag{5.3}$$

where μ stands for the set of elastic parameters. Let $^{(i)}\hat{t}^{\alpha\beta}$ be the "experimental" stress components obtained from the inverse analysis. A logical objective or cost function which represents the difference between the modeled and observed responses is

$$\Phi = \sum_{i=1}^{N} \left({}^{(i)}t^{\alpha\beta} - {}^{(i)}\hat{t}^{\alpha\beta} \right) {}^{(i)}g_{\alpha\gamma} \, {}^{(i)}g_{\beta\delta} \left({}^{(i)}t^{\delta\gamma} - {}^{(i)}\hat{t}^{\delta\gamma} \right), \tag{5.4}$$

where, N is the total number of deformed states. In tensor notation, $\Phi = \sum_{i=1}^{N} \parallel {}^{(i)}\mathbf{t} - {}^{(i)}\hat{\mathbf{t}} \|^2$. If the global stress-free configuration is given, Φ is a function of the material parameters only. Otherwise, Φ depends also on the local metric tensor components $\mathfrak{G}_{\alpha\beta}$, which will be included in the identification. This amounts to adding three additional model parameters to the optimization problem at every regression point.

Since $\boldsymbol{\mathfrak{G}}$ is a metric tensor, it is natural to impose the positiveness requirement. In this case, the regression problem can be described as

$$\begin{aligned} &\text{minimize} && \Phi\left(\mu, \mathfrak{G}_{\alpha\beta}\right) \\ &\text{subject to} && \mathfrak{G}_{11} > 0, \quad \mathfrak{G}_{22} > 0, \quad \mathfrak{G}_{11}\mathfrak{G}_{22} - \mathfrak{G}_{12}^2 > 0, \\ &\text{and} && \mathbf{l} \leq \left(\mu, \mathfrak{G}_{\alpha\beta}\right) \leq \mathbf{u}. \end{aligned} \tag{5.5}$$

Here, $\mathbf{l}$ and $\mathbf{u}$ are the lower and upper bounds of the regression variables μ and $\mathfrak{G}_{\alpha\beta}$. The parameter identification was performed by a gradient-based, sequential quadratic programming (SQP) algorithm, SNOPT [43]. As long as the constitutive model is selected, we can compute the analytical gradients of the objective function Φ with respect to the regression variables.

In order to validate the capability of the method, we fit the obtained stress-strain data to two different constitutive models, one is the same model as was used in the process of generating the deformed configurations (*Model A*), and the other is a distinct model (*Model B*) which exhibits a similar mechanical behavior to that of *Model A*. *Model B* has the energy function

$$w_B = \nu_1 \left\{ \exp\left[\left(I_1 - 2\log J - 2 \right) \right] - 1 \right\} + \frac{\nu_2}{4} \left(I_1 - 2 \right)^2, \tag{5.6}$$

here ν_1 and ν_2 are effective elastic parameters. In the neighborhood of $(I_1, I_2) = (2, 1)$, the two energy functions obviously have similar characteristics. We performed parameter identification under the assumptions of knowing the reference configuration and without knowing the reference configuration. The stress functions of both models and the stress gradients required by the optimization algorithm are presented in the following section.

5.1.4 Stress gradients

When using gradient based optimization algorithms, one often needs to provide the analytical gradients of the objective function with respect to the regression variables. The following two subsections present the analytical gradients of the tension tensor components with respect to the material parameters and the metric tensor components of the stress-free configuration, for *Model A* and *Model B*, respectively.

5.1.4.1 ***Model A***

The convected components of the tension tensor are derived as

$$t^{\alpha\beta} = \frac{1}{J}\left\{\left[\mu_1 + \mu_2\left(I_1 - 2\right)\right] G^{\alpha\beta} - \mu_1 g^{\alpha\beta}\right\}. \tag{5.7}$$

In Equation (5.7), we replace $G^{\alpha\beta}$ with $\mathfrak{G}^{\alpha\beta}$ if the stress-free configuration is unknown, for the sake of consistency with the notation in §3.2.

The stress gradients are defined as the partial derivatives of the tension tensor components $t^{\alpha\beta}$ with respect to the regression variables. The stress gradients with respect to the elasticity parameters, μ_1 and μ_2, are repectively

$$\frac{\partial t^{\alpha\beta}}{\partial \mu_1} = I_2^{-1/2}\left(G^{\alpha\beta} - g^{\alpha\beta}\right), \tag{5.8}$$

$$\frac{\partial t^{\alpha\beta}}{\partial \mu_2} = I_2^{-1/2} \left(I_1 - 2\right) G^{\alpha\beta}. \tag{5.9}$$

If the stress-free configuration is unknown, the stress gradients with respect to the contravariant reference metric tensor components $\mathfrak{G}^{\alpha\beta}$ are

$$\frac{\partial t^{\alpha\beta}}{\partial \mathfrak{G}^{11}} = -\frac{1}{2} I_2^{-3/2} g \mathfrak{G}^{22} \left(\gamma \mathfrak{G}^{\alpha\beta} - \mu_1 g^{\alpha\beta}\right) + I_2^{-1/2} \left(\gamma \frac{\partial \mathfrak{G}^{\alpha\beta}}{\partial \mathfrak{G}^{11}} + \mu_2 g_{11} \mathfrak{G}^{\alpha\beta}\right), \tag{5.10}$$

$$\frac{\partial t^{\alpha\beta}}{\partial \mathfrak{G}^{22}} = -\frac{1}{2} I_2^{-3/2} g \mathfrak{G}^{11} \left(\gamma \mathfrak{G}^{\alpha\beta} - \mu_1 g^{\alpha\beta}\right) + I_2^{-1/2} \left(\gamma \frac{\partial \mathfrak{G}^{\alpha\beta}}{\partial \mathfrak{G}^{22}} + \mu_2 g_{22} \mathfrak{G}^{\alpha\beta}\right), \tag{5.11}$$

$$\frac{\partial t^{\alpha\beta}}{\partial \mathfrak{G}^{12}} = I_2^{-3/2} g \mathfrak{G}^{12} \left(\gamma \mathfrak{G}^{\alpha\beta} - \mu_1 g^{\alpha\beta}\right) + I_2^{-1/2} \left(\gamma \frac{\partial \mathfrak{G}^{\alpha\beta}}{\partial \mathfrak{G}^{12}} + 2\mu_2 g_{12} \mathfrak{G}^{\alpha\beta}\right), \tag{5.12}$$

where, $\gamma = \mu_1 + \mu_2 \left(I_1 - 2\right)$, and $g = det\left(g_{\alpha\beta}\right)$.

5.1.4.2 ***Model B***

The convected tension components of this model are

$$t^{\alpha\beta} = \frac{1}{J} \left[2\nu_1 \exp\left[\left(I_1 - 2\log J - 2\right)\right] \left(G^{\alpha\beta} - g^{\alpha\beta}\right) + \nu_2 \left(I_1 - 2\right) G^{\alpha\beta}\right]. \tag{5.13}$$

Likewise, $G^{\alpha\beta}$ will be replaced by $\mathfrak{G}^{\alpha\beta}$ if the stress-free configuration is unknown. The stress gradients with respect to the elasticity parameters are given by

$$\frac{\partial t^{\alpha\beta}}{\partial \nu_1} = 2 I_2^{-1/2} \xi \left(G^{\alpha\beta} - g^{\alpha\beta}\right), \tag{5.14}$$

$$\frac{\partial t^{\alpha\beta}}{\partial \nu_2} = I_2^{-1/2} \left(I_1 - 2\right) G^{\alpha\beta}. \tag{5.15}$$

The stress gradients with respect to the unknown contravariant metric tensor components of the stress-free configuration are

$$\begin{aligned}\frac{\partial t^{\alpha\beta}}{\partial \mathfrak{G}^{11}} =& -\frac{1}{2} I_2^{-3/2} g \mathfrak{G}^{22} \left[\left(2\nu_1 \xi + \nu_2 \eta\right) \mathfrak{G}^{\alpha\beta} - 2\nu_1 \xi g^{\alpha\beta}\right] \\ &+ I_2^{-1/2} \left[2\nu_1 \xi \left(g_{11} - I_2^{-1} g \mathfrak{G}^{22}\right)\right] \left(\mathfrak{G}^{\alpha\beta} - g^{\alpha\beta}\right) \\ &+ I_2^{-1/2} \left[\nu_2 g_{11} \mathfrak{G}^{\alpha\beta} + \left(2\nu_1 \xi + \nu_2 \eta\right) \frac{\partial \mathfrak{G}^{\alpha\beta}}{\partial \mathfrak{G}^{11}}\right],\end{aligned} \tag{5.16}$$

$$\begin{aligned}\frac{\partial t^{\alpha\beta}}{\partial \mathfrak{G}^{22}} =& -\frac{1}{2} I_2^{-3/2} g \mathfrak{G}^{11} \left[\left(2\nu_1 \xi + \nu_2 \eta\right) \mathfrak{G}^{\alpha\beta} - 2\nu_1 \xi g^{\alpha\beta}\right] \\ &+ I_2^{-1/2} \left[2\nu_1 \xi \left(g_{22} - I_2^{-1} g \mathfrak{G}^{11}\right)\right] \left(\mathfrak{G}^{\alpha\beta} - g^{\alpha\beta}\right) \\ &+ I_2^{-1/2} \left[\nu_2 g_{22} \mathfrak{G}^{\alpha\beta} + \left(2\nu_1 \xi + \nu_2 \eta\right) \frac{\partial \mathfrak{G}^{\alpha\beta}}{\partial \mathfrak{G}^{22}}\right],\end{aligned} \tag{5.17}$$

$$\begin{aligned}\frac{\partial t^{\alpha\beta}}{\partial \mathfrak{G}^{12}} =& I_2^{-3/2} g \mathfrak{G}^{12} \left[\left(2\nu_1 \xi + \nu_2 \eta\right) \mathfrak{G}^{\alpha\beta} - 2\nu_1 \xi g^{\alpha\beta}\right] \\ &+ I_2^{-1/2} \left[4\nu_1 \xi \left(g_{12} + I_2^{-1} g \mathfrak{G}^{12}\right)\right] \left(\mathfrak{G}^{\alpha\beta} - g^{\alpha\beta}\right) \\ &+ I_2^{-1/2} \left[2\nu_2 g_{12} \mathfrak{G}^{\alpha\beta} + \left(2\nu_1 \xi + \nu_2 \eta\right) \frac{\partial \mathfrak{G}^{\alpha\beta}}{\partial \mathfrak{G}^{12}}\right],\end{aligned} \tag{5.18}$$

where $\xi = e^{I_1 - 2\log J - 2}$, $\eta = I_1 - 2$.

5.2 Results

5.2.1 Material insensitivity of membrane stress

The distribution of the principal stress resultants in the deformed configuration under the highest pressure ($p = 110$ mmHg) is shown in Figure 5.2. Figure 5.3 shows the relative difference (in percentage) of principal stress resultants under drastic changes in elasticity parameters of *Model A*. The upper and lower rows show the percentage difference in tension due to the increase of both material parameters μ_1

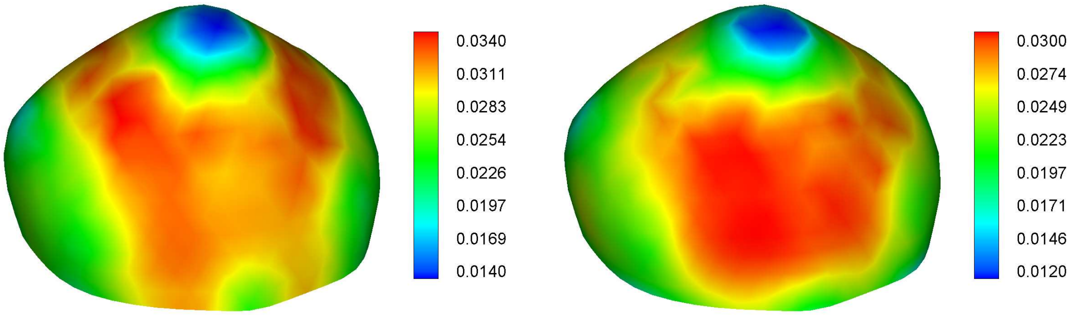

(a) (b)

Figure 5.2: The distribution of principal stress resultants in the membrane sac: (a) t_1; (b) t_2.

and μ_2 by 10 times and 100 times, respectively. Conservatively speaking, the change of the principal stresses is less than 0.15% in the region two layers of elements above the clamped base. In the region near the boundary, the change of principal stresses is relatively large. However, it is below 1%. This analysis allows us to identify the boundary-effect-free regions where parameter identification is to likely yield reliable results. Later, the sac region excluding five layers of elements from the base is designated as the identification zone. The stress values computed from 10 times elevated parameters were used in the parameter regression.

5.2.2 Identified elastic parameters

Figure 5.4 shows the distribution of the identified elasticity parameters (μ_1 and μ_2) of *Model A* under the condition that the global stress free-configuration is known. In this case, the original mesh is taken to be the reference configuration $\mathscr{C}_0$,

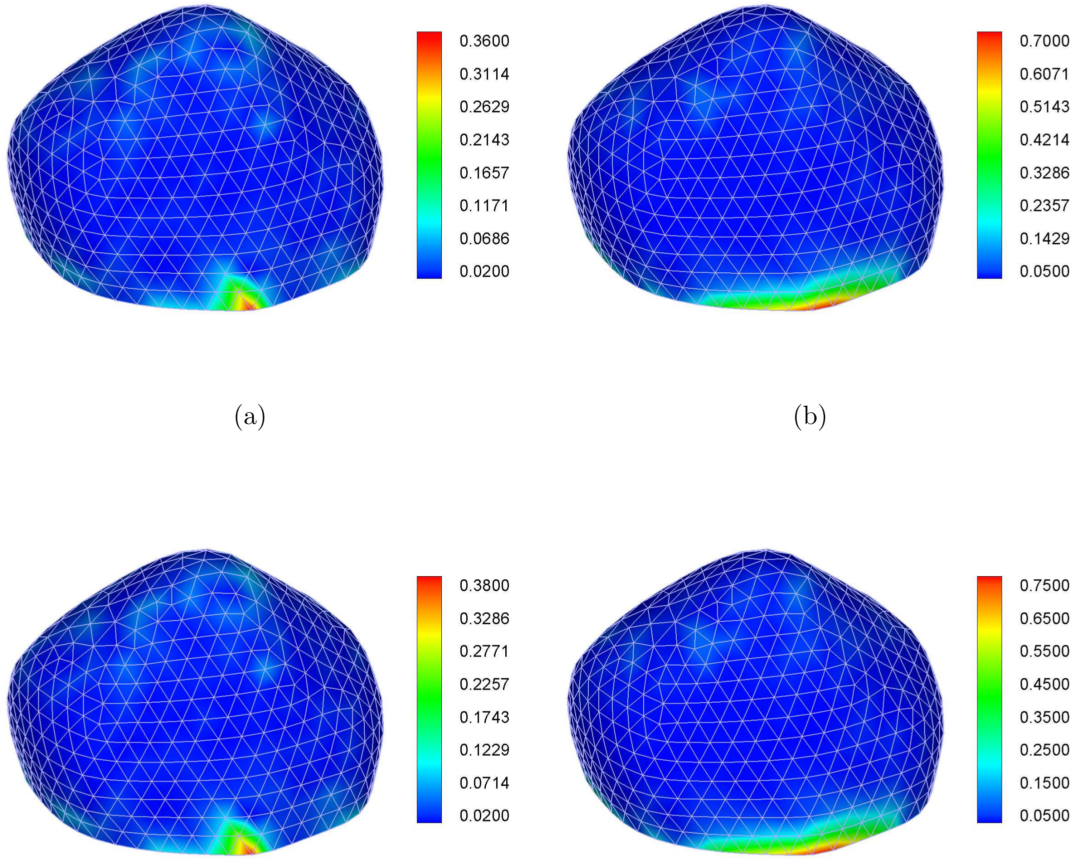

(a) (b)

(c) (d)

Figure 5.3: The percentage difference of principal stress resultants under the change of elasticity parameters. Upper row: Increasing both parameters μ_1 and μ_2 by 10 times: (a) t_1, (b) t_2; Lower row: Increasing both parameters μ_1 and μ_2 by 100 times: (c) t_1, (d) t_2.

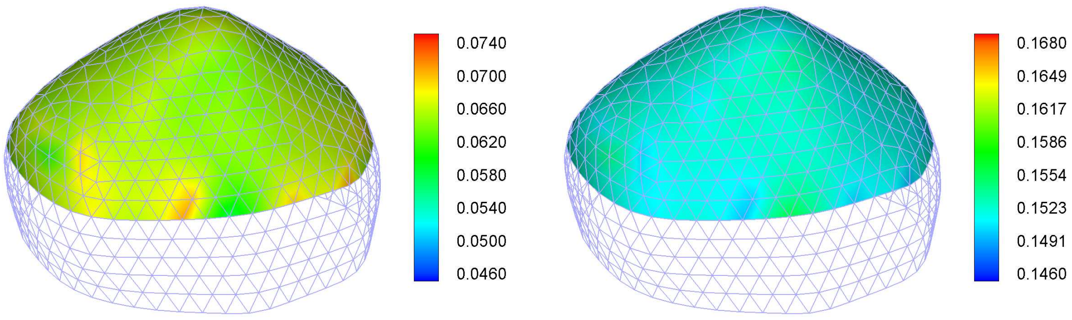

(a) (b)

Figure 5.4: Identified elasticity parameters of *Model A* knowing the reference metric: (a) μ_1, (b) μ_2.

and the referential quantities $G_{\alpha\beta}$ etc. are computed from this given geometry. In the dome region six layers away from the boundary which is shown in Figure 5.4, the identified parameters μ_1 ranges from 0.06119 N/mm to 0.07010 N/mm, and μ_2 shows a narrower range of 0.14986 N/mm to 0.15410 N/mm. Since the stress is computed by FEIEM using a model different from that in the forward computation (10 times of the true elasticity parameters), and hence the acquired stress is not identical to the true stress, the identified parameters are expected to deviate from their true values. The distribution of the identification error (in percentage relative to the true parameters) by knowing the reference metrics are illustrated in Figure 5.5. As the figures show, the identification error falls below 8% and 2% for μ_1 and μ_2, respectively.

Figure 5.6 illustrates the distribution of the identified elasticity parameters of *Model A* without the assumption of known stress-free configuration. Figure 5.7

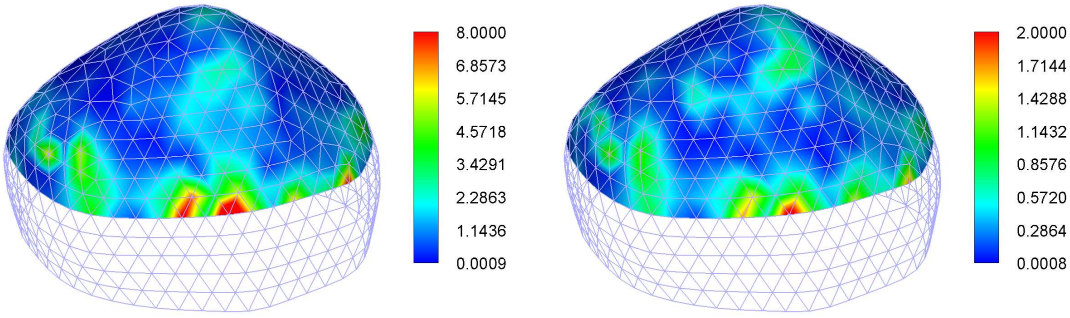

(a) (b)

Figure 5.5: Absolute values of the relative error (in percentage) between identified elasticity parameters and true parameters of *Model A* knowing the reference metric: (a) μ_1, (b) μ_2.

shows the identification error. In the dome region seven layers of elements away from the boundary, the identified parameters μ_1 ranges from 0.05720 N/mm to 0.07872 N/mm, and μ_2 presents a narrower range of 0.14647 N/mm to 0.15563 N/mm. The percentage error of the identified parameters falls below 15% and 3% for μ_1 and μ_2, respectively. It is evident that, in both cases the constant μ_2, which is the leading parameter in this model, is recovered to within a very small error. The identification of constant μ_1 is less accurate, but is still within an acceptable range.

Figure 5.8 shows the distribution of the identified elasticity parameters of *Model B*, with the assumption of the stress-free configuration being given. The distribution of the parameters shows an approximate uniformity in the region six layers of elements away from the boundary. The ranges of the identified parameters are 0.03052 N/mm $\leq \nu_1 \leq$ 0.03492 N/mm, and 0.14981 N/mm $\leq \nu_2 \leq$ 0.15407 N/mm.

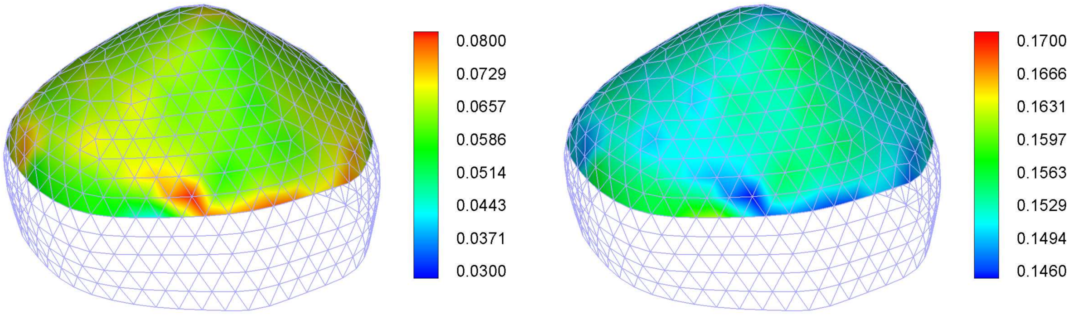

(a) (b)

Figure 5.6: Identified elasticity parameters of *Model A* without knowing the reference metric: (a) μ_1, (b) μ_2.

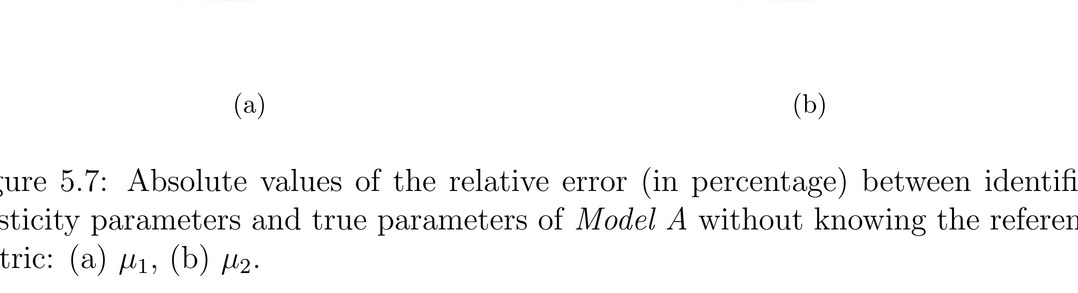

(a) (b)

Figure 5.7: Absolute values of the relative error (in percentage) between identified elasticity parameters and true parameters of *Model A* without knowing the reference metric: (a) μ_1, (b) μ_2.

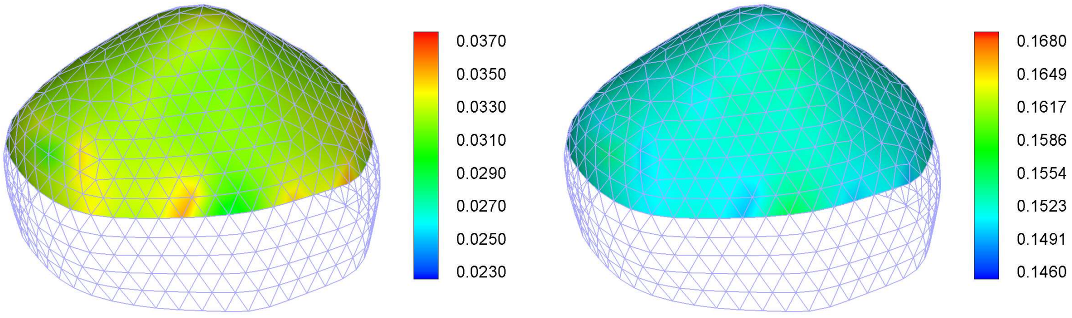

(a) (b)

Figure 5.8: Identified elasticity parameters of *Model B* knowing the reference metric: (a) ν_1, (b) ν_2.

Figure 5.9 shows the distribution of the identified elasticity parameters of *Model B*, without assuming that the stress-free configuration is given. The distribution of the parameters is approximately uniform in the region seven layers of elements above the boundary. The ranges of the identified parameters are 0.02778 N/mm $\leq \nu_1 \leq$ 0.04037 N/mm, and 0.14524 N/mm $\leq \nu_2 \leq$ 0.15555 N/mm. It is expected that the identified parameters span wider ranges for the case of stress-free configuration being unknown due to the increase of the number of the regression variables.

It is also informative to conduct a statistical analysis in the boundary-effect-free region to examine how well the homogeneity has been identified. Table 5.1 and Table 5.2 list the means and standard deviations of the identified elasticity parameters for both models over the aforementioned boundary-effect-free regions for both knowing and without knowing the local stress-free configurations. For both models,

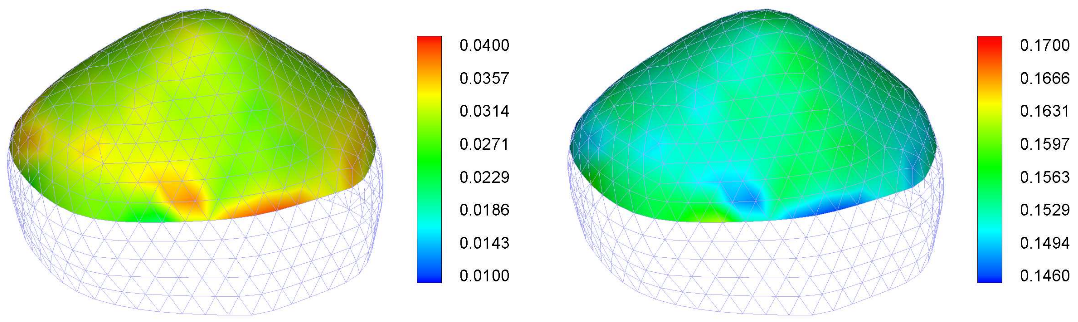

(a) (b)

Figure 5.9: Identified elasticity parameters of *Model B* without knowing the reference metric: (a) ν_1, (b) ν_2.

adding the local reference metric tensor components as three more regression variables generally renders larger standard deviations of identified elasticity parameters. However, the standard deviations of these data, especially those of μ_2, are very small. Hence, we conclude quantitatively that the homogeneity is satisfactorily recovered.

Figure 5.10 illustrates the comparison between the tension invariants modeled by *Model B* and the "experimental" tension invariants at a point where a relatively large principal stretch ($\lambda_1 = 1.076$) occurs. The good match between these two curves suggests that *Model B* fits well the stress-strain data generated by *Model A*. It also provides an *ad hoc* justification for our choice of *Model B*.

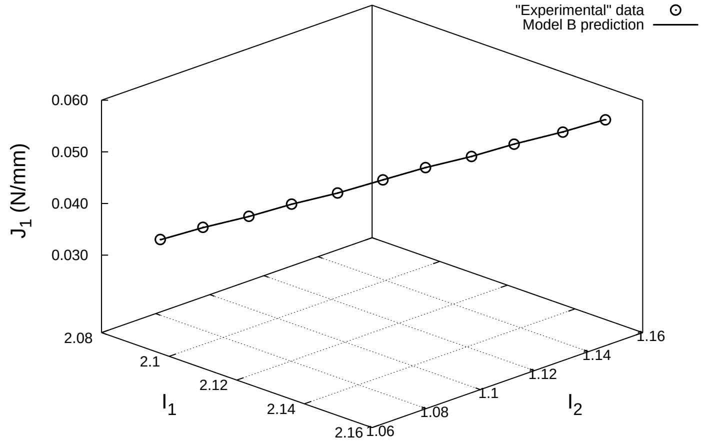

(a)

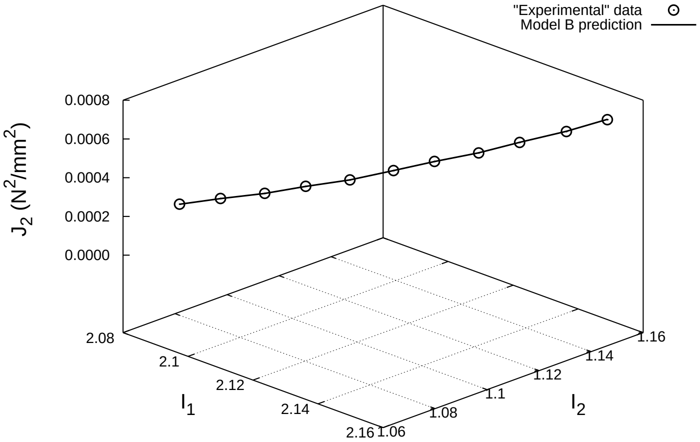

(b)

Figure 5.10: Comparison between the "experimental" tension invariants and the predictions of *Model B*: (a) J_1, (b) J_2.

Table 5.1: The means and standard deviations of identified elasticity parameters of *Model A* and *Model B knowing* the reference metric tensor.

	Model A		*Model B*	
	μ_1	μ_2	ν_1	ν_2
Mean (N/mm)	0.06516	0.15208	0.03239	0.15206
SD (N/mm)	0.00113	0.00061	0.00057	0.00061

Table 5.2: The means and standard deviations of identified elasticity parameters of *Model A* and *Model B without knowing* the reference metric tensor.

	Model A		*Model B*	
	μ_1	μ_2	ν_1	ν_2
Mean (N/mm)	0.06484	0.15218	0.03132	0.15257
SD (N/mm)	0.00328	0.00143	0.00200	0.00168

CHAPTER 6
EXPERIMENTAL VALIDATION: RUBBER BALLOON TEST

6.1 Review of rubber elasticity

Rubber-like materials are characterized by high extensibility and reversibility after deformation. The behavior of rubber materials is usually described to be isotropic hyperelastic. Mathematically, the strain energy function W can be formulated in terms of either the principal invariants of the strain or the principal stretches. The effort of seeking a specific form of W in terms of strain invariants or principal stretches has been based on statistical theory of the long-chain molecule and phenomenological approach. Since we do not intend to give a complete review on the subject of rubber elasticity, we only review some works which are relevant to this study.

The most elementary form of W in the context of Gaussian statistical theory of the cross-linked network is

$$W = \frac{1}{2}G\left(\lambda_1^2 + \lambda_2^2 + \lambda_3^2 - 3\right), \tag{6.1}$$

where λ_1, λ_2 and λ_3 are the principal stretch ratios, and G is a constant given by

$$G = NkT, \tag{6.2}$$

in which N is the number of network chains per unit volume, k is the Boltzmann constant, and T is the absolute temperature. G is equivalent to the shear modulus [154].

Based on Gaussian statistics and molecular network theory, Treloar [149, 150] derived the form of W

$$W = C_1(I_1 - 3), \tag{6.3}$$

where C_1 is a material constant, and I_1 is the first principal invariant of the right Cauchy-green deformation tensor. This form is the famous neo-Hookean form. It is only a first order approximation of rubber behavior, and provides a good correlation with the experimental data in a small deformation range.

Alongside statistical-molecular theories, numerous purely phenomenological models have emerged which describe the mechanical properties of rubber-like materials from a macroscopic point of view, without concerning the structural or molecular interpretation. Mooney [96] is the first investigator who studied phenomenological models for rubber-like materials. By assuming homogeneity, material isotropy before and after extension or compression, isometric deformation (incompressibility), negligible hysteresis and shear being proportional to traction in simple shear, he deduced the well-known Mooney-Rivlin constitutive equation

$$W = C_1\left(I_1 - 3\right) + C_2\left(I_2 - 3\right) \tag{6.4}$$

where C_1 and C_2 are material constants, I_1 and I_2 are the two strain invariants which defined by

$$\begin{aligned} I_1 &= tr\mathbf{C} = \lambda_1^2 + \lambda_2^2 + \lambda_3^2, \\ I_2 &= \frac{1}{2}\left((tr\mathbf{C})^2 - tr\mathbf{C}^2\right) = \lambda_1^2\lambda_2^2 + \lambda_2^2\lambda_3^2 + \lambda_3^2\lambda_1^2. \end{aligned} \tag{6.5}$$

Here, $\mathbf{C}$ is the right Cauchy-Green deformation tensor. If incompressibility condition is enforced, which is reasonable for most rubber-like materials and biological tissues, $I_3 = det\mathbf{C} = \lambda_1^2\lambda_2^2\lambda_3^2 = 1$. Therefore, $\lambda_3^2 = \lambda_1^{-2}\lambda_2^{-2}$, and Equation (6.5) may be expressed as

$$\begin{aligned} I_1 &= \lambda_1^2 + \lambda_2^2 + \lambda_1^{-2}\lambda_2^{-2}, \\ I_2 &= \lambda_1^{-2} + \lambda_2^{-2} + \lambda_1^2\lambda_2^2. \end{aligned} \tag{6.6}$$

Functional form (6.4) can be written as

$$W = \frac{G}{4}\sum_{i=1}^{3}\left(\lambda_i - \frac{1}{\lambda_i}\right)^2 + \frac{H}{4}\sum_{i=1}^{3}\left(\lambda_i^2 - \frac{1}{\lambda_i^2}\right) \tag{6.7}$$

if one make the substitution

$$C_1 = \frac{G+H}{4}, \quad C_2 = \frac{G-H}{4}. \tag{6.8}$$

Here, G is the modulus of rigidity, H is the modulus characterizing asymmetry of reciprocal deformations.

Rivlin [112] showed that the strain-energy function W for an incompressible isotropic elastic material must be expressible as a function of two strain invariants I_1 and I_2 ($I_3 = 1$), which in turn is an even-powered function of the principal stretch ratios, λ_1, λ_2 ($\lambda_3 = (\lambda_1\lambda_2)^{-1}$). A general form can be represented by

$$W = \sum C_{ij} \left(I_1 - 3\right)^i \left(I_2 - 3\right)^j \tag{6.9}$$

where C_{ij} are material constants. In the case of $i = 1$ and $j = 0$, Equation (6.9) reduces to

$$W = C_1 \left(I_1 - 3\right) \tag{6.10}$$

which is equivalent to the strain energy function derived by Treloar [149, 150] based on Gaussian statistics and molecular network theory, i.e. Equation (6.3). When $i = j = 1$, Equation (6.9) reduces to the Mooney form (6.4), also called Mooney-Rivlin strain energy function.

Rivlin also pointed out that the form of W can be derived directly from the experimental data of certain types of simple experiments, e.g. biaxial extension test. However, the accuracy of this derivation is limited by the accuracy with which the experiments are carried out. Rivlin and Saunders [114] conducted controlled strain invariant tests (i.e., varying one invariant while maintaining another) and found out that $\partial W/\partial I_1$ is independent of I_1 and I_2, whereas $\partial W/\partial I_2$ is independent of I_1 but decreases with increase of I_2. From that, they concluded that appropriate strain-energy functions should take the form

$$W = C\left(I_1 - 3\right) + f\left(I_2 - 3\right), \tag{6.11}$$

where C is a constant.

Rivlin and Sawyers [115] proposed a specific form of W, namely,

$$W = C_1\left(I_1 - 3\right) + C_2\left(I_2 - 3\right) + C_3\left(I_2 - 3\right)^2, \tag{6.12}$$

where C_1 and C_2 are positive constants and C_3 is a negative constant, for specific ranges of I_1 (5 to 11) and I_2 (5 to 30). It should be noted that form (6.12) is not valid for lower values of I_1 and I_2.

Gent and Thomas [41] proposed the strain energy function form

$$W = C_1\left(I_1 - 3\right) + C_2 \log\left(\frac{1}{3}I_2\right) \tag{6.13}$$

which, for a suitable choice of the material constants C_1 and C_2 describes the behavior of rubber-like materials over a much broader range of deformation than the Mooney form does.

Obata et al. [101] attempted to extend Rivlin's constitutive equation in order to quantify the effect of crosslinking on the shape of the response functions. They arrived at new response functions,

$$\begin{aligned}\frac{\partial W}{\partial I_1} &= C_1 + \frac{C_2}{\left(I_1-3\right)^2} - \frac{C_3\left(I_2-3\right)}{\left(I_1-3\right)^{2.5}} \\ \frac{\partial W}{\partial I_2} &= C_4 + \frac{C_5}{\left(I_2-3\right)} - \frac{2C_3}{3\left(I_1-3\right)^{1.5}}\end{aligned} \tag{6.14}$$

where C_1 to C_5 are material constants.

Departing from the Rivlin's approach of describing the strain-energy function in terms of principal invariants, Valanis and Landel [161] postulated that the strain energy function, for incompressible isotropic materials, should be a separable symmetric function of the principal stretch ratios, instead of the strain invariants, i.e.

$$W = w\left(\lambda_1\right) + w\left(\lambda_2\right) + w\left(\lambda_3\right) \tag{6.15}$$

where the function $w\left(\lambda_i\right)$ by symmetry is the same for each stretch ratio. This form of W was proved to be valid over a large deformation range $(0.2 \leq \lambda_i \leq 3.5)$. Using this postulate and unpublished data by Becker and Landel, and other there sources of experimental data by Rivlin and Saunders [114], Treloar [152] and Blatz and Ko [12], they proposed an analytical form of the function W over a more limited range of stretch ratio $(0.6 \leq \lambda \leq 2.5)$,

$$W = 2\mu \sum_{i=1}^{3} \lambda_i \left(\log \lambda_i - 1\right) \tag{6.16}$$

where μ is the shear modulus.

Based on Valanis-Landel hypothesis, Ogden [102] proposed a special form of W as

$$W = \sum_i \frac{\mu_i}{\alpha_i} \left(\lambda_1^{\alpha_i} + \lambda_2^{\alpha_i} + \lambda_3^{\alpha_i} - 3 \right) \tag{6.17}$$

where μ_i and α_i are material parameters. α_i may take any non-zero real value. The summation on i extends over as many terms as are necessary to characterize a particular material [50]. It was shown that Ogden's strain energy function provides a good agreement with Treloar's data.

Table 6.1 summarizes the phenomenological constitutive relations of rubber-like materials.

6.2 Method

6.2.1 Finite inflation test for a rubber balloon

The experimental system designed for inflation tests consists of a gas cylinder with compressed nitrogen gas, a U-tube manometer, a Nikon D80 digital SLR camera, and a close-range photogrammetry software, PhotoModeler (EOS Systems Inc.). Figure 6.1 illustrates schematically the experimental system.

A finite element mesh which constitutes 12×12 four-node elements was drawn by hand using a fine marker pen on the belly region of the balloon surface. Compressed nitrogen gas was used to inflate the balloon. Before testing, the rubber balloon underwent cyclical inflation-deflation (preconditioning) for 10 times to eliminate the Mullin's effect. Subsequently, the balloon was inflated to a relative large size of approximately 200% stretch. After several seconds waiting for the balloon to reach

Table 6.1: Summary of phenomenological constitutive relations of rubber-like materials.

Author	Constitutive Equation	Data
Mooney [96] (1940)	$W = C_1 (I_1 - 3) + C_2 (I_2 - 3)$	Gerke [42]
Rivlin & Saunders [114] (1951)	$W = C (I_1 - 3) + f (I_2 - 3)$	Rivlin & Saunders [114]
Gent & Thomas [41] (1958)	$W = C_1 (I_1 - 3) + C_2 \ln \left(\frac{I_2}{3}\right)$	Gent & Thomas [41]
Hart-Smith [52] (1966)	$\frac{\partial W}{\partial I_1} = Gexp \left[k_1 (I_1 - 3)^2\right]$ $\frac{\partial W}{\partial I_2} = \frac{Gk_2}{I_2}$	Treloar [152], Rivlin & Saunders [114]
Alexander [3] (1968)	$W = C_1 \int e^{k(I_1-3)^2} dI_1 +$ $C_2 \ln \left(\frac{(I_2-3)+\gamma}{\gamma}\right) + C_3 (I_2 - 3)$	Alexander [3]
Rivlin & Sawyers [115] (1976)	$W = C_1 (I_1 - 3) + C_2 (I_2 - 3) +$ $C_3 (I_2 - 3)^2$	Rivlin & Saunders [114]
Valanis & Landel [161]	$W = 2\mu \sum_{i=1}^{3} \lambda_i (\log \lambda_i - 1)$	Becker & Landel
Ogden [102] (1972)	$W = \sum_{i=1}^{3} \frac{\mu_i}{\alpha_i} (\lambda_1^{\alpha_i} + \lambda_2^{\alpha_i} + \lambda_3^{\alpha_i} - 3)$	Treloar [152]

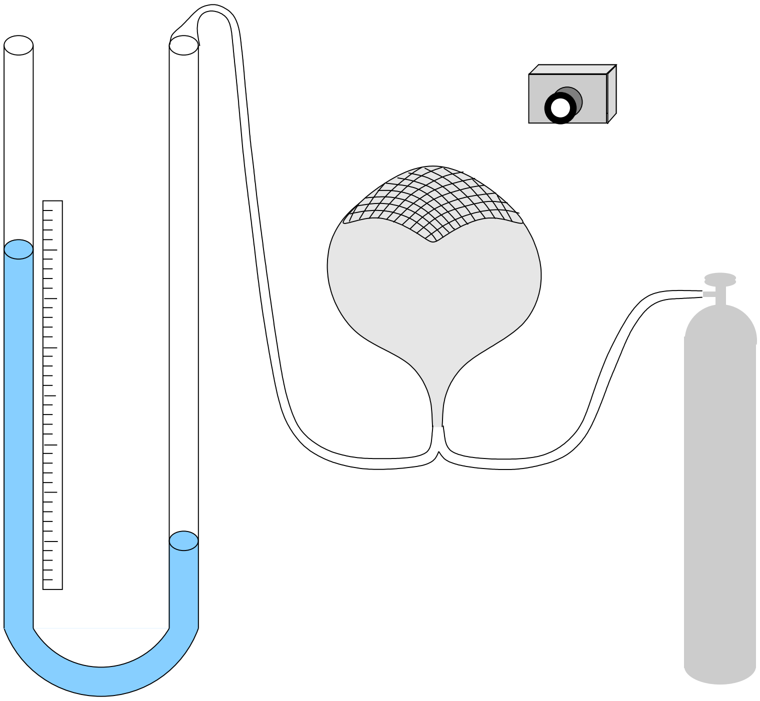

Figure 6.1: Schematic illustration of the experimental system.

its stable status, the balloon was deflated in several decrements. At each state, the air pressure inside the balloon was measured using a manometer. In the meantime, four photos were taken from different perspectives using a Nikon D80 digital SLR camera which was calibrated prior to the test. Since the balloon generally collapses when the net internal pressure is zero, the configuration under a very small pressure (0.0001 N/mm^2), but still in convex shape, was taken as the approximate stress-free configuration. Fourteen configurations, including the stress-free configuration and thirteen deformed configurations, were recorded.

6.2.2 Photogrammetric surface reconstruction

Photogrammetry encompasses methods of image interpretation in order to derive the shape and location of an object from one or more photographs of that object [91]. A primary purpose of photogrammetric measurement is the three dimensional reconstruction of an object in digital form. Photogrammetry works as follows. First, the camera needs to be calibrated, which allows the photogrammetry program to know the detailed description of the camera, including the focal length, imaging scale, image center and lens distortion. Second, the user takes enough photographs of the object from different perspectives, which can sufficiently characterize its 3D structure. Third, the photographs are imported into the program, and point referencing is then performed to let the program know the corresponding positions in each 2D image space of a point in the 3D space. Finally, the 3D position of all the selected points are computed using mathematical transformation. If applied to a deforming membrane with enough tracking markers on its surface, which sufficiently characterize the geometry feature of membrane, photogrammetry can be used to record the 3D positions of the tracking markers in different deformed states. By identifying a reference configuration, one can obtain the displacements of the tracking markers, and hence compute the strains using interpolation.

Taking the photos as input, we used a close-range photogrammetry program, PhotoModeler 6 (EOS Systems Inc.), to reconstruct the 3D surface geometry of the meshed region in each configuration. In the process of 3D geometry reconstruction, an important step is the determination of the point-to-point correspondence between the tracking points in different photographs. Due to the difficulty in corresponding the nodes across different photographs automatically, we determined the point-to-point correspondence by manually picking the points using mouse.

6.2.3 Computation of stress

Taking the reconstructed finite element mesh of each deformed configuration, we computed individually the wall tension using FEIEM described in §3.4. We employed the strain energy function, Equation (5.1), i.e.

$$w = \frac{\nu_1}{2}\left(I_1 - 2\log J - 2\right) + \frac{\nu_2}{4}\left(I_1 - 2\right)^2 . \tag{6.18}$$

and assumed unrealistic values of the elasticity parameters, $\nu_1 = \nu_2 = 100$ N/mm which rendered a very small deformation, For the sake of quick convergence. The reason that we use different notation ν_1 and ν_2 from those in Equation (5.1) for the elastic parameters is to distinguish from the notation in Ogden's model, which are μ_i.

Clamped boundary conditions were applied on the four edges of the mesh. As discussed in [89, 180], clamped boundary (or other types of displacement constraints) compromises the stress static determinacy. However, for sufficiently curved membranes the influence exists in a thin boundary layer [118, 174], and the thickness of which depends inversely on the surface curvature. Outside the boundary layer, the stress is asymptotic to the static solution. We hypothesize that the boundary layer can be identified numerically by examining the change of stress induced by the variation of the material parameters. The region in which the stress remains approximately invariant under relatively large change of material parameters is defined as the boundary-effect-free region. Later, the parameter identification will be carried out in the boundary-effect-free region only. This procedure is important to the experiment design, as we need a practical method to eliminate the influence of boundary effect.

In the inverse stress analysis the stress $\mathbf{t}$ is computed at each Gauss point in a local orthonormal coordinate system, and thus the outputs are the physical components which we denoted as t_{11}, t_{22}, $t_{12} = t_{21}$. The principal stresses, which will be used in parameter regression, can be directly computed according to

$$\begin{aligned} t_1 &= \frac{t_{11}+t_{22}}{2} + \frac{\sqrt{\left(t_{11}-t_{22}\right)^2 + 4t_{12}^2}}{2}, \\ t_2 &= \frac{t_{11}+t_{22}}{2} - \frac{\sqrt{\left(t_{11}-t_{22}\right)^2 + 4t_{12}^2}}{2}. \end{aligned} \tag{6.19}$$

6.2.4 Computation of strain

Based on the measured nodal positions in the reference and deformed configurations, we approximated the position vectors of a point inside the meshed region via the finite element interpolation (cf. Equation (4.1)). Following the formulation in §4.1.1, the base vectors ($\mathbf{G}_\alpha$, $\mathbf{G}^\alpha$, $\mathbf{g}_\alpha$, and $\mathbf{g}^\alpha$) and metric tensor components ($G_{\alpha\beta}$, $G^{\alpha\beta}$, $g_{\alpha\beta}$, and $g^{\alpha\beta}$) in the undeformed and deformed configurations were computed. Finally, the principal stretch ratios λ_1 and λ_2 at each Gauss point were computed according to Equation (4.4).

6.2.5 Isotropy test

For materials in some symmetry classes, the stress function should satisfy certain *universal relations* [54, 9, 10, 108, 113]. For experimentalists, the universal relations are important in determining whether a material belongs to a certain symmetry class. For isotropic elastic materials, the relation

$$\mathbf{SC} = \mathbf{CS} \tag{6.20}$$

holds, which implies that the second Piola-Kirchhoff stress tensor $\mathbf{S}$ commutes with the right Cauchy-Green deformation tensor $\mathbf{C}$ in every possible motion. Giving the linear relation between $\mathbf{S}$ and referential tension $\mathbf{T}$, it is clear that $\mathbf{T}$ must satisfy

$$\mathbf{TC} = \mathbf{CT}. \tag{6.21}$$

This is the *universal relation* for isotropic membranes.

Utilizing the acquired tension-strain data, we may examine whether $\mathbf{TC} = \mathbf{CT}$ holds. Due to the experimental error, $\mathbf{TC} - \mathbf{CT}$ will not be exactly zero even if the material is truly isotropic. We employ the commutator $\mathbf{e} = \mathbf{TC} - \mathbf{CT}$ as an indicator for isotropy. Due to the symmetry of $\mathbf{T}$ and $\mathbf{C}$, the components $e_{11} = e_{22} = 0$, and the only possible non-zero component is e_{12}. We introduce the function $\varepsilon = \frac{2|e_{12}|}{\|\mathbf{TC}-\mathbf{CT}\|} \times 100$ as a measure of co-axiality. If ε is close to zero for a wide range of stress-strain protocols, we may say the universal relation is satisfied. Obviously, the test alone cannot conclude material isotropy, especially if only limited stress-strain protocols are tested. However, if the universal relation is found to hold true for a rich family of stress-strain protocols, then there is a strong justification to model the material as isotropic.

6.2.6 Elastic parameter identification

The mechanics of rubber elasticity has been investigated extensively in the last several decades, and various constitutive models have been developed. Among the well-known hyperelastic descriptors, there are mainly two types of energy functions, one in terms of the strain invariants [112, 47] and the other in principal stretches [152, 161, 102, 105]. Attributing to the limited extensibility of the molecule chain network, the stress-stretch curve shows a characteristic sigmoid shape [155]. Our experimental stress-stretch data displayed the same characteristic as that by Treloar [152]. It has been well-accepted that the Ogden's energy function [102], which contains non-integer powers of the principal stretches, can model the sigmoid shape well within the typical range of experimental stretches. Based on this consideration, we selected the Ogden model to fit our experimental data.

The Ogden model describes the strain-energy function in terms of the principal stretches λ_r $(r = 1, 2, 3)$, in the following form

$$W = \sum_i \frac{M_i}{\alpha_i} \left(\lambda_1^{\alpha_i} + \lambda_2^{\alpha_i} + \lambda_3^{\alpha_i} - 3 \right). \tag{6.22}$$

Here, W is the strain energy per unit reference volume, M_i and α_i are elastic parameters. The exponents α_i may take any non-zero real value. The summation on

i extends over as many terms as are necessary to characterize a particular material [50]. For membranes, the strain energy per unit reference area is $w = HW$, where H is the reference membrane thickness. Hence, the 2D form of (6.22) is

$$w = \sum_i \frac{HM_i}{\alpha_i} \left(\lambda_1^{\alpha_i} + \lambda_2^{\alpha_i} + \lambda_3^{\alpha_i} - 3\right). \tag{6.23}$$

We introduce the effective elasticity parameters, $\mu_i = HM_i$, and rewrite (6.23) as

$$w = \sum_i \frac{\mu_i}{\alpha_i} \left(\lambda_1^{\alpha_i} + \lambda_2^{\alpha_i} + \lambda_3^{\alpha_i} - 3\right). \tag{6.24}$$

The incompressibility condition, $\lambda_1\lambda_2\lambda_3 = 1$, gives rise to $\lambda_3 = \left(\lambda_1\lambda_2\right)^{-1}$. Considering λ_1 and λ_2 two independent deformation parameters, we may rewrite function (6.24) as

$$\hat{w}\left(\lambda_1, \lambda_2\right) = \sum_i \frac{\mu_i}{\alpha_i} \left(\lambda_1^{\alpha_i} + \lambda_2^{\alpha_i} + \lambda_1^{-\alpha_i}\lambda_2^{-\alpha_i} - 3\right). \tag{6.25}$$

It follows that under the plane stress assumption ($t_3 = 0$) the principal values of the tension tensor are given by

$$t_1 = \frac{1}{\lambda_2}\frac{\partial \hat{w}}{\partial \lambda_1}, \quad t_2 = \frac{1}{\lambda_1}\frac{\partial \hat{w}}{\partial \lambda_2}. \tag{6.26}$$

Expanding equation (6.26), we obtain

$$\begin{aligned} t_1 &= \sum_i \mu_i \left(\lambda_1^{\alpha_i - 1} \lambda_2^{-1} - (\lambda_1 \lambda_2)^{-\alpha_i - 1} \right), \\ t_2 &= \sum_i \mu_i \left(\lambda_2^{\alpha_i - 1} \lambda_1^{-1} - (\lambda_1 \lambda_2)^{-\alpha_i - 1} \right). \end{aligned} \tag{6.27}$$

It was shown by Ogden [102] that the energy function (6.24) fits well the data of a particular rubber material by Treloar [152] if three terms are included. Following this observation, we chose the three-term Ogden model in this work.

The objective function is constructed as

$$\Phi = \sum_{i=1}^{N} w_1 \left({}^{(i)}t_1 - {}^{(i)}\hat{t}_1 \right)^2 + w_2 \left({}^{(i)}t_2 - {}^{(i)}\hat{t}_2 \right)^2 \tag{6.28}$$

where, N is the number of deformed states recruited into the regression, ${}^{(i)}t_\alpha$ and ${}^{(i)}\hat{t}_\alpha$ $(\alpha = 1, 2)$ are the model predicted and experimental principal tensions (computed from the inverse method) in the ith configuration, w_1 and w_2 are the weight parameters, the values of which are determined by numerical experiments. To achieve the reported results, we chose $w_1 = 1.0$ and $w_2 = 1.5$. Since an approximate global stress-free configuration was obtained, Φ is a function of the unknown elasticity parameters only. The parameter identification problem can be described as

$$\begin{aligned} &\text{minimize} \quad \Phi(\boldsymbol{\mu}, \boldsymbol{\alpha}) \\ &\text{subject to} \quad \mathbf{l} \le (\boldsymbol{\mu}, \boldsymbol{\alpha}) \le \mathbf{u}. \end{aligned} \tag{6.29}$$

Here, $(\boldsymbol{\mu}, \boldsymbol{\alpha}) = (\mu_1, \mu_2, \mu_3, \alpha_1, \alpha_2, \alpha_3)$ is the vector of elasticity parameters, $\mathbf{l}$ and $\mathbf{u}$

are the vectors of lower and upper bounds of $(\boldsymbol{\mu}, \boldsymbol{\alpha})$.

A practical difficulty in material parameters identification is that multiple sets of parameters may render equally good fits to a given set of stress-strain data due to the presence of local minima or experimental error or regression error [143]. The problem aggravates for highly nonlinear models, as a small perturbation in the experimental data may result in a large variation in the ensuing parameters. This issue has a nontrivial implication in membrane identifications. While the 3D energy function parameters are intrinsic properties of the material, the effective properties in the membrane energy function, such as μ_i in Equation (6.24), are not. Their values depend on the wall thickness, and thus may vary with the thickness even if the underlying material is intrinsically homogeneous. Due to the numerical non-uniqueness in fitting, a variation in the wall thickness may result in a spurious heterogeneity in the identified intrinsic parameters. To cope with this difficulty, we adopted the following strategy. We first performed regression at a selected point where the response was relatively smooth and determined the parameters α_i and μ_i. Then, based on the consideration that the balloon is approximately homogeneous, we applied the values of α_i to all other points and identified the remaining effective parameters μ_i. Although the parameters so obtained are unlikely the global minimizer of the objective function, the (assumed) intrinsic homogeneity is enforced. The regression was performed by a gradient-based, sequential quadratic programming (SQP) algorithm, SNOPT [43].

6.2.7 Predictive capability

The usefulness of the identified elastic parameters can be evaluated by examining how well the model derived from a set of experiments can predict the system behavior in a different physical setting [68]. We conducted a forward finite element analysis using the identified model to predict a deformed configuration which was not used in the parameter identification. The FEM predictions were compared to the measured deformation. In the forward analysis we followed the finite element formulation of the Ogden model for membrane problems presented by Gruttmann and Taylor [50], and implemented the element in the nonlinear finite element program FEAP [147].

The forward finite element analysis was conducted for the boundary-effect-free region where the parameter identification was carried out. The identified parameters α_i and the averages of the identified parameters μ_i over the region were input as the model parameters. The displacements of the boundary nodes were prescribed according to the recorded nodal positions. The difference between the predicted position $\mathbf{x}$ and measured position $\hat{\mathbf{x}}$ was quantified node-wise with the error measure $e = \frac{\|\mathbf{x}-\hat{\mathbf{x}}\|}{L}$, where L is a characteristic length taken to be 10 cm.

6.3 Results

6.3.1 Reconstructed surfaces and stress results

Table 6.2 lists the thirteen deformed configurations and their corresponding pressure values. The largest stretch being around 2.1 occurred in the configuration 13 (the highest pressure). The initial size of a randomly selected element in the stress-

Table 6.2: The identities and corresponding pressure values of the deformed configurations.

Configuration ID	1	2	3	4	5
Pressure (N/mm^2)	0.00089	0.00134	0.00153	0.00161	0.00167
Configuration ID	6	7	8	9	10
Pressure (N/mm^2)	0.00173	0.00179	0.00184	0.00190	0.00198
Configuration ID	11	12	13		
Pressure (N/mm^2)	0.00208	0.0022	0.00238		

free configuration is about 5.3×5.3 mm^2, whereas in the deformed configuration 13, its size is around 10.6×10.6 mm^2. Figure 6.2 shows a typical photo used in the process of 3D geometry reconstruction. The 3D reconstruction was performed successfully. Take the central node (node 85) as an example, the coordinates and precisions in the X, Y, and Z directions are X : 65.05 ± 0.029 mm, Y : 51.46 ± 0.053 mm, and Z : 161.07 ± 0.089 mm, respectively. The confidence interval is 0.68. Figure 6.3 shows the reconstructed mesh for the deformed configurations. Two deformed configurations which were close to other ones are not shown. Qualitatively, the convexity and smoothness of membrane surfaces have been recovered.

Figure 6.4 shows the finite element mesh and the principal tensions in the 13th state (the highest pressure). It should be noted that the stress solution obtained through the inverse method is largely affected by the geometric features of the surface, e.g. smoothness and curvature. Due to the unavoidable existence of experimental error, the reconstructed membrane surface may have some unphysical local undulations depending on the accuracy of the motion tracking devices. In that case, the stress solution may not converge, or has stress concentrations here and there.

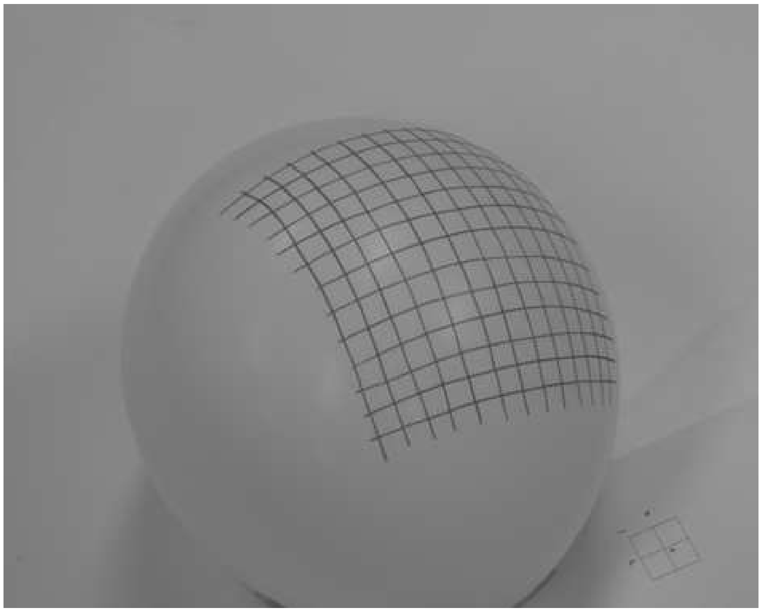

Figure 6.2: A photo of the rubber balloon used in the process of 3-D geometry reconstruction.

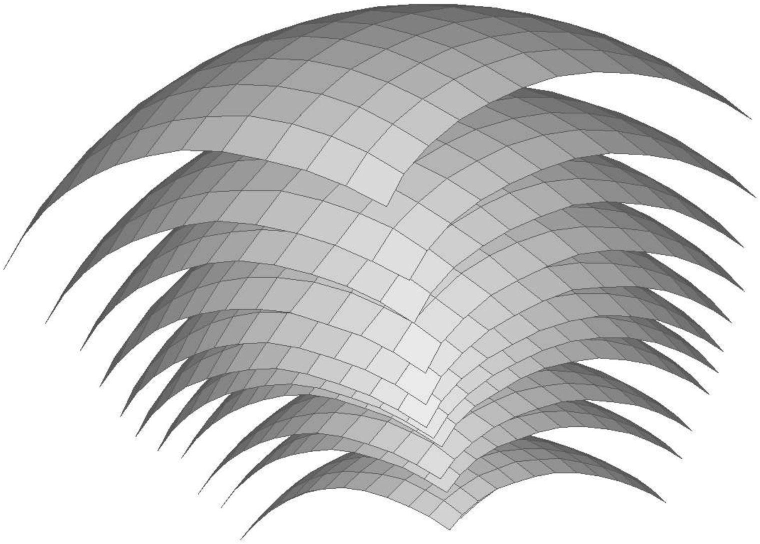

Figure 6.3: Reconstructed meshes of the deformed configurations.

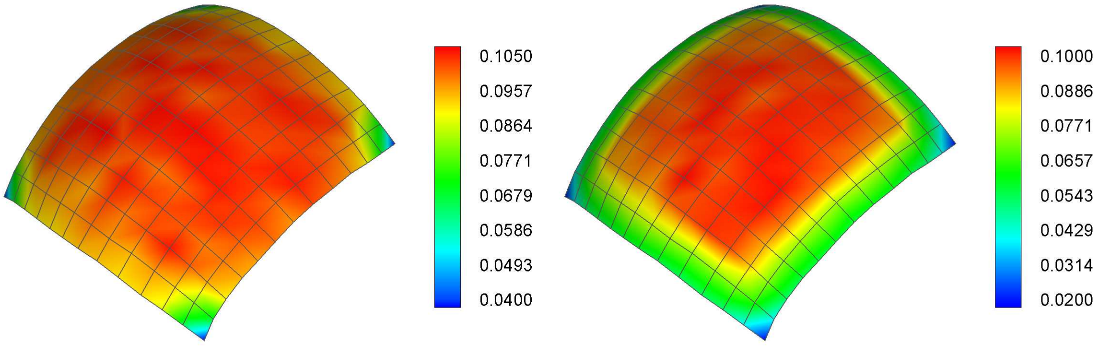

(a) (b)

Figure 6.4: Distribution of principal tensions in deformed configuration 13: (a) t_1, (b) t_2.

In order to reduce this artifact, it is imperative that certain surface smoothing processes be conducted prior to stress computation. In this work, we were able to obtain good quality surface meshes from 3D reconstruction without modification for all the configurations.

6.3.2 Stress sensitivity to material model

Figure 6.5 shows the relative difference (in percentage) of the principal tensions under drastic changes in elasticity parameters of the neo-Hookean model. We took the parameters $\nu_1 = \nu_2 = 100$ N/mm as the reference values. After varying the two parameters in different ways, we computed the principal tensions using the inverse method, and compared them with those computed from the reference parameters. In Figure 6.5, the upper row shows the percentage difference in principal stresses when both parameters were magnified 10 times, i.e. $\nu_1 = \nu_2 = 1000$ N/mm. The percentage differences in the region three layers of elements distanced from the boundary were

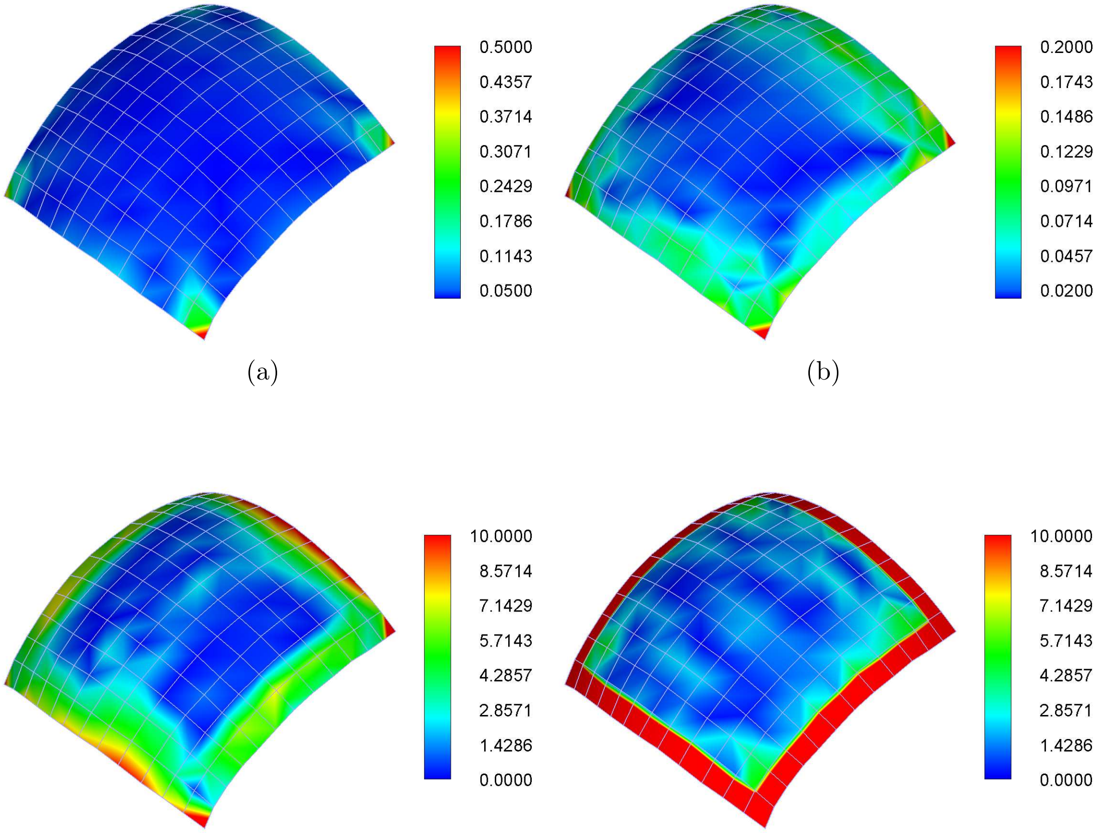

(a) (b)

(c) (d)

Figure 6.5: The percentage difference of principal tensions under the change of elasticity parameters. Upper row: Increasing both parameters μ_1 and μ_2 to 10 times: (a) t_1, (b) t_2; Lower row: Keeping μ_1 unchanged and increasing μ_2 to 5 times: (c) t_1, (d) t_2.

below 0.05%. Increasing both parameters by 100 times produces a similar difference margin, and we do not report here. In the lower row, ν_1 was kept unchanged, while ν_2 was increased to 5 times, i.e. $\nu_1 = 100$ N/mm and $\nu_2 = 500$ N/mm. The percentage differences in the region three layers of elements distanced from the boundary were below 2.8%. The case where ν_1 was increased to 5 times while ν_2 remained unchanged was also considered and a similar margin of difference was observed.

Throughout all the tests, it appears that the tension solution was affected minimally by proportional variations of the elastic parameters. Changing two parameters unproportionally, however, rendered a relatively larger variation in the tension solution. Nevertheless, the difference was within an acceptable range in the region three layers of elements distanced from the boundary. This region was identified as the boundary-effect-free region where the parameter identification was performed later.

6.3.3 Isotropy test

Figure 6.6(a) and (b) show the distribution of the co-axiality indicator ε in the lowest and highest pressure states (configurations 1 and 13), respectively. In the boundary-effect-free region defined above, the value of ε was less than 0.58% and 1.07% for the configurations 1 and 13, respectively. The values in other states fall into these limits. Allowing for the experimental error, we conclude that the co-axiality condition between the stress and strain tensors was met. Therefore, the rubber may be modeled as isotropic material.

6.3.4 Elastic parameter identification

As introduced in §6.2.6, the parameter identification was accomplished in two steps. First, the regression was performed at a selected Gauss point and all parameters were identified. Second, the identified α_i values were applied to the entire region, and the remaining parameters μ_i were identified at all remaining Gauss points. The identified values of α_i and μ_i at the selected point are listed in Table 6.3.

The global regression was performed using the states in Table 1 excluding the

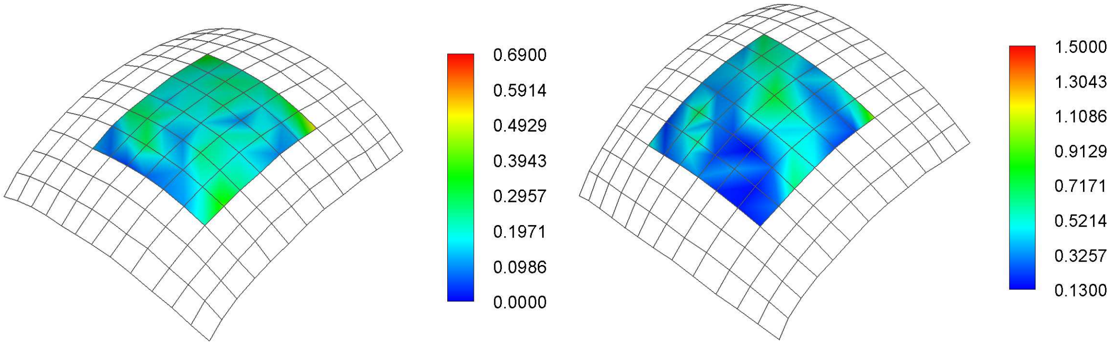

(a) (b)

Figure 6.6: The distribution of the co-axiality indicator ε in selected configurations: (a) Configuration 1; (b) Configuration 13. Both figures were scaled to fit the canvas for clarity.

Table 6.3: The identified parameters α_i and μ_i for the Ogden model at a selected point.

i	α_i	μ_i (N/mm)
1	2.87181	0.05827
2	-1.80776	0.01940
3	-5.76831	-8.477×10^{-5}

11th state ($p = 0.00208$ N/mm^2), which was reserved for a forward verification. The distributions of the identified parameters μ_i in the whole region are shown in Figure 6.7 for the boundary-effect-free region. The ranges, means, and standard deviations of these three parameters are listed in Table 6.4. Since the standard deviations for all the parameters are relatively small, we may conclude that the material is at least nominally homogeneous.

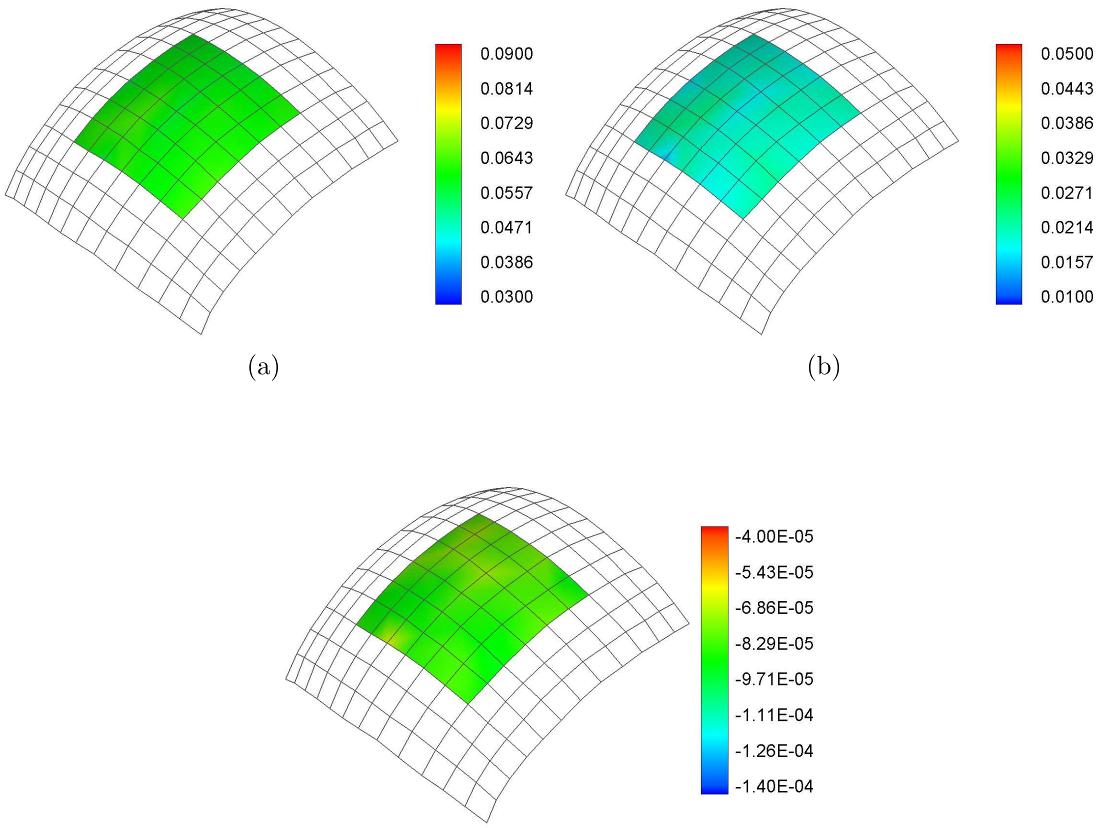

(a)

(b)

(c)

Figure 6.7: Identified elasticity parameters of the Ogden model: (a) μ_1, (b) μ_2, (c) μ_3.

Table 6.4: Ranges, means, and standard deviations of the identified elasticity parameters.

	μ_1	μ_2	μ_3
Minimum (N/mm)	0.05470	0.01473	-9.454×10^{-5}
Maximum (N/mm)	0.06453	0.02320	-6.221×10^{-5}
Mean (N/mm)	0.05986	0.01966	-8.154×10^{-5}
SD (N/mm)	0.00239	0.00171	6.923×10^{-6}

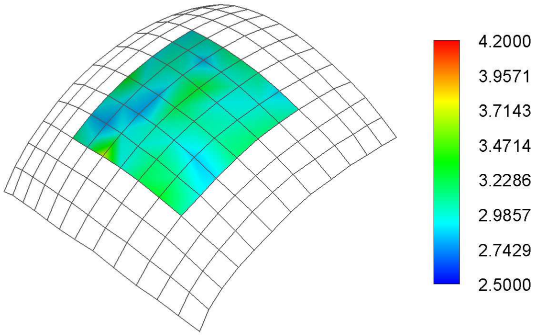

Figure 6.8: Distribution of the ratio of μ_1 to μ_2.

The intrinsical homogeneity of the material can be checked by inspecting the ratios $\frac{\mu_1}{\mu_2}$, $\frac{\mu_1}{\mu_3}$, and $\frac{\mu_3}{\mu_2}$, which factor out the wall thickness. Since μ_3 is several orders of magnitude smaller than μ_1 and μ_2, we only examine the ratio of μ_1 to μ_2. The distribution of this ratio is illustrated in Figure 6.3.4. Qualitatively seen from the figure, the ratio is approximately uniform over the region. The mean is 3.0309 N/mm, and the standard deviation is 0.1720 N/mm. The result suggests that the material is intrinsically homogeneous.

Figure 6.9 illustrates the comparison between the identified model's tension-stretch curves and the experimental data, at the point where the initial identification of all the six parameters took place. The good match between the model-predictions and experimental data indicates that the material's response were modeled successfully by the Ogden model, at least within the stretch range considered in the experiment.

6.3.5 Predictive capability

The 11th configuration ($p = 0.00208$ N/mm^2), which has been excluded from parameter identification, was recruited for a forward verification. Figure 6.10 shows the comparison between the finite element predicted configuration using the identified mean elastic parameters and the experimentally measured configuration. In the left plot, the thick black mesh is the finite element prediction, and the thin gray mesh is the experimental result. The finite element analysis was performed for the boundary-effect-free region where the elastic parameter identification was conducted. Displacement boundary condition corresponding to the measured nodal positions were applied along the boundary edges. The right plot shows the distribution of the relative error between the predicted and measured nodal positions. As shown in the plots, the computed configuration coincides very well with the experimentally measured one. The position error $e = \frac{\|\mathbf{x}-\hat{\mathbf{x}}\|}{L}$ is less than 0.2% throughout the region.

6.4 Discussion

In principle, multiple experiments should be conducted for a population of objects and the results need to be averaged when one characterizes the elastic properties of a specific material due to inevitable experimental error and specimen-to-specimen

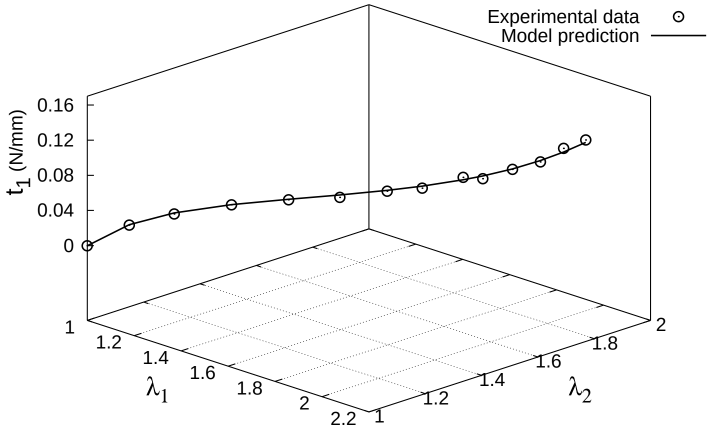

(a)

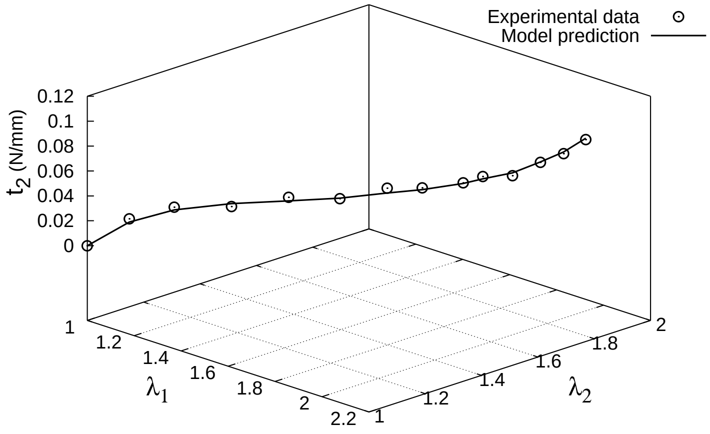

(b)

Figure 6.9: Comparison between the experimental and the modeled tension curves: (a) t_1; (b) t_2.

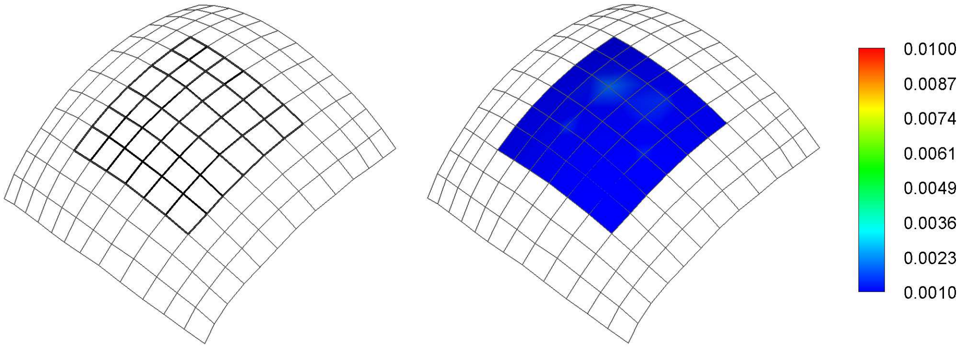

(a) (b)

Figure 6.10: Comparison between the deformed configuration computed from finite element method using the identified elastic parameters and the experimentally measured configuration. (a) Thin gray mesh: experimental (whole domain); Thick black mesh: finite element modeled (boundary-effect-free region); (b) Distribution of the position error $e = \frac{\|\mathbf{x}-\hat{\mathbf{x}}\|}{L}$.

variance. In our experiment, we only conducted a single test. The reason for this is three-fold. First, our objective here is to test the validity and effectiveness of the method in identifying the elastic properties of a specific object instead of obtaining the realistic elastic parameters for specific materials, so there is no need to evaluate it for other objects. Later in application, if one needs to identify the population mean elastic parameters for specific materials or soft tissues, multiple specimen will be considered. Second, the data processing is tedious although the experiment itself is not complicated. During the 3D reconstruction using photogrammetry software, the point-to-point reference among multiple (more than three) needs to be made by hand due to lack of automation. Third, the obtained stress-strain curves at interested regions for the single specimen used are relatively smooth, and it is reasonable to conclude the data are reliable enough.

CHAPTER 7
NUMERICAL EXPERIMENTS: CEREBRAL ANEURYSMS

7.1 Introduction

Cerebral aneurysms are focal dilatations of the intracranial arterial wall that usually develop in or near the circle of Willis. Non-complicated cerebral aneurysms are typically thin-walled. Their diameters range from a few to a few tens of millimeters while the wall thicknesses range from tens to hundreds of micrometers [126, 67]. In their service environment, these lesions are best described as elastic membranes subjected to transmural pressure and hemodynamic shear stress. While the long term growth and remodeling is likely modulated by the lumen shear stress, the sudden bleed or rupture is believed to be caused by the pressure induced wall stress. Rupture likely occurs at the spot where the wall stress exceeds the wall strength. Historically, the size has been used as an indicator for evaluating rupture risk [25, 73, 157, 171, 35]; recently it is believed that shape may provide a more reliable prediction [158, 159, 110].

Due to its significance in predicting the rupture risk of aneurysms, the determination of the wall stress distribution has become an active research subject. Many works have been reported to determine wall stress distribution in aneurysms of hypothetical shape, e.g. cylinder and sphere. These include Stringfellow et al. [142], Inzoli et al. [70], Mower et al. [98], Elger et al. [32]. However, every single cerebral aneurysm has its own size, geometry, wall thickness, elastic property, and extension strength. Therefore, the value of the maximum wall stress and the location where it occurs is different from patient to patient, and so is the rupture risk of the aneurysm. Accordingly, ideal evaluation of rupture risk would be to determine the wall stress under in vivo blood flow condition with patient-specific geometry, wall thickness and elastic properties, and then check if the maximum wall stress will exceed the wall strength soon. Current imaging segmentation techniques allow for in vivo reconstruction of the three-dimensional geometry of cerebral aneurysms [92, 16], although patient specific aneurysm wall thickness is still an unsolved problem.

Towards the direction of in vivo stress analysis for patient-specific aneurysms, some representative studies have emerged. Raghavan et al. [111] developed a method to noninvasively estimating the in vivo wall stress distribution in patient-specific abdominal aorta aneurysms (AAAs), utilizing 3D reconstruction with medical images and finite element method. Isaksen et al. [71] performed finite element isogeometric analysis to determine wall tension in cerebral aneurysms using fluid-structure interaction. For stress analysis using forward or direct finite element method like Raghavan et al. [111] and Isaksen et al. [71], however, detailed information on the material properties and wall thickness are needed. Unfortunately, the heterogeneous material property and wall thickness are very difficult to characterize and hence, one often has to adopt population-averaged material properties retrieved from uniaxial or biaxial specimen testing or in vitro inflation experiments on ruptured aneurysms, and an estimation or a population-average of the wall thickness. It is not hard to imagine that such analyses could give rise to unrealistic stress estimation in the aneurysm wall, which may in turn yield unreliable estimation of rupture risk.

More often than not, the geometries of aneurysms used in determining the wall stress distribution are stressed configurations due to the fact that the stress-free configuration is never reached in vivo. The outcome of this factor is that an initial stress is added to the computed stress, rendering an overestimation of the realistic stress values. Therefore, the determination of the stress-free configuration of aneurysms is very important. Lu et al. [88] proposed an inverse approach to determine the stress-free configuration of an abdominal aortic aneurysm, and subsequently obtained the wall stress distribution. Their approach is based on a finite element inverse elastostatics formulation, which takes as input a deformed configuration and seeks a stress-free configuration. However, the sought stress-free configuration is not necessarily realistic unless the realistic elastic parameters are input to the inverse finite element analysis. In [88], population mean elastic parameters were used which were identified from *ex vivo* experiments. Therefore, the so obtained stress-free configuration was considered the realistic one.

Pursuing the same goal while taking a different path, Lu et al. [89] proposed a method to determine the in vivo wall stress distribution in a cerebral aneurysm by utilizing finite element inverse elastostatics method for membrane structures without *a priori* knowledge of the realistic stress-free configuration and elastic properties. Their method hinges on the statically determinate feature of membrane equilibrium problem, i.e. the stress can be determined from the balance equation alone. This work is the cornerstone of the pointwise identification method that this thesis is proposing.

Regardless the capability of the aforementioned methods in identifying the stress distribution of cerebral aneurysms, the detailed information on the wall material property still is of great interest. However, delineating the elastic property of aneurysm tissue, in particular, experimental determination of the material parameters, presents some significant challenges. The lesion wall typically consists of multiple layers of type I and III collagen fibers with varying orientations that form two-dimensional networks [13, 93]. Variation in microstructure and remodeling history gives rise to spatially varying stiffness and symmetry characteristics. At the continuum level, aneurysm tissue is typically characterized as nonlinear, anisotropic, and heterogeneous over finite strain. Among these characteristics, heterogeneity perhaps poses the most difficulty to experiments.

Despite the critical importance of constitutive parameters to understanding aneurysm mechanical behavior, reports on cerebral aneurysm wall property have been scarce. Earlier studies focused mainly on global property (e.g., pressure-volume relation) [125], or uniaxial and biaxial stress behavior of exercised strips and sheets [141, 148]. Hsu et al. [62, 61] studied the pressure-deformation behavior of two intracranial cerebral aneurysms harvested as a whole from cadavers, and reported multiaxial deformations at multiple locations under varying pressures. In recent years, several studies have been conducted to characterize the heterogeneous material property in cerebral aneurysms. Humphrey's group [126, 128] developed the inverse finite element method, and applied it to delineate the regional properties in a harvested aneurysm, and obtained best-fit material parameters in a Fung-type strain-energy function for a cerebral aneurysm sac. Their work remains to this date the the most complete report on the heterogeneous properties in cerebral aneurysms.

Recently, Kroon and Holzapfel [77] reported an inverse finite element identification of anisotropic heterogeneous elastic properties in idealized cerebral aneurysms. In this chapter, we will validate the method for anisotropic material using the cerebral aneurysm model. The validation procedure is the same as that of the isotropic case considered in Chapter 5 except that the material model is anisotropic and the material is assumed to have a certain pattern of heterogeneity. We chose the constitutive model proposed by Holzapfel et al. [60] which is a structural model suitable for fiberous biological tissues.

Basically, a virtual (numerical) test is conducted to demonstrate and evaluate the utility of PWIM in cerebral aneurysms. The procedure is illustrated in Figure 7.1. Forward finite element analysis is applied first to a cerebral aneurysm sac of known material property and geometry to generate a series of deformed states. The FE model of the aneurysm sac is shown in Figure 7.2 including the initial configuration and a deformed configuration under the highest pressure (p=110 mmHg). Clamped boundary condition is applied at the neck of the aneurysm, to mimic a common setting in experiment. The assumed distribution of heterogeneous elastic property of the aneurysm wall will be referred to as the "*realistic distribution*" of the elastic properties. Taking the realistic distribution as input, we simulate an inflation motion by performing a series of quasistatic finite element analyses for the aneurysm sac. The obtained deformed configurations and assumed reference configuration are considered as "*virtual*" experimentally observed configurations. Subsequently, we set the elastic properties (may include fiber orientation information) of the aneurysm to be unknown

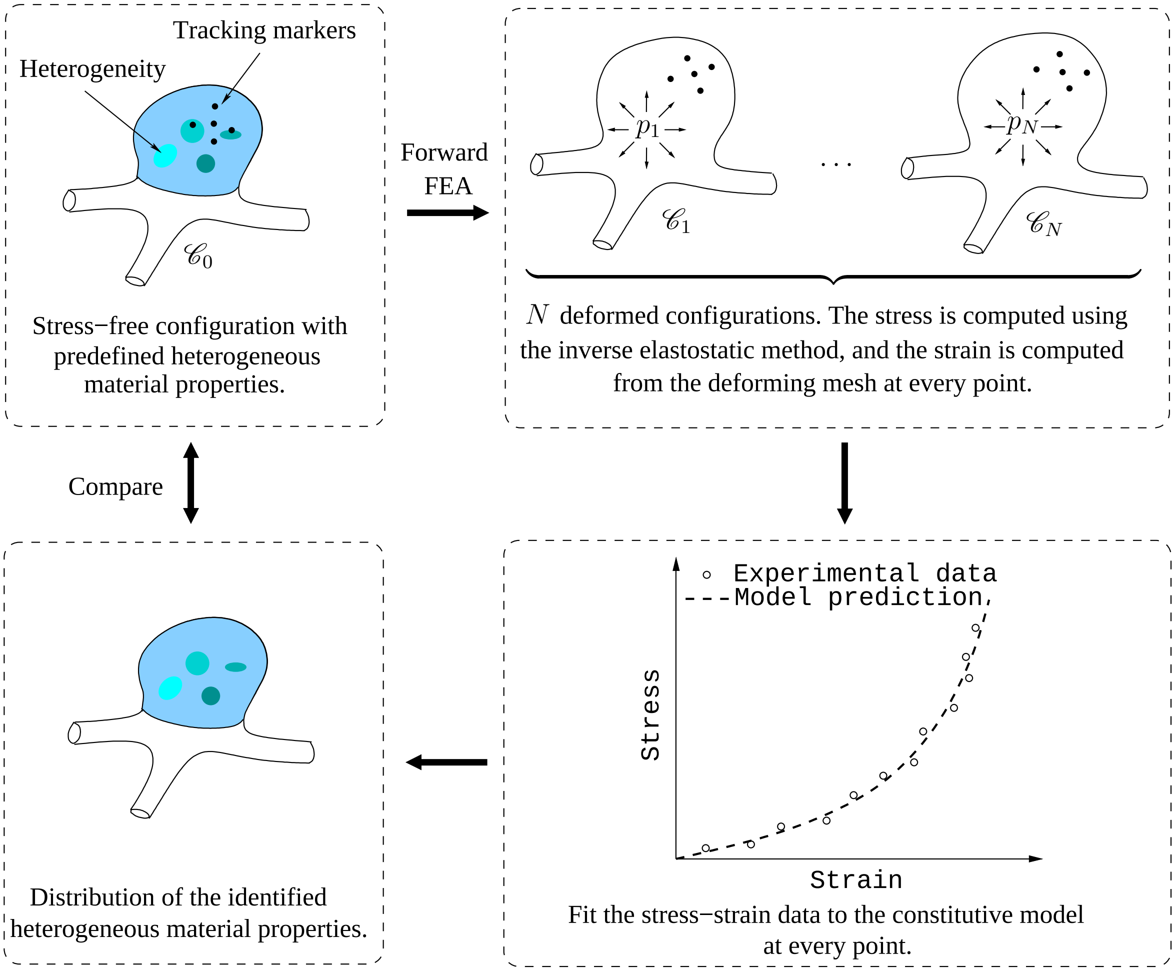

Figure 7.1: Schematic of the validation procedure.

and use the virtual experimental data to identify the elastic parameters of the selected model. After applying the pointwise identification method for each Gauss point, a distribution of identified elastic properties is obtained for the cerebral aneurysm sac. This distribution will be referred to as the "*identified distribution*" of the elastic properties. The next step is to compare the *identified distribution* to the *realistic distribution*. If the difference between these two distributions is small enough, we can conclude that the method is valid and effective.

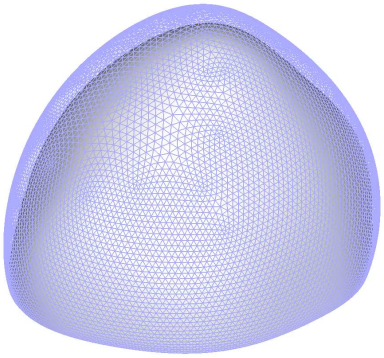

Figure 7.2: The initial configuration (shaded) a deformed configuration under a pressure of 110 mmHg (mesh) of the cerebral aneurysm sac.

7.2 Method

7.2.1 Material model

Cerebral aneurysm wall consists of primarily 7-8 layers of type I and III collagen fibers with varying orientations that form two-dimensional networks [13]. At the continuum level, the tissue is typically described by a single strain energy function that taking into account collectively the properties of the constituents and microstructure. Following [78], we assume that the cerebral aneurysm wall is composed of random elastin network, reinforced by two families of orthogonal collagen fibers. The first family of fibers are further assumed to be parallel to the basal $(x - y)$ plane and tangent to the aneurysm surface at every point. The second family is pointwise perpendicular to the first one. The material property of the cerebral aneurysm is assumed to be heterogeneous; the elastic stiffness decreases linearly with respect to the height from the neck (cf. Figure 7.3). The reference wall thickness is set to be uniform and takes the value of $H = 0.1$ mm.

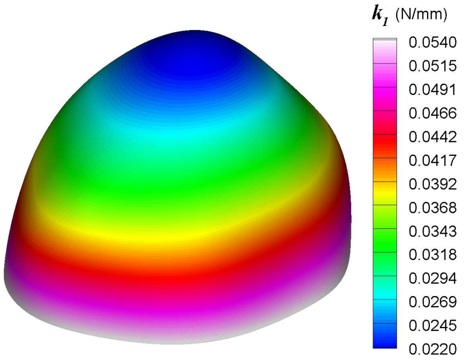

Figure 7.3: Realistic (assumed) distribution of the elastic parameter k_1.

We use an anisotropic structural strain energy function proposed by Holzapfel et al. [60] to model the anisotropic elastic behavior of the cerebral aneurysm sac. The strain energy function takes the form

$$w = k_1 \left(I_1 - 2\log J - 2\right) + \sum_{i=4,6} \frac{k_i}{a} \left\{\exp\left[a\left(I_i - 1\right)^2\right] - 1\right\}, \tag{7.1}$$

where k_i $(i = 1, 4, 6)$ are *effective* elastic stiffness parameters, which are the product of 3D elasticity constants and the wall thickness, having the dimension of force per unit length, and a is a dimensionless parameter. Here k_4 and k_6 characterize the stiffness in the fiber directions (or the preferred directions), i.e. the horizontal $\mathbf{N}_1$ and the meridional $\mathbf{N}_2$ directions. To the authors' knowledge, there is no established evidence on which direction exhibits stiffer behavior. In this study, we assume the collagen fibers along $\mathbf{N}_1$ are two times stiffer than those along $\mathbf{N}_2$.

In Equation (7.1), I_1, I_4, I_6, and $J = \sqrt{I_2}$ are the strain invariants, which are given by Equations (3.8) and (3.15). Due to the assumption that the two fiber directions in the reference configuration are orthogonal, I_4 and I_6 satisfy the relation $I_1 = I_4 + I_6$. The components of the membrane stress is derived as

$$\begin{aligned} t^{\alpha\beta} &= \frac{2}{J} k_1 \left(G^{\alpha\beta} - g^{\alpha\beta} \right) \\ &+ \frac{4}{J} k_4 \exp \left[a \left(I_4 - 1 \right)^2 \right] \left(I_4 - 1 \right) \left(N_1^{\delta} G_{\delta\gamma} N_1^{\gamma} \right)^{-1} N_1^{\alpha} N_1^{\beta} \\ &+ \frac{4}{J} k_6 \exp \left[a \left(I_6 - 1 \right)^2 \right] \left(I_6 - 1 \right) \left(N_2^{\delta} G_{\delta\gamma} N_2^{\gamma} \right)^{-1} N_2^{\alpha} N_2^{\beta} \end{aligned} \tag{7.2}$$

where $\alpha, \beta, \delta, \gamma = 1, 2$, and repeating index implies summation.

The linearly varying stiffness of the aneurysm wall material is represented by the varying effective elasticity parameter, k_i $(i = 1, 4, 6)$, according to

$$k_i = k_i^{fundus} + \frac{k_i^{neck} - k_i^{fundus}}{Z_i^{neck} - Z_i^{fundus}} (Z - Z_i^{fundus}) \tag{7.3}$$

where Z is the "Z" coordinate of any point on the sac, Z^{fundus} and Z^{neck} are the "Z" coordinates at the fundus and neck, respectively. Similarly, k_i are the elastic parameters at point "Z", k_i^{fundus} and k_i^{neck} are respectively the elasticity parameters at the fundus and neck, and they take the value of

$$\begin{aligned} k_1^{fundus} &= 0.01875 \text{ N/mm}, \quad k_1^{neck} = 0.05626 \text{ N/mm}, \\ k_4^{fundus} &= 0.03513 \text{ N/mm}, \quad k_4^{neck} = 0.10538 \text{ N/mm}, \\ k_6^{fundus} &= 0.01171 \text{ N/mm}, \quad k_6^{neck} = 0.03513 \text{ N/mm}. \end{aligned} \tag{7.4}$$

The value of the parameter $a = 0.7112$ is assumed to be identical across the whole sac.

Due to the scarcity of published values of the elastic parameters of model (7.1) specific to cerebral aneurysms, we refer to the identified parameters from experiments for arteries by Holzapfel et al. [60] while choosing the values of these parameters. The value of a is the same as the reported value for arterial adventitia. The stiffnesses in the two preferred directions are not differentiated in [60]. We scaled proportionally the reported values of k_1 and k_4 in [60], and presume the value of k_6 based on the assumption that the stiffness along $\mathbf{N}_1$ is two times higher than that along $\mathbf{N}_2$, i.e. $k_4 = 3k_6$. It is worth pointing out that these parameters are chosen to generate a reasonable deformation while taking advantage of the most reliable experimental results in the literature. In the deformation range considered in the current study, the stress-strain relation is insensitive to the parameter a (see the analysis in §7.2.5). Thus, it is difficult to identify a using the stress-strain data. As a first step, we assign the actual value of a and identify the elastic parameters k_1, k_4, k_6, and possibly the fiber orientations. Figure 7.3 shows the realistic (assumed) distribution of k_1. The realistic distribution of k_4 and k_6 has the same pattern and is not shown here.

7.2.2 Forward analysis

Eleven deformed configurations were generated by applying pressures ranging from 60 to 110 mmHg at an interval of 5 mmHg. To simulate the clamped boundary constraint typically used in experiments, we assumed that the neck of the sac is fixed. The simulation of the inflation motion was conducted using the forward nonlinear membrane finite element in FEAP, a nonlinear finite element program originally developed at the University of California, Berkeley [147]. The largest principal surface

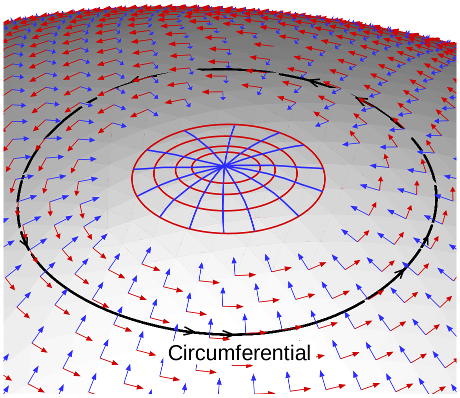

Figure 7.4: The distribution of fiber directions at the fundus.

stretch, $\lambda_1 = 1.12$, occurs on the configuration under the highest pressure (p=110 mmHg).

Because we assume the first family of collagen fibers lies parallel to the basal plane, the fibers near the fundus form closed loops with extremely small radius of curvature which presents great reinforcing effect (cf. Figure 7.4). It turns out that the deformed surface near the fundus is almost flat, which gives difficulties in determining the stress in there by inverse analysis. Therefore, the stress determination would be inaccurate not only at the region near the clamped boundary, but the region near the fundus. It is worth noting that such phenomena arises from our assumption on the fiber direction distribution. In reality, this assumption may not be completely valid for cerebral aneurysms, especially near the fundus. Therefore, the inaccurate stress determination near the fundus reported here will unlikely be present.

7.2.3 Computation of stress

Following the inflation simulation of the cerebral aneurysm sac, we took each of the obtained deformed configurations as input, and applied the inverse method to compute the wall stress distribution. Cauchy stress was obtained at each Gauss point of the finite element mesh. An isotropic neo-Hookean constitutive model along with arbitrarily chosen model parameters were used to compute the wall stress. The neo-Hookean strain energy function takes the form

$$w = \frac{\nu_1}{2}\left(I_1 - 2\log J - 2\right) + \frac{\nu_2}{4}\left(I_1 - 2\right)^2 . \tag{7.5}$$

Similar to the elastic parameters k_i of the Holzapfel model, the parameters ν_1 and ν_2 here are also effective elastic parameters which are multiplications of 3D elasticity constants with the wall thickness. $\nu_1 = \nu_2 = 5.0$ N/mm were used in the inverse FE analysis. The computed stress distributions were compared to the actual stress distribution computed from the forward FE analyses to evaluate the insensitivity of the stress with respect to the selected constitutive models and their elastic parameters.

7.2.4 Computation of strain

In theory, if the stress-free configuration is known, from the nodal coordinates in the reference and deformed configurations, strain distributions in each deformed configuration can be computed with the aid of the finite element interpolation. However, in the current covariant setting, the base vectors ($\mathbf{G}_\alpha$ and $\mathbf{g}_\alpha$) of the stress-free configuration and deformed configurations are computed first, from which the corresponding metric tensors ($G_{\alpha\beta}$ and $g_{\alpha\beta}$) are computed accordingly. If the fiber directions $\mathbf{N}_1$ and $\mathbf{N}_2$ are also known, these metric tensors in the stress-free and deformed configurations will be input directly to the stress function to compute the modeled stress, which will be compared to the experimental stress data in the parameter regression process.

If the stress-free configuration is assumed to be unknown to mimic the in vivo setting, we need to identify the elastic parameters together with the unknown metric tensor components. In this case, linear transformation of the metric tensors in the deformed configurations must be conducted. Here, at each Gauss point, we first transform the metric tensor in the deformed configuration under the lowest pressure to an identity tensor, and apply the same transformation rule to the metric tensors of the remaining deformed configurations. Under such transformations, the base vectors of these metric tensors remain convected. The basic formulation was presented in §3.5.

7.2.5 Elastic parameters identification

As shown in Equation (7.2), the stress components are functions of the reference and current metric tensors, the fiber directions, and the elastic parameters appearing in the constitutive law. As described above, at each Gauss point we can obtain the stress components $t^{\alpha\beta}$ and the convected components $g_{\alpha\beta}$ of the current metric tensor in each of deformed configurations. If the stress-free configuration is known, the reference metric tensor components $G_{\alpha\beta}$ are also known. Accordingly, the strain invariants I_1, I_2, I_4, and I_6 can be computed by Equations (3.8) and (3.15).

We denote the modeled stress in the i-th configuration by

$$^{(i)}t^{\alpha\beta} = t^{\alpha\beta}(a, k_1, k_4, k_6, {}^{(i)}g_{\delta\gamma}, G_{\delta\gamma}, N_1^\delta, N_2^\delta) \tag{7.6}$$

Let $^{(i)}\hat{t}^{\alpha\beta}$ be the "experimental" stress components obtained from the inverse analysis. The objective function is defined pointwise, as

$$\Phi = \sum_{i=1}^{N} \left({}^{(i)}t^{\alpha\beta} - {}^{(i)}\hat{t}^{\alpha\beta}\right) {}^{(i)}g_{\alpha\gamma}\, {}^{(i)}g_{\beta\delta} \left({}^{(i)}t^{\delta\gamma} - {}^{(i)}\hat{t}^{\delta\gamma}\right) \tag{7.7}$$

where, N is the total number of deformed states. In tensor notation, $\Phi = \sum_{i=1}^{N} \| {}^{(i)}\mathbf{t} - {}^{(i)}\hat{\mathbf{t}} \|^2$. If the global stress-free configuration is known, Φ is a function of the elastic parameters only.

Alternatively, as long as the modeled and experimental stress are described in the same convected coordinate system, one may construct the cost function as

$$\Psi = \sum_{i=1}^{N} w_1 \left({}^{(i)}t^{11} - {}^{(i)}\hat{t}^{11}\right) + w_2 \left({}^{(i)}t^{22} - {}^{(i)}\hat{t}^{22}\right) + w_3 \left({}^{(i)}t^{12} - {}^{(i)}\hat{t}^{12}\right) \tag{7.8}$$

where w_i $(i = 1, ..., 3)$ are weight parameters. One can judiciously choose different weight parameters by observing different ratios among the stress components. In the current study, the two cost functions were both used, but not at the same time. More details will be discussed in §7.3.

As mentioned briefly in §7.2.1, the stress is insensitive to the elastic parameter a at $a = 0.7112$. To see this, we expand the exponential terms in the Holzapfel's strain energy function into a Taylor series to give

$$w = k_1\left(I_1 - 2\log J - 2\right) + \sum_{i=4,6} k_i \left[\left(I_i - 1\right)^2 + \frac{a}{2}\left(I_i - 1\right)^4 + ...\right]. \tag{7.9}$$

At a point where the maximum deformation occurs ($\lambda_1 = 1.12$), the quadratic term $\left(I_i - 1\right)^2 = 5.93 \times 10^{-2}$, whereas the quartic term $\frac{a}{2}\left(I_i - 1\right)^4 = 7.03 \times 10^{-4}$ which is about two orders of magnitude smaller than the leading term. Therefore, the strain energy and stress are very insensitive to the perturbation of a, which makes it difficult to identify a, especially when experimental error exists. Based on this fact, we take "a" as a known parameter and exclude it from regression.

First, we focus on an in vitro setting in which a slightly inflated configuration is taken as a reference configuration and thus $G_{\alpha\beta}$ are known. The situation of the stress-free configuration being unknown will be taken into account later. If the fiber directions are also known, the regression problem can be described as

$$\begin{aligned} &\text{minimize} && \Phi\left(k_1, k_4, k_6\right) \quad \text{or} \quad \Psi\left(k_1, k_4, k_6\right) \\ &\text{subject to} && \mathbf{l} \leq \left[k_1, k_4, k_6\right]^T \leq \mathbf{u}. \end{aligned} \tag{7.10}$$

Here, $\mathbf{l}$ and $\mathbf{u}$ are the lower and upper bounds of the vector of regression variables $\left[k_1, k_4, k_6\right]^T$.

If the fiber directions are not known, one more regression variable enters the identification process. In the current set-up, $N_1^1 = \mathbf{N}_1 \cdot \mathbf{G}^1$ and $N_1^2 = \mathbf{N}_1 \cdot \mathbf{G}^2$ are the components of the first fiber direction $\mathbf{N}_1$ with respect to base vectors $\mathbf{G}_1$

and $\mathbf{G}_2$, respectively. Since two fiber directions are orthogonal in the stress-free configuration, the components (N_2^1 and N_2^2) for the second fiber direction $\mathbf{N}_2$ are determined explicitly. Therefore, the identification of the fiber directions can be realized by identifying only one fiber direction, say $\mathbf{N}_1$.

From Equation $(3.15)_a$, we know that I_4 depends only on the ratio between N_1^1 and N_1^2, and thus so for I_6. In the parameter regression process, we first set N_1^1 to be 1, and identify N_1^2. If the realistic value of N_1^1 is comparable to 1, N_1^2 can be identified successfully. However, If the realistic value of N_1^1 is close to 0 and that of N_1^2 is close to ± 1, the ratio $|N_1^2/N_1^1| \gg 1$. If this happens, we set N_1^2 to be 1 and identify N_1^1.

If the stress-free configuration is not available which is true for thin membrane structures and biological tissues in the living body, as we did for isotropic material in Chapter 5, we are going to define an imaginary or virtual local stress-free configuration at a material point and parameterize it using a Rimannian metric tensor which is symmetric. The three independent components of the metric tensor will be treated as three model parameters when using the constitutive equation, and they are identified together with the elastic parameters in the parameter regression process. In order to have a broader deformation range, we added four more deformed configurations. The current number of deformed configurations is 15, and the pressure is ranging from 50 to 120 mmHg at an interval of 5 mmHg. Another assumption we made is that the two families of collagen fibers are orthogonal in the stress-free configuration although the stress-free configuration itself is unknown. There are totally six parameters which will be identified, i.e., the three elastic parameters, k_1, k_4 and k_6, and the three unknown metric tensor components, $\mathfrak{G}_{11}$, $\mathfrak{G}_{22}$ and $\mathfrak{G}_{12}$, of the local stress-free configuration at each Gauss point. Hence, the parameter identification problem becomes a regression process as

$$\begin{aligned} &\text{minimize} && \Phi\left(k_1, k_4, k_6, \mathfrak{G}_{11}, \mathfrak{G}_{22}, \mathfrak{G}_{12}\right) \\ &\text{subject to} && \mathfrak{G}_{11} > 0, \quad \mathfrak{G}_{22} > 0, \quad \mathfrak{G}_{11}\mathfrak{G}_{22} - \mathfrak{G}_{12}^2 > 0, \\ &\text{and} && \mathbf{l} \leq \left(k_1, k_4, k_6, \mathfrak{G}_{11}, \mathfrak{G}_{22}, \mathfrak{G}_{12}\right) \leq \mathbf{u}. \end{aligned} \tag{7.11}$$

where $\mathbf{l}$ and $\mathbf{u}$ are the lower and upper bounds of the regression variables k_i and $\mathfrak{G}_{\alpha\beta}$.

The parameter identification was performed by a gradient-based, sequential quadratic programming (SQP) algorithm, SNOPT [43].

7.3 Results

7.3.1 Wall stress is insensitive to the material property

Before identifying the elastic parameters, we need to verify that the wall stress obtained from inverse analysis is truly insensitive to the material property. The principal stresses in a deformed configuration ($p = 110$ mmHg) computed from *forward* FEA with the anisotropic Holzapfel model are denoted as t_i^{for}, $(i = 1, 2)$. The principal stresses in the same deformed configuration computed from *inverse* FEA with the isotropic neo-Hookean model are denoted as t_i^{inv}, which are shown in Figure 7.5. We use a quantity $e_i = \left|\frac{t_i^{inv} - t_i^{for}}{t_i^{for}}\right| \times 100\%, (i = 1, 2)$ to evaluate the percentage difference between t_i^{inv} and t_i^{for}. Figure 7.6 shows the distribution of e_i. As can be seen from the figures, in the most part of the sac (excluding the near-boundary region, the fundus

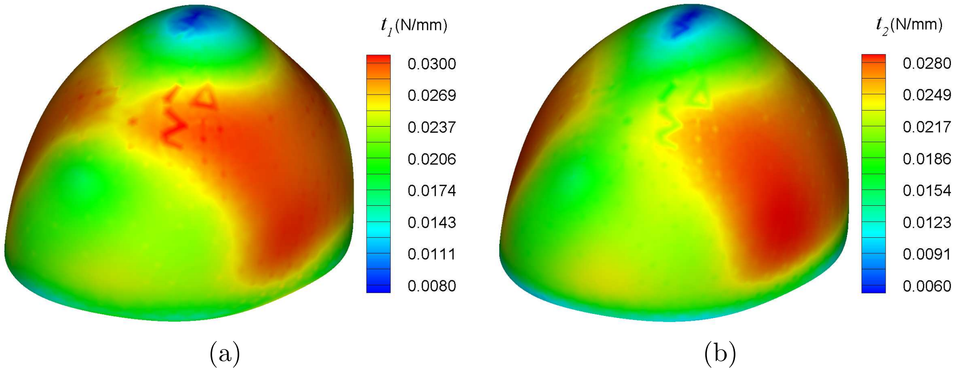

(a) (b)

Figure 7.5: Distribution of the principal stresses on the deformed configuration under the highest pressure (110 mmHg): (a) t_1, (b) t_2.

region, and a narrow stripe along the meridional direction (displayed in light blue)), e_1 and e_2 are less than 1%. Within the stripe, they are in the order of 2%. We will see later that in this region the strain is also relatively small ($\lambda_1 \approx 1.07$), and this region turns out to be where the parameter identification is relatively inaccurate. The distribution of the first principal stretch is shown in Figure 7.7. The distribution of e_i induced by increasing ν_1 and ν_2 more shows no significant change. The fact that stress is insensitive to the material property has been revealed again. This fact is especially valuable in that it allows one to arbitrarily choose a constitutive model and use it to compute membrane stress before suitable constitutive models can be determined. Therefore, the obtained wall stress data can be used to represent the realistic stress data for the purpose of elastic parameter identification.

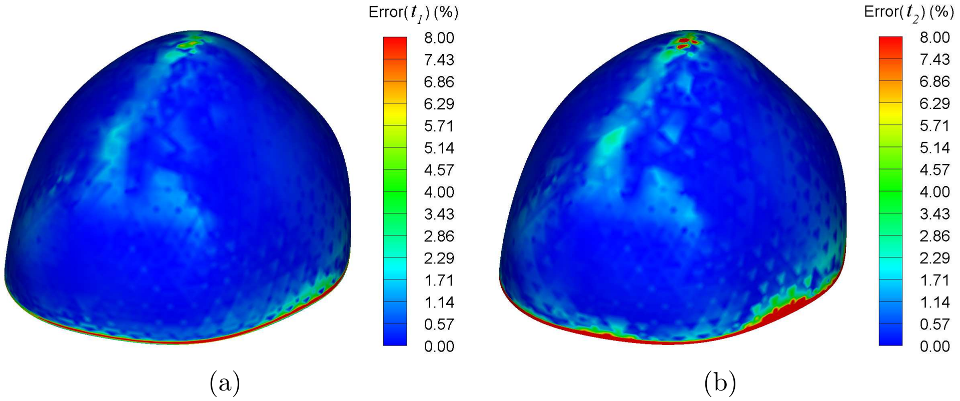

(a) (b)

Figure 7.6: The absolute percentage difference between the principal stresses computed from inverse and forward FEA: (a) Error(t_1), (b) Error(t_2).

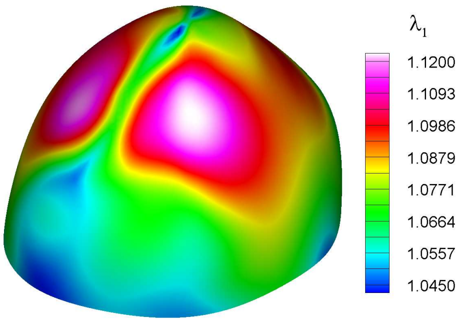

Figure 7.7: Distribution of the first principal stretch.

7.3.2 Distribution of the identified elastic parameters

7.3.2.1 Pointwise identification when the fiber orientation is known

Parameter identification was conducted for all the Gauss points in the whole sac using the cost function Φ (cf. Equation (7.7)). We compared the identified parameters to the exact parameters and extracted the elements where the identification error of k_4 exceeded 3%. Subsequently, we repeated the parameter identification using the cost function Ψ (cf. Equation (7.8)) for the Gauss points in the selected elements. The weights w_i were chosen according to the ratios among the experimental stress components, i.e. $|\hat{t}^{11}/\hat{t}^{22}|$ and $|\hat{t}^{11}/\hat{t}^{12}|$, so as to fairly consider the influence of all the stress component on the objective function value by scaling them to a similar order. The results showed improvement in most points. After identification, we projected the parameters at Gauss points to the nodes using a least-square algorithm for a more convenient demonstration using Tecplot 360 (Tecplot, Inc.).

Figure 7.8 shows the distribution of the identified parameters k_i. Qualitatively judged from the figure, the linear dependence of the identified k_i on the height was recovered. The identification errors between the identified parameters and the realistic ones were computed at each nodal point according to $Error(k_i) = \left|\left(k_i - \tilde{k}_i\right)/\tilde{k}_i\right| \times 100\%, (i = 1, 4, 6)$, where k_i and $\tilde{k}_i$ are identified and realistic elastic parameters, respectively. Figure 7.9 shows the distribution of the identification error $Error(k_i)$. The identification error is less than 8%, 3% and 5% for k_1, k_4 and k_6, respectively, in the bulk region of the aneurysm sac. Consistently with the regions where the stress computation is not accurate, the identification is less accurate at the boundary area

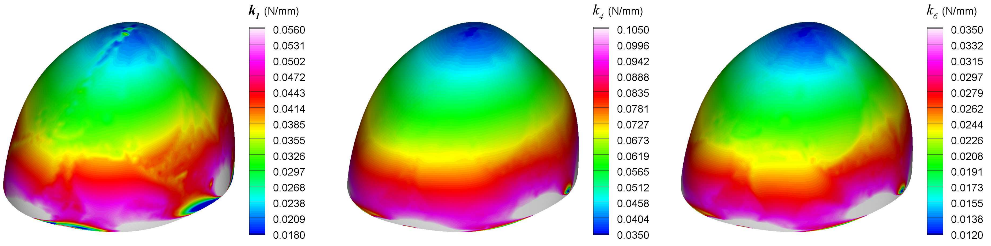

(a) (b) (c)

Figure 7.8: Distribution of the identified elastic parameters from pointwise identification by assuming the fiber directions are known: (a) k_1, (b) k_4, (c) k_6.

Table 7.1: Means, minimums and maximums of the identification errors of the *pointwise* identification by assuming the fiber orientation is *known.*

	Error(k_1)	Error(k_4)	Error(k_6)
Mean (%)	6.41	3.50	4.08
Min (%)	1.45×10^{-4}	8.66×10^{-5}	7.17×10^{-4}
Max (%)	124.1	78.81	78.81

and the fundus. In addition, the identification is less accurate in the region where the stretch is relatively low ($\lambda_1 < 1.08$), i.e., the neck region and the meridional stripe illustrated in the contour plot of the first principal stretch (Figure 7.7). Figure 7.9 shows the distribution of the identification error of k_i, $Error(k_i)$. Generally, relatively bigger error occurs where the deformation is relatively smaller. The means, minimums and maximums of the identification errors over the whole sac are listed in Table 7.1. The maximum error occurs near the boundary, and large error only occurs at scattered spots. The mean errors for the three parameters are 6.41%, 3.50% and 4.08%, respectively.

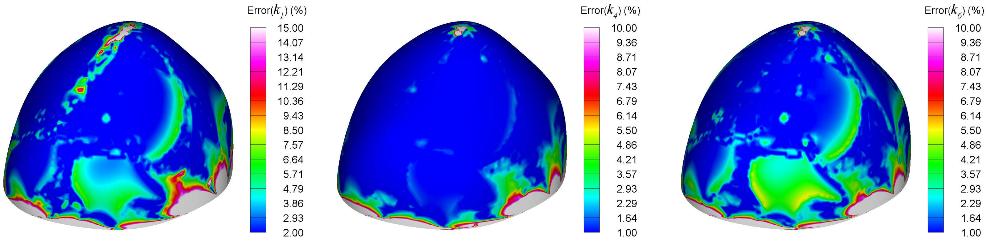

(a) (b) (c)

Figure 7.9: Distribution of the identification errors of the elastic parameters from pointwise identification by assuming the fiber directions are known: (a) Error(k_1), (b) Error(k_4), (c) Error (k_6).

7.3.2.2 Pointwise identification when the fiber orientation is unknown

When assuming the fiber orientation is unknown except that the material is orthotropic, the elastic parameters k_i were identified along with N_1^1 (or N_1^2) by using the objective function Φ. Figure 7.10 shows the distribution of the identified parameters k_i. From a qualitative point of view, the regional variation of the elastic parameters was successfully identified. Quantitatively, the absolute identification errors for k_1, k_4 and k_6 were respectively less than 5%, 2% and 2% in the bulk region of the aneurysm sac. The means, minimums and maximums of the identification errors over the whole sac are listed in Table 7.2. The mean errors for the three parameters are 10.35%, 4.15% and 4.15%, respectively. Compare to the case of known fiber directions, the mean errors for all the parameters are larger although the elevation is not significant. This is understandable since there is one more parameter in the regression.

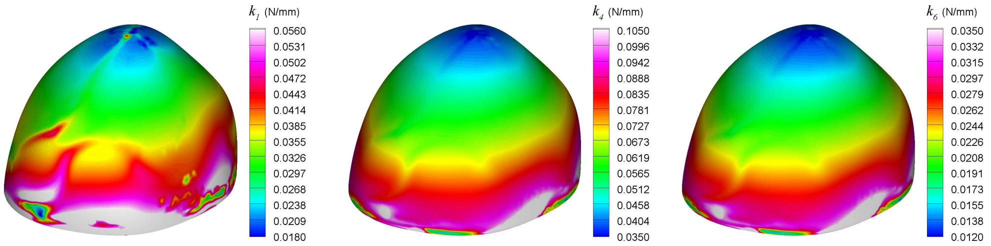

(a) (b) (c)

Figure 7.10: Distribution of identified elastic parameters from pointwise identification by assuming the fiber directions are unknown: (a) k_1, (b) k_4, (c) k_6.

Table 7.2: Means, minimums and maximums of the identification errors of the *pointwise* identification by assuming the fiber orientation is *unknown*.

	Error(k_1)	Error(k_4)	Error(k_6)
Mean (%)	10.35	4.15	4.15
Min (%)	2.08×10^{-3}	5.20×10^{-5}	7.79×10^{-5}
Max (%)	122.9	63.04	63.04

7.3.2.3 Region-wise identification when the fiber orientation is known

The proposed *pointwise* method can be modified to render a *region-wise* identification. By region-wise, we mean assuming the material property is homogeneous within a region of specific size, and let the cost function include the stress-strain data at all the Gauss points in that region. The logic is keen to that of the subdomain inverse finite element method although the implementation is entirely different. Figure 7.11 shows the distribution of the identified elastic parameters by region-wise identification. The small region was chosen to be each element. The identification was conducted by using the cost function Φ alone, but including all the Gauss points

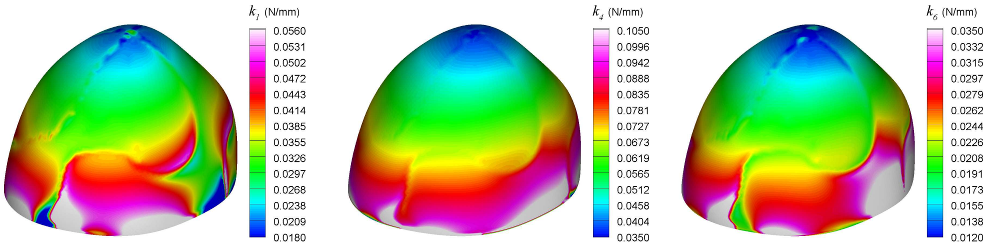

(a) (b) (c)

Figure 7.11: Distribution of identified elastic parameters from "region-wise" identification by assuming the fiber directions are known: (a) k_1, (b) k_4, (c) k_6.

Table 7.3: Means, minimums and maximums of the identification errors of the *region-wise* identification by assuming the fiber orientation is *known*.

	Error(k_1)	Error(k_4)	Error(k_6)
Mean (%)	10.83	4.52	8.31
Min (%)	2.39×10^{-4}	1.51×10^{-5}	1.11×10^{-3}
Max (%)	100.0	81.05	90.49

within each element. The identification accuracy is almost identical to that of the *pointwise* scheme when using the single objective function Φ because the element size is very small. The identification error is quite small in most part of the sac. The identification error of k_1, k_4 and k_6 is below 4.0%, 2.5% and 4.0%, respectively, in most part of the sac. As the results show, the element-wise identification still can characterize the material heterogeneity relatively accurately as long as the specified homogeneous regions are small enough. The maximums, minimums, and means of the identification errors over the whole sac are listed in Table 7.3. The mean errors for the three parameters are 10.83%, 4.52% and 8.31%, respectively.

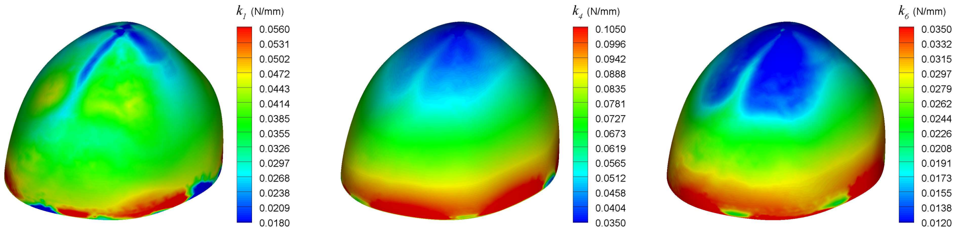

(a) (b) (c)

Figure 7.12: Distribution of the identified elastic parameters by assuming the stress-free configuration is unknown: (a) k_1, (b) k_4, (c) k_6.

7.3.2.4 Pointwise identification assuming the stress-free configuration is unknown

Figure 7.12 shows the distribution of the identified parameters k_i. Qualitatively judged from the figure, the dependence of the identified parameters on the height from the aneurysm neck was recovered, except for the region where the stress determination was not accurate enough, i.e., near the clamped boundary and at the fundus. Figure 7.13 shows the identification error $Error(k_i)$. The identification error is less than 15%, 5% and 9% for k_1, k_4 and k_6, respectively, in the bulk region of the aneurysm sac which is in blue in Figure 7.13. Due to the addition of three more parameters into the regression process, the identification error turns out to be larger which is understandable. However, the identification error is still acceptable.

7.4 Discussion

In this chapter, we showed through numerical experiments that the pointwise identification method is also applicable to anisotropic material. We demonstrated the

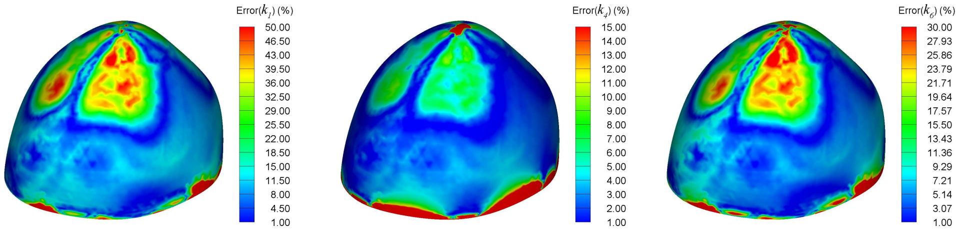

(a) (b) (c)

Figure 7.13: Distribution of the identified error by assuming the stress-free configuration is unknown: (a) Error(k_1), (b) Error(k_4), (c) Error(k_6).

feasibility of identifying the local fiber directions from stress-strain data. In theory, characterizing material anisotropy involves two tasks: (1) Identifying the symmetry group (e.g., isotropy, transversely isotropy, orthotropy, etc.), and (2) Identifying the structural information (e.g., the fiber directions) associated with the material anisotropy. The former dictates the mathematical representation of permissible function forms that contain the desired material symmetry. While the simulation suggested a possible approach for identifying the latter under the assumption of known symmetry group (which is implied in the assumed constitutive equation), it remains unclear as to whether in real applications the symmetry group can be determined from stress-strain data alone. For certain classes of materials, the elastic stress and deformation should obey certain universal relations involving no material property information. By examining if corresponding universal relations hold true, one may determine the type of material symmetry. The universal relations for isotropic materials were treated in [54, 172, 9, 10, 108, 113], and those for transversely isotropic materials were investigated in [108, 113, 8, 120, 119].

In Chapter 6, we used a universal relation ($\mathbf{CS} = \mathbf{SC}$) for isotropic materials to determine if the tested rubber is isotropic so as to choose appropriate constitutive models. It is understood that any class of hyperelastic materials possessing anisotropic properties more complicated than those of transversely isotropy obeys no universal relations [133]. However, Soldatos [133] showed that certain types of orthotropic hyperelastic materials still obey certain universal relations. For these orthotropic materials, universal relations can be used for symmetry characterization. For other types of anisotropic materials, whether universal relations exist remains unknown. Under such circumstances, a possible solution is to utilize appropriate techniques to determine fiber orientation, e.g. Polarized Light Microscopy [93], small angle light scattering [51] and depth-resolved SHG polarimetry [177], and construct structural models that incorporate the experimentally determined fiber information.

Low strain can have an adverse effect on parameter identification. As the results showed, the elastic parameter identification was more accurate in the high-strain region ($\lambda_1 \geq 1.08$) than in the low-strain region ($\lambda_1 < 1.08$). The strain range used in this study (10%) has already exceeded the physiological strain typical of cerebral aneurysms (2–5%). The influence of strain range is not unexpected. The reason is that the realistic parameters in the constitutive model are supposed to model the elastic behavior of the material in any deformation range. However, due to the inevitable experimental error in determining the membrane surface geometry and the position of tracking markers and the induced error in determining the realistic stress and strain distribution, certain values of the elastic parameters may render a local minimum of the objective function at a small-strain point, which may not predict the elastic response in high-strain range at that point. This fact highlights the limitation that the elastic behavior is not fully represented at the points where the deformation is relatively small. Nevertheless, it is worth-noting that the elastic properties identified as such may still fulfill a good predictive model for physiological motions since they are characterized from the realistic deformation undergone in service. Moreover, the conclusion about the feasibility of the method should remain valid if the strain values used in the study are uniformly lowered.

To a lesser degree of importance, the simulation embodied a number of assumptions that may not be realistic. First, we assume that the horizontal fibers are stiffer than the meridional fibers. So far, there is yet no reliable evidence on how the collagen fibers orient and which direction is stiffer than the other as the aneurysms initiate and develop. Existing studies presented conflicting arguments. Without bias toward either of the existing hypotheses, we assume in the current study that the fiber in the circumferential direction is stiffer, just for demonstrative purpose. Later application of the proposed method to physical experiments on realistic cerebral aneurysms may be able to shed some light on the further verification of these hypotheses. It should be noted that the assumptions on fiber direction and stiffness difference have no effect on the demonstrated capability. Secondly, the identified stiffness parameters k_1, k_4 and k_6 in the model are effective parameters which are the products of the intrinsic 3-D elasticity parameters and the wall thickness. If the intrinsic 3-D elasticity parameters need to be determined, one must obtain the wall thickness. In summary, although this study is limited to numerical experiment, it clearly highlighted the features of PWIM and demonstrated its feasibility of identifying the distribution of anisotropic heterogeneous elastic properties in cerebral aneurysm wall.

CHAPTER 8
EXPERIMENTS: RABBIT URINARY BLADDER

8.1 Introduction

The urinary bladder is a distensible sac-like organ that collects urine excreted by the kidneys prior to disposal by urination. When urine inside the bladder reaches a certain level, the fluid pressure stimulates nervous signals that relax the external sphincter to allow for the urinary flow. The ability of the bladder to accommodate increasing amounts of urine while maintaining a low intravesical pressure is related to the resilience or elasticity of the bladder and is functionally defined as compliance [18].

Type I collagen is the most common structural protein found in the body and is the most abundant collagen in the bladder. Type III collagen, which often colocalizes with type I [36], is also widely distributed throughout the bladder wall [18]. Healthy and normal bladder wall is very compliant. Under some pathological conditions, e.g., spinal cord injury [44], the compliance of the bladder wall will decrease, which affects its deforming ability significantly. The decrease in compliance is believed to be caused by thickening of the bladder wall due to smooth muscle cell hypertrophy and increased connective tissue deposition [18]. Knowledge of the elastic property is of critical importance in understanding the bladder function and in reconstruction surgical planning.

The mechanical property characterization of urinary bladders has focused on quasi-static uniaxial tests [26, 168, 5, 4], biaxial tests [44], in situ studies [4, 117, 24, 82] and uniaxial viscoelasticity studies [23, 163, 27]. In order to provide accurate description of the mechanical properties of urinary bladders, whole organ characterization is highly demanded, which is rare for the time being.

8.2 Method

8.2.1 Materials and experiment

We conducted an organ-level in vitro inflation experiment on a rabbit urinary bladder. 81 (9 by 9) points were drawn on the bladder surface using tissue marking dye (Cancer Diagnostics, Inc.). These points will act as landmarks at which the displacements will be recorded during the inflation. The bladder was inflated by a nitrogen gas tank to nine pressure levels, the one of which under the lowest pressure (slightly inflated) was chosen as the approximately stress-free configuration. The markers also served as the nodes of a finite element mesh composed of 64 (8 by 8) quadrilateral elements. The spatial position of the tracking markers in each deformed states was recorded by using the optical motion capture system that was described in Chapter 6. Subsequently, the stress distribution in each deformed configuration was determined through finite element inverse elastostatics methods by using a neo-Hookean model (cf. Equantion (7.5)). The model parameters were set to be ν_1=ν_2=5 N/mm. The base vectors of the stress-free and deformed configurations were then computed according to Equation (4.2), from which the reference and current metric tensors could be computed accordingly. One of the deformed configurations of the inflated bladder is shown in Figure 8.1.

8.2.2 Material model

We assumed that the urinary bladder wall is composed of a random elastin network, reinforced by two families of orthogonal collagen fibers. Microscopically, we assumed the two families of collagen fibers are aligned with the longitudinal and circumferential directions of the bladder, respectively, in the undeformed states. An anisotropic structural strain energy function (cf. Equation (7.1)) proposed by Holzapfel et al. [60] was used to model the elastic behavior of the urinary bladder wall.

8.3 Results

First, we identified the elastic parameters k_1, k_4, k_6 and a at all the Gauss points in the whole domain and, we found that, at most points, the parameter k_1 characterizing the isotropic behavior was identified to be zero. Thus, we set k_1 to be zero for the whole domain. We also assumed that the value of a is identical over the whole urinary bladder and chose the identified value of a (a=44.98) at a point (in the central region of the mesh) where the stress-strain curve is quite smooth. We then identified parameters k_4 and k_6 in the central region where the stress solution from inverse elastostatic method is insensitive to the material property, i.e., the four elements in the middle of the mesh. Figure 8.2 shows the distribution of the identified parameters k_4 and k_6 in the whole reconstructed mesh. Due to the prescribed boundary condition on the four edges, the computed stress from inverse elastostatic method is relatively inaccurate, in the two layers of elements from the boundary, compared to the actual stress. Therefore, larger errors generally are induced for the identified

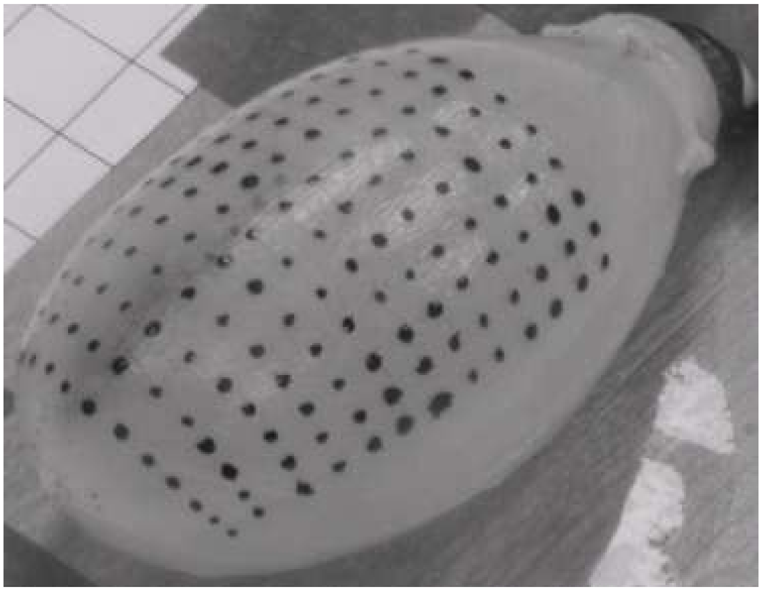

Figure 8.1: A photo of the inflated rabbit urinary bladder used in the process of 3-D geometry reconstruction.

elastic parameters. We show the identification results in the whole mesh for just a demonstrative purpose. Practically, the boundary effect can be reduced by providing finer mesh or refining the elements near the boundary, say the out-most two layers of elements. Comparison between the model prediction from the identified parameters and the experimental data at a point in the middle of the mesh is illustrated in Figure 8.3. As the figure shows, the Holzapfel model fits well the experimental data.

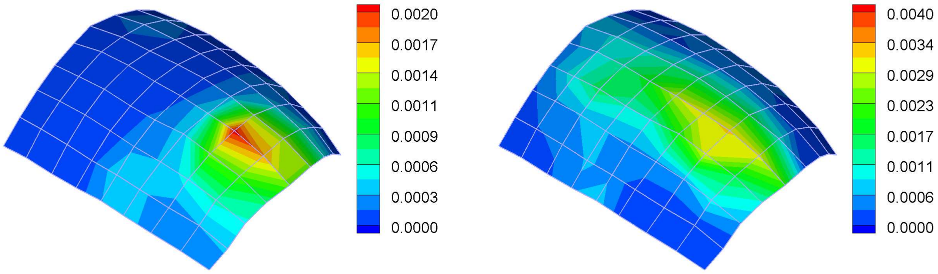

(a) (b)

Figure 8.2: Distribution of the identified elastic parameters of the rabbit urinary bladder: (a) k_4, (b) k_6.

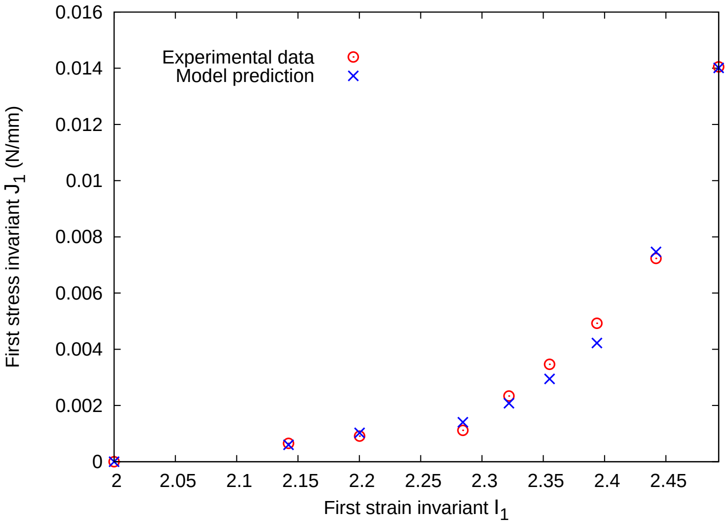

Figure 8.3: Comparison between the experimental and modeled stress invariants-strain invariants curves.

CHAPTER 9
MATERIAL SENSITIVITY ANALYSIS

Structural design sensitivity is a measure of the change in structural responses (displacements, stress, etc.) induced by the change in the system design variables or parameters (e.g., material properties, geometrical parameters, etc.). The sensitivity of a structural system to variations of its parameters is one of the most important aspects necessary for a proper understanding of system performance [75]. It has been very useful in reliability analysis and design optimization. In this chapter, we will use it as a tool to study how the variation of material property affect the wall stress in membranes.

Parameter sensitivity information can be computed with various methods of which two most important ones are *finite difference method* (FDM) and *direct differential method* (DDM). In FDM, the parameter sensitivity is approximated using *forward finite difference* or *central finite difference method* by perturbing particular parameter (e.g. material or constitutive parameter) and computing the perturbation of the performance measures (e.g. displacement and stress). In DDM, the parameter sensitivity is computed by differentiating the continuum or discretized state equation directly. Readers are referred to references [75, 19, 20] for more information about parameter sensitivity analysis. In the following, continuum DDM is introduced.

9.1 Mathematical formulation

For a general forward or direct boundary value problem, we start from the standard weak form

$$\int_{\Omega_0} \frac{1}{2}\mathbf{S} \cdot \delta\mathbf{C} dV = \int_{\Omega_0} \rho_0 \mathbf{b} \cdot \delta\mathbf{u} dV + \int_{\Gamma} \mathbf{t} \cdot \delta\mathbf{u} d\Gamma \tag{9.1}$$

where, $\mathbf{S}$ is the second Piola-Kirchhoff stress tensor, and $\mathbf{C}$ is the right Cauchy-Green deformation tensor, $\mathbf{b}$ is the body force, $\mathbf{t}$ is the boundary traction, Ω_0 is the reference domain, and Γ is the traction boundary.

Differentiating both sides of Equation (9.1) with respect to the design variable θ (say material parameters), we obtain

$$\int_{\Omega_0} \left\{ \underbrace{\frac{1}{2}\delta\mathbf{C} \cdot \left[\frac{\partial \mathbf{S}}{\partial \mathbf{C}} \cdot \mathbf{C},_\theta \right]}_{(1)} + \underbrace{\frac{1}{2}\mathbf{S} \cdot \left(\delta\mathbf{F}^T \mathbf{F},_\theta + \mathbf{F},_\theta^T \delta\mathbf{F} \right)}_{(2)} + \underbrace{\frac{1}{2}\mathbf{S},_\theta \cdot \delta\mathbf{C}}_{(3)} \right\} dV = 0 \tag{9.2}$$

since

$$\frac{\partial \delta\mathbf{C}}{\partial \theta} = \frac{\partial \delta \left(\mathbf{F}^T \mathbf{F} \right)}{\partial \theta} = \frac{\partial \left(\delta\mathbf{F}^T \mathbf{F} + \mathbf{F}^T \delta\mathbf{F} \right)}{\partial \theta} = \delta\mathbf{F}^T \mathbf{F},_\theta + \mathbf{F},_\theta^T \delta\mathbf{F} \tag{9.3}$$

where $(\cdot),_\theta$ denotes the partial derivative of the quantity $(\cdot)$ with respect to θ.

Recall that

$$\delta\mathbf{F} = \left(\bigtriangledown \delta\mathbf{u} \right) \mathbf{F}, \tag{9.4}$$

and denote

$$\bigtriangledown^{(s)}\,\delta\mathbf{u} = \frac{1}{2}\left(\bigtriangledown\delta\mathbf{u} + \left(\bigtriangledown\delta\mathbf{u}\right)^T\right), \tag{9.5}$$

where $\bigtriangledown^{(s)}\delta\mathbf{u}$ is the symmetric part of $\delta\mathbf{u}$. It follows from Equations (9.4) and (9.5) that term (1) in Equation (9.2) may be rewritten as

$$\begin{aligned}
\frac{1}{2}\delta\mathbf{C}\cdot\left[\frac{\partial\mathbf{S}}{\partial\mathbf{C}}\cdot\mathbf{C},_\theta\right] &= \frac{1}{2}\mathbf{F}^T\left(2\bigtriangledown^{(S)}\,\delta\mathbf{u}\right)\mathbf{F}\cdot\frac{1}{2}\mathbb{D}\cdot\mathbf{F}^T\left(2\bigtriangledown^{(S)}\,\mathbf{u},_\theta\right)\mathbf{F}\\
&= \bigtriangledown^{(S)}\delta\mathbf{u}\cdot\mathbf{F}\mathbf{F}\mathbb{D}\mathbf{F}^T\mathbf{F}^T\,\bigtriangledown^{(S)}\,\mathbf{u},_\theta\\
&= \bigtriangledown^{(S)}\delta\mathbf{u}\cdot J\mathbb{C}\,\bigtriangledown^{(S)}\,\mathbf{u},_\theta\,.
\end{aligned} \tag{9.6}$$

Here J is the volume change ratio, $\mathbb{D}$ is the material tangent tensor

$$\mathbb{D} = \frac{\partial\mathbf{S}}{\partial\mathbf{E}} = 2\frac{\partial\mathbf{S}}{\partial\mathbf{C}} \tag{9.7}$$

where $\mathbf{E}$ is the Green-Lagrange strain tensor, and $\mathbb{C}$ is the spatial tangent tensor, which relates to $\mathbb{D}$ through

$$\mathbb{C} = \frac{1}{J}\mathbf{F}\mathbf{F}\mathbb{D}\mathbf{F}^T\mathbf{F}^T. \tag{9.8}$$

Also, we can rewrite the term (2) of the integrant in Equation (9.2) as

$$\begin{aligned}
\frac{1}{2}\mathbf{S}\cdot\left(\delta\mathbf{F}^T\mathbf{F},_\theta + \mathbf{F},_\theta^T\,\delta F\right) &= \frac{1}{2}\mathbf{S}\cdot\left[\mathbf{F}^T(\bigtriangledown\delta\mathbf{u})^T\bigtriangledown\mathbf{u},_\theta\mathbf{F} + \mathbf{F}^T(\bigtriangledown\mathbf{u},_\theta)^T\bigtriangledown\delta\mathbf{u}\mathbf{F}\right]\\
&= \boldsymbol{\tau}\cdot(\bigtriangledown\delta\mathbf{u})^T\bigtriangledown\mathbf{u},_\theta\\
&= \bigtriangledown\delta\mathbf{u}\cdot(\mathbf{1}\boxtimes\boldsymbol{\tau})\bigtriangledown\mathbf{u},_\theta\\
&= \bigtriangledown\delta\mathbf{u}\cdot(\mathbf{1}\boxtimes J\boldsymbol{\sigma})\bigtriangledown\mathbf{u},_\theta
\end{aligned} \tag{9.9}$$

where, $\boldsymbol{\tau}$ is the Kirchhoff stress tensor and is related to the Cauchy stress tensor and the second Piola-Kirchhoff stress tensors through

$$\boldsymbol{\tau} = J\boldsymbol{\sigma} = \mathbf{F}^T\mathbf{S}\mathbf{F}. \tag{9.10}$$

Following the rule of tensor contraction

$$\mathbf{A} \cdot (\mathbf{B}\mathbf{C}) = \left(\mathbf{A}\mathbf{C}^T\right) \cdot \mathbf{B} = \left(\mathbf{B}^T\mathbf{A}\right) \cdot \mathbf{C} \tag{9.11}$$

where $\mathbf{A}$, $\mathbf{B}$ and $\mathbf{C}$ are any second order tensors, we obtain

$$\begin{aligned} \mathbf{S},_\theta \cdot \delta\mathbf{C} &= \mathbf{S},_\theta \cdot \left(\delta\mathbf{F}^T\mathbf{F} + \mathbf{F}^T\delta\mathbf{F}\right) \\ &= \mathbf{S},_\theta \cdot \left(\delta\mathbf{F}^T\mathbf{F}\right) + \mathbf{S},_\theta \cdot \left(\mathbf{F}^T\delta\mathbf{F}\right) \\ &= \left(\delta\mathbf{F}\mathbf{S},_\theta\right) \cdot \mathbf{F} + \left(\mathbf{F}\mathbf{S},_\theta\right) \cdot \delta\mathbf{F}. \end{aligned} \tag{9.12}$$

Substituting Equation (9.4) to Equation (9.12) yields

$$\begin{aligned} \mathbf{S},_\theta \cdot \delta\mathbf{C} &= \left(\bigtriangledown\delta\mathbf{u}\right)\mathbf{F}\mathbf{S},_\theta \cdot \mathbf{F} + \left(\mathbf{F}\mathbf{S},_\theta\right) \cdot \left(\bigtriangledown\delta\mathbf{u}\right)\mathbf{F} \\ &= 2\left(\bigtriangledown\delta\mathbf{u}\right) \cdot \left(\mathbf{F}\mathbf{S},_\theta \mathbf{F}^T\right) \\ &= 2\left(\bigtriangledown\delta\mathbf{u}\right) \cdot \boldsymbol{\tau},_\theta \\ &= 2\left(\bigtriangledown\delta\mathbf{u}\right) \cdot J\boldsymbol{\sigma},_\theta, \end{aligned} \tag{9.13}$$

where, $\boldsymbol{\tau},_\theta = J\boldsymbol{\sigma},_\theta = \mathbf{F}^T\mathbf{S},_\theta \mathbf{F}$. It follows that term (3) of the integrant in Equation

(9.2) can be rewritten as

$$\frac{1}{2}\mathbf{S},_{\theta}\cdot\delta\mathbf{C} = (\bigtriangledown\delta\mathbf{u})\cdot\boldsymbol{\tau},_{\theta} = (\bigtriangledown\delta\mathbf{u})\cdot J\boldsymbol{\sigma},_{\theta}. \tag{9.14}$$

Consequently, Equation (9.2) turns into

$$\int_{\Omega}\bigtriangledown\delta\mathbf{u}\cdot[\mathbb{C}+\mathbf{1}\boxtimes\boldsymbol{\tau}]\bigtriangledown\mathbf{u},_{\theta}\,dv + \int_{\Omega}\bigtriangledown\delta\mathbf{u}\cdot\boldsymbol{\tau},_{\theta}\,dv = 0. \tag{9.15}$$

which is the first order sensitivity equation.

Notice that Equation (9.15) is a linear equation after the nonlinear state problem is converged at the current load step. In addition, the stiffness matrix for sensitivity equation is the same as that of the state problem. Hence, after the state problem is converged, we can compute the new internal resistance force which is represented by the second integral in Equation (9.15), and solve a linear equation to obtain the sensitivity of nodal displacements with respect to the material parameters. After obtaining the displacement sensitivity, we can conduct post-processing to obtain the sensitivity of the Cauchy stress with respect to the material parameters by using

$$\frac{d\mathbf{S}}{d\theta} = \frac{\partial\mathbf{S}}{\partial\theta} + \frac{\partial\mathbf{S}}{\partial\mathbf{F}}\frac{\partial\mathbf{F}}{\partial\theta}, \tag{9.16}$$

where $\frac{\partial\mathbf{S}}{\partial\theta}$ denotes the explicit dependence of the stress tensor on the material parameters, and $\frac{\partial\mathbf{S}}{\partial\mathbf{F}}\frac{\partial\mathbf{F}}{\partial\theta}$ denotes the implicit dependence of the stress on the material parameters due to the deformation gradient.

In the current study, we are only concerned with membrane structures. Therefore, the sensitivity of membrane stress resultant or tension with respect to the material parameter is computed. In component form, the stress sensitivity is

$$\frac{dt^{\alpha\beta}}{d\theta} = \frac{\partial t^{\alpha\beta}}{\partial\theta} + \frac{\partial t^{\alpha\beta}}{\partial g_{\gamma\delta}}\frac{\partial g_{\gamma\delta}}{\partial\theta}, \tag{9.17}$$

where $g_{\alpha\beta}$ are the components of the current metric tensor which depends on the forward deformation.

In inverse elastostatics problems, the sensitivity equation can be derived by differentiating with respect to the material parameters the weak form constructed on the current configuration. The formulation is similar except that the geometric stiffness is absent because the the strain-displacement matrix $\mathbf{B}$ in linearizing the weak form depends on the current configuration which is fixed in the inverse formulation. Thus, the term $\mathbf{1} \boxtimes \boldsymbol{\tau}$ in Equation (9.15) vanishes.

After the sensitivity of inverse displacement with respect to the material parameters is obtained, the stress sensitivity can be computed by

$$\frac{dt^{\alpha\beta}}{d\theta} = \frac{\partial t^{\alpha\beta}}{\partial\theta} + \frac{\partial t^{\alpha\beta}}{\partial G_{\gamma\delta}}\frac{\partial G_{\gamma\delta}}{\partial\theta}, \tag{9.18}$$

which is slightly different from Equation (9.18) in that the implicit dependence of the stress is through $G_{\alpha\beta}$, the metric tensor components in the stress-free configuration.

9.2 Numerical example

In this numerical example, we will conduct continuum sensitivity analysis for the membrane stress with respect to the material property of the cerebral aneurysm model introduced in Chapter 5. The strain-energy function of neo-Hookean type (cf. Equation (5.1)) will be used to demonstrate the material sensitivity of membrane stress. The neo-Hookean strain energy function is

$$w = \frac{\mu_1}{2}\left(I_1 - 2\log J - 2\right) + \frac{\mu_2}{4}\left(I_1 - 2\right)^2, \tag{9.19}$$

where the elastic parameters μ_1 and μ_2 are set to be

$$\mu_1 = 0.06521739 \text{ N/mm}, \quad \mu_2 = 0.1521739\text{N/mm}. \tag{9.20}$$

Differentiating the strain energy function w with respect to the current covariant metric tensor $g_{\alpha\beta}$ and pushing forward to the current configuration yields the Cauchy stress

$$t^{\alpha\beta} = \frac{\partial w}{\partial g_{\alpha\beta}} = \frac{1}{J}\left\{\left[\mu_1 + \mu_2\left(I_1 - 2\right)\right] G^{\alpha\beta} - \mu_1 g^{\alpha\beta}\right\}. \tag{9.21}$$

Multiplying the area change ratio J to the above equation gives the Kirchhoff stress tensor components

$$\tau^{\alpha\beta} = \left[\mu_1 + \mu_2\left(I_1 - 2\right)\right] G^{\alpha\beta} - \mu_1 g^{\alpha\beta}. \tag{9.22}$$

Since the virtual force $\boldsymbol{\tau}_{,\theta}$ (θ stands for the elastic parameters μ_1 or μ_2 in here) need be constructed for the purpose of computing the sensitivity of nodal displacement with respect to the elastic parameters μ_1 or μ_2, we subsequently differentiate the Kirchhoff stress components $\tau^{\alpha\beta}$ with respect to the two parameters as

$$\begin{aligned}\frac{\partial \tau^{\alpha\beta}}{\partial \mu_1} &= G^{\alpha\beta} - g^{\alpha\beta}, \\ \frac{\partial \tau^{\alpha\beta}}{\partial \mu_2} &= \left(I_1 - 2\right) G^{\alpha\beta}.\end{aligned} \tag{9.23}$$

The sensitivities of membrane stress with respect to the elastic parameters in the strain-energy function of neo-Hookean type (cf. Equation (5.1)) were computed for the cerebral aneurysm model described in Chapter 5 by using direct differentiation method (DDM). Two scenarios were considered. The first one was a forward analysis, and the second one was an inverse analysis. In the forward analysis, the stress-free configuration was known and the sensitivity of the membrane stress with respect to the elastic parameters was computed. Given a stress-free configuration and its pressure loading and clamped boundary conditions, one can obtain a different deformed configuration if the material property is changed, which produces different stress in the deformed configuration. Therefore, the sensitivity of stress is non-trivial. However, in the inverse analysis, the deformed configuration and its pressure loading and displacement boundary conditions are known. Due to the static determinacy of the membrane stress, the stress is insensitive to the variation of the material property. Or in other words, the stress sensitivity should be close to zero.

For both scenarios, the transmural pressure was set to be 110 mmHg. The DDM results are validated through central finite difference method and forward finite difference method using the same finite element model. For the two finite difference methods, we chose the same step size, i.e., 1% of elastic parameters. In inverse sensitivity analysis, linear and quadratic membrane elements were used for comparison.

9.3 Results

9.3.1 Linear elements

Figure 9.1 and Figure 9.2 show the distribution of the sensitivity of the stress components with respect to elastic parameters μ_1 and μ_2, respectively, computed by DDM for the *foward* analysis. As can be seen from the figures, the sensitivity of membrane stress is non-uniform over the sac, and it is dependent on the geometry of the reference geometry. If the curvature in a region is relatively small, or in another word, the surface is flatter, the membrane is more prone to deformation. Hence, the stress is more dependent on the material property of this region.

Figure 9.3 and Figure 9.4 show the distribution of the sensitivity of the stress components with respect to elastic parameters μ_1 and μ_2, respectively, computed by DDM for the *inverse* analysis. As can be seen from the figures, the stress sensitivity is almost uniformly small in the region distanced from the clamped boundary. Near the boundary, the sensitivity is relatively larger due to the boundary effect. Table 9.1 and 9.2 list the statistical quantities of the stress sensitivity with respect to the elastic parameters μ_1 and μ_2, respectively, by using linear triangular elements. The mean sensitivity is in the order of 10^{-3}.

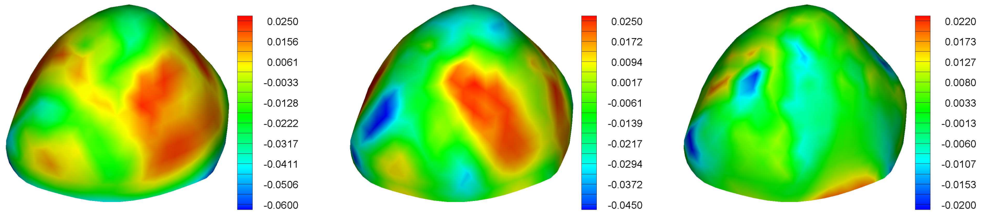

(a) (b) (c)

Figure 9.1: Sensitivity of the stress components with respect to elastic parameter μ_1 in forward analysis: (a) t^{11}, (b) t^{22}, (c)t^{12}.

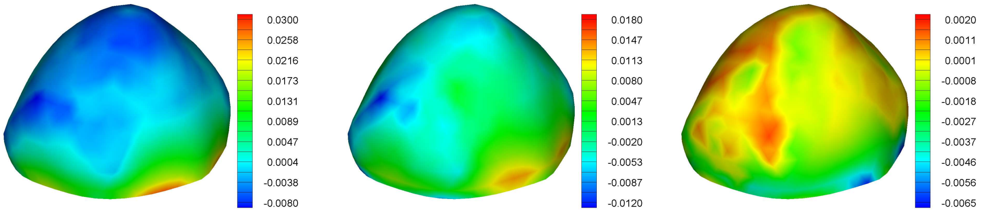

(a) (b) (c)

Figure 9.2: Sensitivity of the stress components with respect to elastic parameter μ_2 in forward analysis: (a) t^{11}, (b) t^{22}, (c)t^{12}.

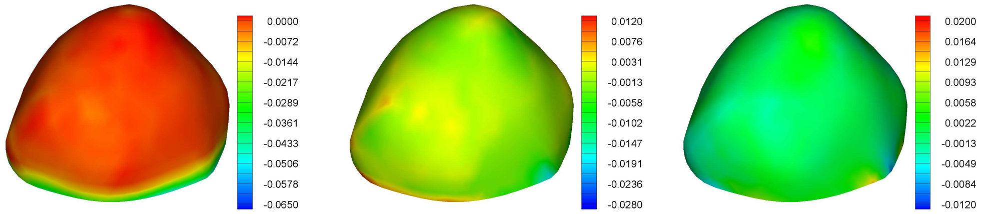

(a) (b) (c)

Figure 9.3: Sensitivity of the stress components with respect to elastic parameter μ_1 in inverse analysis: (a) t^{11}, (b) t^{22}, (c)t^{12}.

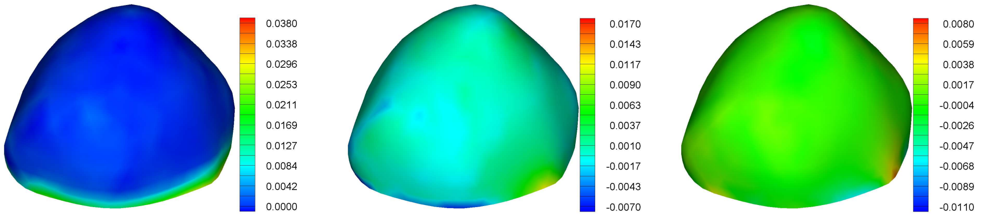

(a) (b) (c)

Figure 9.4: Sensitivity of the stress components with respect to elastic parameter μ_2 in inverse analysis: (a) t^{11}, (b) t^{22}, (c)t^{12}.

Table 9.1: Means, minimums and maximums of the stress sensitivity with respect to μ_1 using linear elements.

	t^{11}	t^{22}	t^{12}
Mean	1.04×10^{-2}	8.36×10^{-3}	3.52×10^{-3}
Min	1.91×10^{-5}	2.76×10^{-6}	2.14×10^{-6}
Max	1.03×10^{-1}	6.82×10^{-2}	4.19×10^{-2}

Table 9.2: Means, minimums and maximums of the stress sensitivity with respect to μ_2 using linear elements.

	t^{11}	t^{22}	t^{12}
Mean	5.92×10^{-3}	4.84×10^{-3}	1.82×10^{-3}
Min	6.16×10^{-6}	6.96×10^{-6}	1.60×10^{-7}
Max	5.32×10^{-2}	2.94×10^{-2}	2.37×10^{-2}

Table 9.3: Means, minimums and maximums of the stress sensitivity with respect to μ_1 using quadratic elements.

	t^{11}	t^{22}	t^{12}
Mean	5.34×10^{-4}	3.83×10^{-4}	2.69×10^{-4}
Min	0	0	0
Max	2.06×10^{-2}	1.59×10^{-2}	6.96×10^{-3}

Table 9.4: Means, minimums and maximums of the stress sensitivity with respect to μ_2 using quadratic elements.

	t^{11}	t^{22}	t^{12}
Mean	2.40×10^{-4}	1.75×10^{-4}	7.47×10^{-5}
Min	0	0	0
Max	9.23×10^{-3}	7.00×10^{-3}	2.40×10^{-3}

9.3.2 Quadratic elements

Due to the curved surface of the aneurysm model, linear elements may not describe the geometry of the surface accurately enough. Therefore, we used quadratic nine-node membrane elements to compute the stress sensitivity again. Table 9.3 and 9.4 list the statistical quantities of the stress sensitivity with respect to the elastic parameters μ_1 and μ_2, respectively, by using nine-node elements.

As we expected, the computed sensitivity is closer to zero. The mean sensitivity is in the order of 10^{-4}. Dr. Lu's group is investigating into utilizing NURBS finite element method to conduct stress analysis for curved surfaces and solids. The recent work can be found in [90]. NURBS can provide more accurate description of the curves and surfaces than linear and quadratic traditional finite elements do. Therefore, it is reasonable to expect that the stress sensitivity computed using NURBS finite element will capitalize the material insensitivity of membrane stress more accurately.

CHAPTER 10
CONCLUSIONS

10.1 Summary of major findings

The presented work is motivated by the big challenge in delineating the distribution of elastic properties in heterogeneous materials and the demand in accurately characterizing the mechanical behaviors of normal and diseased human tissues and organs in vivo. The objective in this study is to develop a pointwise method which can delineate the heterogeneous elastic properties in membrane structures and explore the possibility in the application of the method to thin biological tissues and organs. The extension of the method into in vivo identification is also attempted. The major contributions of this study are listed below.

- Developed a pointwise method for identifying the elastic properties in heterogeneous nonlinear membranes. This method provides an un-reprecedented capability to delineate pointwise the heterogeneous anisotropic properties in thin membranes. Static determinacy in curved membranes is long known; in this work, this property was for the first time systematically utilized to characterize material properties.

- Designed an inflation experiment for membranes of general shape, and conducted experimental validation for the method using an inflation test on a rubber balloon. Inflation tests reported in the literature were implemented exclusively for axisymmetric membranes. In the applications reported in the literature, the objects of interest were normally approximated as axisymmstric even though not so. The experiment designed in this work is the first one which treats the geometry as it is without any approximation. The experimental work not only validated the concept of PWIM, but also opened a pathway for designing new experimental systems for organ level tests. Moreover, the experiments suggested a systematic way to identify isotropic versus anisotropic responses without making *a prior* assumption about material symmetry.

- Conducted numerical validation for an anisotropic cerebral aneurysm model with specific distribution of collagen fibers. The validation not only proved that the proposed method can be applied to identify the elastic parameters for anisotropic materials if fiber orientation is known, but also showed the feasibility of identifying fiber orientation for some types of material symmetry.

- Conducted an inflation experiment on a rabbit urinary bladder and identified its distributive elastic properties using PWIM. The work is rather preliminary at this stage, and there are a number of issues yet to be addressed. However, the test was the first attempt ever to delineate the distributive elastic properties of urinary bladders using whole bladder experiments.

- Introduced the concept of local stress-free configuration for membranes and applied to elastic property identification for the first time. The availability of pointwise stress-strain data offers us an opportunity to parameterize the *local* stress-free configuration at a material point of a membrane, and treat it as model parameters in elastic parameter identification. This practice will enhance greatly the possibility of in vivo elastic property identification solely from medical images. This idea was realized numerically for both isotropic and anisotropic materials in this study.

10.2 Future work

The pointwise identification method presented in this work is a novel method. Both its advantages and limitations will open opportunities for future development and applications.

Like most experimental methods which require measurement and data collection, the current method has the issue of accuracy in data acquisition. Since the membrane stress in dependent of the membrane surface geometry and transmural pressure, the accuracy of the surface geometry description is crucial to the accuracy of stress computation. In the rubber balloon test of this work, the finite element mesh drawn on the balloon surface could not be considered fine enough to capture the surface geometry accurately. In order to improve the accuracy of stress computation, one may use a finer mesh or higher order elements to describe the surface, which needs more extensive effort. Another option is to conduct 3-D reconstruction using more advanced techniques, e.g., 3-D Laser Scanning. In addition, the accuracy of strain measurement is dependent of how accurate the displacement of the tracking markers or FE nodes can be measured. In this work, when performing 3-D reconstruction using photogrammetry, the point-to-point correspondence was determined by manually picking the points on the images, which might introduced some amount of human error. In order to reduce human input to the process, an automatic procedure is needed.

The experiments conducted on rubber balloon and rabbit urinary bladder showed that the proposed method is effective in whole organ identification. Whole organ identification can be done in vitro or ex vivo for various biological tissues and organs, e.g., skins, cornea, etc.. However, in order for accurate identification of the elastic parameters for tissues of significant anisotropic mechanical behavior, information on fiber orientation is needed, although this work showed that fiber direction can also be identified if certain material symmetry type (e.g., transverse isotropy or orthotropy) is legitimate to assume. Nevertheless, the actual microstructure is very complex in biological tissues, therefore any assumption may bring certain level of inaccuracy in the final results of elastic parameter identification. Research in combining the proposed method and fiber orientation reconstruction will be valuable in identifying the elastic properties in anisotropic biological tissues and organs.

The extension of this work is to apply the proposed method to identify the distributive elastic properties in diseased human tissues and organs. An ideal application would be in cerebral aneurysms. However, the feasibility depends heavily on the advancement of image segmentation and registration techniques in deformation tracking for thin biological structures. Research has been very active in deformation tracking for the heart and arteries from medical images. However, it is relatively more difficult to track the deformation of thin organs, e.g., cerebral aneurysms. One reason is that the thinness of the aneurysm wall requires very high resolution of the imaging techniques. Provided with mature deformation tracking methods for thin biological structures, exploration toward in vivo elastic property identification from medical images will be valuable to biomedical engineering and medical science.

Often times, the evolution of the elastic properties in diseased tissues is more important than those at a particular moment. By retrospecting the time history of the material property, one may be able to predict what probably is going to happen next. Take for example human cerebral aneurysms. By applying the proposed method to identify (in vivo) the elastic properties, e.g., the effective wall stiffness, of the aneurysm at multiple instances, a database of the elastic property evolution may be established. Although we cannot prevent the initialization of an aneurysm, we may predict the future evolution of its wall material property from its time history using appropriate models. This may help the doctor to evaluate the rupture risk of the aneurysm and decide whether to leave it alone or conduct treatment.

There is a need to investigate the viscoelastic properties of thin soft tissues since most biological soft tissues exhibit viscoelastic response. The proposed method can be applied to this situation with slight modification. By conducting a creep test on an inflated thin tissue while keeping the transmural pressure constant, and recording continuously the deformed configurations, the time-history of pointwise stress-strain relation can be obtained, from which the distribution of viscoelastic properties can be identified.

REFERENCES

[1] J. E. Adkins. A reciprocal property of the finite plane strain equations. *Journal of the Mechanics and Physics of Solids*, 6:267–275, 1958.

[2] J. E. Adkins and R. S. Rivlin. Large elastic deformations of isotropic materials IX. The deformation of thin shells. *Philosophical transactions of the Royal Society of London*, pages 505–531, 1952.

[3] H. Alexander. A constitutive relation for rubber-like materials. *International Journal of Engineering Science*, 6:549–563, 1968.

[4] R. S. Alexander. Mechanical properties of urinary bladders. *American Journal of Physiology*, 220:1413–1421, 1971.

[5] R. S. Alexander. Series elasticity of urinary bladder smooth muscle. *American Journal of Physiology*, 231(5):1337–1342, 1976.

[6] L. Axel and L. Dougherty. Heart wall motion: improved method of spatial modulation of magnetization for MR imaging. *Radiology*, 172(2):349–350, 1989.

[7] L. Axel and L. Dougherty. MR imaging of motion with spatial modulation of magnetization. *Radiology*, 171(3):841–845, 1989.

[8] R. C. Batra. Universal relations for transversely isotropic materials. *Mathematics and Mechanics of Solids*, 7:421–437, 2002.

[9] M. F. Beatty. A class of universal relations in isotropic elasticity. *Journal of Elasticity*, 17:113–121, 1987.

[10] M. F. Beatty. A class of universal relations for constrained, isotropic elasticity materials. *Archives of Mechanics*, 80:299–312, 1989.

[11] T. Belytschko, W. K. Liu, D. Organ, M. Fleming, and P. Krysl. Meshless methods: an overview and recent developments. *Computer Methods in Applied Mechanics and Engineering, special issue on Meshless Methods*, 139:3–47, 1996.

[12] P. L. Blatz and W. L. Ko. Application of finite elasticity theory to the deformation of rubber materials. *Transactions of the Society of Rheology*, 6:223–251, 1962.

[13] P. B. Canham, H. M. Finlay, and S. Y. Tong. Stereological analysis of the layered collagen of human intracranial aneurysms. *Journal of Microscopy*, 183:170–180, 1996.

[14] D. E. Carlson and R. T. Shield. Inverse deformation results in elastic materials. *Journal of Applied Mathematics and Physics (ZAMP)*, 20:261–263, 1969.

[15] A. J. Carmichael and H. W. Holdaway. Phenomenological elastomechanical behavior of rubbers over wide ranges of strain. *Journal of Applied Physics*, 32:159–166, 1961.

[16] J. R. Cebral, M. Hernandez, A. Frangi, C. Putman, R. Pergolizzi, and J. Burgess. Subject-specific modeling of intracranial aneurysms. *Proc. SPIE*, 5369:319–327, 2004.

[17] P. Chadwick. Applications of an energy-momentum tensor in nonlinear elastostatics. *Journal of Elasticity*, 5:249–258, 1975.

[18] S. L. Chang, J. S. Chung, M. K. Yeung, P. S. Howard, and E. J. Macarak. Roles of the lamina propria and the detrusor in tension transfer during bladder filling. *Scandinavian Journal of Urology and Nephrology*, 33:38–45, 1999.

[19] K. K. Choi and N. H. Kim. *Structural Sensitivity Analysis and Optimization I: Linear Systems*. Springer, New York, 2005.

[20] K. K. Choi and N. H. Kim. *Structural Sensitivity Analysis and Optimization II: Nonlinear Systems and Applications*. Springer, New York, 2005.

[21] C. J. Chuong and Y. C. Fung. Three-dimensional stress distribution in arteries. *ASME Journal of Biomechanical Engineering*, pages 268–274, 1983.

[22] C. J. Chuong and Y. C. Fung. Residual stress in arteries. In G. W. Schmid-Schonbein, S. L. Y. Woo, and B. W. Zweifach, editors, *Frontiers in Biomechanics*, pages 117–129. Springer, New York, 1986.

[23] B. L. Coolsaet, W. A. van Duyl, R. van Mastrigt, and J. W. Schouten. Viscoelastic properties of bladder wall strips. *Investigative Urology*, 12(5):351–356, 1975.

[24] D. E. Coplen, E. J. Macarak, and R. M. Levin. Developmental changes in normal fetal bovine whole bladder physiology. *The Journal of Urology*, 151(5):1391–5, 1994.

[25] M. R. Crompton. Mechanism of growth and rupture in cerebral berry aneurysms. *British Medical Journal*, 1:1138–1142, 1966.

[26] S. E. Dahms, H. J. Piechota, R. Dahiya, T. F. Lue, and E. A. Tanagho. Composition and biomechanical properties of the bladder acellular matrix graft: comparative analysis in rat, pig and human. *British Journal of Urology*, 82(3):411–419, 1998.

[27] M. S. Damaser. Whole bladder mechanics during filling. *Scandinavian Journal of Urology and Nephrology*, pages 51–58, 1999.

[28] A. Delfino, N. Stergiopulos, J. E. Moore, and J. J. Meister. Residual strain effects on the stress field in a thick wall finite element model of the human carotid bifurcation. *Journal of Biomechanics*, 30:777–786, 1997.

[29] M. T. Draney, F. R. Arko, M. T. Alley, M. Markl, R. J. Herfkens, N. J. Pelc, C. K. Zarins, and C. A. Taylor. Quantification of vessel wall motion and cyclic strain using cine phase contrast MRI: in vivo validation in the porcine aorta. *Magnetic Resonance in Medicine*, 52(2):286–295, 2004.

[30] M. T. Draney, R. J. Herfkens, T. J. R. Hughes, N. J. Pelc, K. L. Wedding, C. K. Zarins, and C. A. Taylor. Quantification of vessel wall cyclic strain using cine phase contrast magnetic resonance imaging. *Annals of Biomedical Engineering*, 30(8):1033–1045, 2002.

[31] N. J. B. Driessen, C. V. C. Bouten, and F. P. T. Baaijens. A structural constitutive model for collengenous cardiovascular tissues incorporating the angular fiber distribution. *ASME Journal of Biomechanical Engineering*, 127:494–503, 2005.

[32] D. F. Elger, D. M. Blackketter, R. S. Budwig, and K. H. Johansen. The influence of shape on the stresses in model abdominal aortic aneurysms. *Journal of Biomechanical Engineering - Transactions of the ASME*, 118:326–332, 1996.

[33] M. Epstein and G.A. Maugin. The energy-momentum tensor and material uniformity in finite elasticity. *Acta Mechanica*, 3(3-4):127–133, 1990.

[34] M. Epstein and G.A. Maugin. On the geometrical material structure of anelasticity. *Acta Mechanica*, 115:119–131, 1996.

[35] D. O. Wiebers et al. Unruptured intracranial aneurysms risk of rupture and risks of surgical intervention. international study of unruptured intracranial aneurysms investigators. *The New England Journal of Medicine*, 339:1725–1733, 1998.

[36] D. H. Ewalt, P. S. Howard, B. Blyth, H. M. Snyder, J. W. Duckett, R. M. Levin, and E. J. Macarak. Is lamina propria matrix responsible for normal bladder compliance? *The Journal of Urology*, 148(2 Pt 2):544–9, 1992.

[37] H. O. Foster. Very large deformations of axially symmetrical membranes made of neo-Hookean materials. *International Journal of Engineering Science*, 5:95–117, 1967.

[38] Y. C. Fung. *Biomechanics; Motion, Flow, Stress and Growth*. Springer-Verlag, New York, 1990.

[39] Y. C. Fung, K. Fronek, and P. Patitucci. Pseudoelasticity of arteries and the choice of its meathematical expression. *American Journal of Physiology*, 237:H620–H631, 1979.

[40] Y. C. Fung and S. Q. Liu. Change of residual strains in arteries due to hypertrophy caused by aortic constriction. *CR*, 65(5):1340–1349, 1989.

[41] A. N. Gent and A. G. Thomas. Forms of the stored (strain) energy function for vulcanized rubber. *Journal of Polymer Science*, 28:625–628, 1958.

[42] R. H. Gerke. Thermodynamics of stressed vulcanized rubber. *Industrial and Engineering Chemistry*, 22:73–77, 1930.

[43] P. E. Gill, W. Murray, and M. A. Saunders. SNOPT: An SQP algorithm for large-scale constrained optimization. *SIAM Review*, 47:99–131, 2005.

[44] D. C. Gloeckner, M. S. Sacks, M. O. Fraser, G. S. Somogyi, W. C. d. Groat, and M. B. Chancellor. Passive biaxial mechanical properties of the rat urinary bladder wall after spinal cord injury. *The Journal of Urology*, 167:2247–2252, 2002.

[45] S. Govindjee and P. A. Mihalic. Computational methods for inverse finite elastostatics. *Computer Methods in Applied Mechanics and Engineering*, 136:47–57, 1996.

[46] S. Govindjee and P. A. Mihalic. Computational methods for inverse deformations in quasi-incompressible finite elasticity. *International Journal for Numerical Methods in Engineering*, 43:821–838, 1998.

[47] A. E. Green and J. E. Adkins. *Large elastic deformations and non-linear continuum mechanics*. Clarendon Press, Oxford, 1960.

[48] A. E. Green and J. E. Adkins. *Large Elastic Deformations*. Clarendon Press, Oxford, 2nd edition, 1970.

[49] A. E. Green and R. S. Rivlin. On cauchy's equation of motion. *Journal of Applied Mathematics and Physics (ZAMP)*, 15:290–292, 1964.

[50] F. Gruttmann and R. L. Taylor. Theory and finite element formulation of rubberlike membrane shells using principal stretches. *International Journal for Numerical Methods in Engineering*, 35:1111–1126, 1992.

[51] M. C. Jimenez Hamann, M. S. Sacks, and T. I. Malinin. Quantification of the collagen fibre architecture of human cranial dura mater. *Journal of Anatomy*, 192:99–106, 1998.

[52] L. J. Hart-Smith. Elasticity parameters for finite deformations of rubber-like materials. *Journal of Applied Mathematics and Physics (ZAMP)*, 17:608–626, 1966.

[53] L. J. Hart-Smith and J. D. C. Crisp. Large elastic deformations of thin rubber membranes. *International Journal of Engineering Science*, 5:1–24, 1967.

[54] M. Hayes and R. B. Knops. On universal relations in elasticity theory. *Journal of Applied Mathematics and Physics (ZAMP)*, 17:636–639, 1966.

[55] J. M. Hill. On a duality of stress and deformation fields in finite elasticity. *Journal of Elasticity*, 3:51–56, 1973.

[56] J. M. Hill and R. T. Shield. Notes on a duality of stress and deformation fields in plane finite elasticity. *Journal of Elasticity*, 4:167–172, 1974.

[57] A. Hoger. The constitutive equation for finite deformations of a transversely isotropic hyperelastic material with residual stress. *Journal of Elasticity*, 33:107–118, 1993.

[58] A. Hoger. Virtual configurations and constitutive equations for residually stressed bodies with material symmetry. *Journal of Elasticity*, 48:125–144, 1997.

[59] G. A. Holzapfel. Determination of material models for arterial walls from uniaxial extension tests and histological structure. *Journal of Theoretical Biology*, 238:290–302, 2006.

[60] G. A. Holzapfel, T. G. Gasser, and R. W. Ogden. A new constitutive framework for arterial wall mechanics and a comparative study of material models. *Journal of Elasticity*, 61:1–48, 2000.

[61] F. P. K. Hsu, A. C. M. Liu, J. Downs, D. Rigamonti, and J. D. Humphrey. A triplane video-based experimental system for studying axisymmetrically inflated biomembranes. *IEEE Transactions on Biomedical Engineering*, 42:442–450, 1995.

[62] F. P. K. Hsu, C. Schwab, D. Rigamonti, and J. D. Humphrey. Identification of response functions from axisymmetrical membrane inflation tests - implications for biomechanics. *International Journal of Solids and Structures*, 31:3375–3386, 1994.

[63] T. J. R. Hughes, J. A. Cottrell, and Y. Bazilevs. Isogeometric analysis: CAD, finite elements, NURBS, exact geometry and mesh refinement. *Computer Methods in Applied Mechanics and Engineering*, 194:4135–4195, 2005.

[64] J. D. Humphrey. Mechanicsl of the arterial wall: Review and Directions. *Critical Reviews in Biomedical Engineering*, 23:1–162, 1995.

[65] J. D. Humphrey. *Cardiovascular Solid Mechanics: Cells, Tissues, and Organs.* Springer, New York, 2002.

[66] J. D. Humphrey. Intracranial saccular aneurysms. In *Biomechanics of Soft Tissue in Cardiovascular Systems*, CISM Courses and Lectures No. 441 (Udine, Italy), pages 185–220. Springer, New York, 2003.

[67] J. D. Humphrey and P. B. Canham. Structure, mechanical properties, and mechanics of intracranial saccular aneurysms. *Journal of Elasticity*, 61:49–81, 2000.

[68] J. D. Humphrey, R. K. Strumpf, and F. C. P. Yin. Determination of a constitutive relation for passive myocardium. II. parameter-estimation. *ASME Journal of Biomechanical Engineering*, 112(3):340–346, 1990.

[69] R. H. Iding, K. S. Pister, and R. L. Taylor. Identification of nonlinear elastic solids by a finite element method. *Computer Methods in Applied Mechanics and Engineering*, 4:121–142, 1974.

[70] F. Inzoli, F. Boschetti, M. Zappa, T. Longo, and R. Fumero. Biomechanical factors in abdominal aortic-aneurysm rupture. *European Journal of Vascular Surgery*, 7:667–674, 1993.

[71] J. G. Isaksen, Y. Bazilevs, T. Kvamsdal, Y. Zhang, J. H. Kaspersen, K. Waterloo, B. Romner, and T. Ingebrigtsen. Determination of wall tension in cerebral artery aneurysms by numerical simulation. *Stroke*, 39(12):3172–3178, 2008.

[72] E. R. Jacobs and A. Hoger. The use of a virtual configuration in formulating constitutive equations for residually stressed elastic materials. *Journal of Elasticity*, 41:177–215, 1995.

[73] N. F. Kassel and J. C. Torner. Size of intracranial aneurysms. *Neurosurgery*, 12:291–297, 1983.

[74] K. T. Kavanagh and R. W. Clough. Finite element applications in the characterization of elastic solids. *International Journal of Solids and Structures*, 7:11–23, 1971.

[75] M. Kleiber, H. Antunez, T. D. Hien, and P. Kowalczyk. *Parameter Sensitivity in Nonlinear Mechanics: Theory and Finite Element Computations*. Wiley, New York, 1997.

[76] W. W. Klingbeil and R. T. Shield. Some numerical investigations on empirical strain energy functions in the large axi-symmetric extensions of rubber membranes. *Journal of Applied Mathematics and Physics (ZAMP)*, 15:608–629, 1964.

[77] M. Kroon and G. A. Holzapfel. Estimation of the distribution of anisotropic, elastic properties and wall stresses of saccular cerebral aneurysms by inverse analysis. *Proceedings of the Royal Society of London, Series A*, 464:807–825, 2008.

[78] M. Kroon and G. A. Holzapfel. A new constitutive model for multi-layered collagenous tissues. *Journal of Biomechanics*, 41:2766–2771, 2008.

[79] S. K. Kyriacou, A. D. Shah, and J. D. Humphrey. Inverse finite element characterization of nonlinear hyperelastic membranes. *Journal of Applied Mechanics-Transactions of the ASME*, 64:257–262, 1997.

[80] Y. Lanir and Y. C. Fung. Two-dimensional mechanical properties of rabbit skin. I. experimental system. *Journal of Biomechanics*, 7:29–34, 1974.

[81] Y. Lanir and Y. C. Fung. Two-dimensional mechanical properties of rabbit skin. II. experimental results. *Journal of Biomechanics*, 7:171–182, 1974.

[82] R. M. Levin, P. Horan, and S-P. Liu. Metabolic aspects of urinary bladder filling. *Scandinavian Journal of Urology and Nephrology*, 33:59–66, 1999.

[83] S. Li and W. K. Liu. Meshfree and particle methods and their application. *Applied Mechanics Review*, 55:1–34, 2002.

[84] S. Q. Liu and Y. C. Fung. Relationship between hypertension, hypertrophy, and opening angle of zero-stress state of arteries following aortic constriction. *Journal of Biomechanical Engineering-Transactions of the ASME*, 111:325–335, 1989.

[85] J. Lu. A covariant condition and related constitutive results in finite plasticity. *Journal of Applied Mathematics and Physics (ZAMP)*, 57:313–323, 2006.

[86] J. Lu and P. Papadopoulos. A covariant formulation of anisoptropic finite plasticity: theoretical development. *Computer Methods in Applied Mechanics and Engineering*, 193:5335–5358, 2004.

[87] J. Lu, X. Zhou, and M. L. Raghavan. Computational method of inverse elastostatics for anisotropic hyperelastic solids. *International Journal for Numerical Methods in Engineering*, 69:1239–1261, 2007.

[88] J. Lu, X. Zhou, and M. L. Raghavan. Inverse elastostatic stress analysis in pre-deformed biological structures: Demonstration using abdominal aortic aneurysm. *Journal of Biomechanics*, 40:693–696, 2007.

[89] J. Lu, X. Zhou, and M. L. Raghavan. Inverse method of stress analysis for cerebral aneurysms. *Biomechanics and Modeling in Mechanobiology*, 7:477–486, 2008.

[90] Jia Lu. Circular element: isogeometric elements of smooth boundary. *Computer Methods in Applied Mechanics and Engineering*, In press.

[91] T. Luhmann, S. Robson, S. Kyle, and I. Harley. *Close Range Photogrammetry, Principles, Methods and Applications*. Whittles Publishing, 2006.

[92] B. Ma, R. E. Harbaugh, and M. L. Raghavan. Three-dimensional geometrical characterization of cerebral aneurysms. *Annals of Biomedical Engineering*, 32:264–273, 2004.

[93] D. J. MacDonal, H. M. Finlay, and P. B. Canham. Directional wall strength in saccular brain aneurysms from polarized light microscopy. *Annals of Biomedical Engineering*, 28:533–542, 2000.

[94] G.A. Maugin and M. Epstein. Geometrical material structure of elastoplasticity. *International Journal of Plasticity*, 14:109–115, 1998.

[95] C. Miehe. A constitutive frame of elastoplasticity at large strains based on the notion of a plastic metric. *International Journal of Solids and Structures*, 35(30):3859–3897, 1998.

[96] M. Mooney. A theory of large elastic deformation. *Journal of Applied Physics*, 11:582–592, 1940.

[97] C. C. Moore, E. R. McVeigh, and E. A. Zerhouni. Quantitative tagged magnetic resonance imaging of the normal human left ventricle. *Topics in magnetic resonance imaging : TMRI*, 11(6):359–371, 2000.

[98] W. R. Mower, L. J. Baraff, and J. Sneyd. Stress distributions in vascular aneurysms: Factors affecting risk of aneurysm rupture. *Journal of Surgical Research*, 55:155–161, 1993.

[99] P. M. Naghdi. The theory of plates and shells. In C. Truesdell, editor, *Handbuch der Physik*, volume VIa/2, pages 425–640. Springer-Verlag, Berlin, New York, 1972.

[100] W. Noll. A new mathematical theory of simple material. *Archive for Rational Mechanics and Analysis*, 48:1–50, 1972.

[101] Y. Obata, S. Kawabata, and H. Kawai. Mechanical properties of natural rubber vulcanizates in finite deformation. *Journal of Polymer Science*, 8:903–919, 1970.

[102] R. W. Ogden. Large deformation isotropic elasticity - on the correlation of theory and experiment for incompressible rubberlike solids. *Proceedings of the Royal Society of London, Series A*, 326:565–584, 1972.

[103] R. W. Ogden. Dual reciprocal states in finite elasticity. *Journal of Elasticity*, 5:149–153, 1975.

[104] R. W. Ogden. A note on duality in finite elasticity. *Journal of Elasticity*, 5:83–88, 1975.

[105] R. W. Ogden. Elastic deformation of rubberlike solids. In H.G. Hopkins and M.J. Sewell, editors, *Mechanics of Solids, The Rodney Hill 60th anniversary volume*, pages 499–537. Pergamon Press, Oxford, 1982.

[106] T. Olsson, J. Stålhand, and A. Klarbring. Modeling initial strain distribution in soft tissues with application to arteries. *Biomechanics and Modeling in Mechanobiology*, 5:27–38, 2006.

[107] N. J. Pelc, R. J. Herfkens, A. Shimakawa, and D. R. Enzmann. Phase contrast cine magnetic resonance imaging. *Magnetic Resonance Quarterly*, 7(4):229–54, 1991.

[108] E. Pucci and G. Saccomandi. On universal relations in continuum mechanics. *Continuum Mechanics and Thermodynamics*, 9:61–72, 1997.

[109] R. D. Rabbitt, J. A. Weiss, G. E. Christensen, and M. I. Miller. Mapping of hyperelastic deformable templates using the finite element method. *SPIE*, 2573:252–265, 1995.

[110] M. L. Raghavan, B. Ma, and R. E. Harbaugh. Quantified aneurysm shape and rupture risk. *Journal of Neurosurgery*, 102:355–362, 2005.

[111] M. L. Raghavan, D. A. Vorp, M. P. Federle, M. S. Makaroun, and M. W. Webster. Wall stress distribution on three-dimensionally reconstructed models of human abdominal aortic aneurysm. *Journal of Vascular Surgery*, 31:760–769, 2000.

[112] R. S. Rivlin. Large elastic deformations of isotropic materials. IV. further developments of the general theory. *Proceedings of the Royal Society of London, Series A*, 241:368–397, 1948.

[113] R. S. Rivlin. Universal relations for elastic materials. *Rendiconti di Matematica*, 20:35–55, 2000.

[114] R. S. Rivlin and D. W. Saunders. Large elastic deformations of isotropic materials. VII. experiments on the deformation of rubber. *Proceedings of the Royal Society of London, Series A*, 243:251–288, 1951.

[115] R. S. Rivlin and K. N. Sawyers. The strain-energy function for elastomers. *Transactions of the Society of Rheology*, 20:545–557, 1976.

[116] E. K. Rodriguez, A. Hoger, and A. D. Mcculloch. Stress-dependent finite growth in soft elastic tissues. *Journal of Biomechanics*, 27:455–467, 1994.

[117] D. Rohrmann, S. A. Zderic, J. W. Duckett Jr, R. M. Levin, and M. S. Damaser. Compliance of the obstructed fetal rabbit bladder. *Neurourology and Urodynamics*, 16(3):179–189, 1997.

[118] J. N. Rossettos. Nonlinear membrane solutions for symmetrically loaded deep membranes of revolution. Technical Report NASA TN D-3297, NASA, 1966.

[119] G. Saccomandi and R. C. Batra. Additional universal relations for transversely isotropic materials. *Mathematics and Mechanics of Solids*, 9:167–174, 2004.

[120] G. Saccomandi and M. F. Beatty. Universal relations for fiber-reinforced materials. *Mathematics and Mechanics of Solids*, 7:95–110, 2002.

[121] M. S. Sacks. Biaxial mechanical evaluation of planar biological materials. *Journal of Elasticity*, 61:199–246, 2000.

[122] M. S. Sacks. Personal communication. 2008.

[123] L. R. Schmidt and J. F. Carley. Biaxial stretching of heat-softened plastic sheets using an inflation technique. *International Journal of Engineering Science*, 13:563–578, 1975.

[124] B. S. Schultze-Jena. Über die schraubenförmige Struktur der Arterienwand. *Genenbauers Morphologisches Jahrbuch*, 83:230–246, 1939.

[125] A. Scott, G. G. Ferguson, and M. R. Roach. Comparison of the elastic properties of human intracranial arteries and aneurysms. *Canadian Journal of Physiology and Pharmacology*, 50:328–332, 1972.

[126] P. Seshaiyer, F. P. K. Hsu, A. D. Shah, S. K. Kyriacou, and J. D. Humphrey. Multiaxial mechanical behavior of human saccular aneurysms. *Computer methods in biomedical engineering*, 4:281–289, 2001.

[127] P. Seshaiyer and J. D. Humphrey. A sub-domain inverse finite element characterization of hyperelastic membranes including soft tissues. *ASME Journal of Biomechanical Engineering*, 125:363–371, 2003.

[128] P. Seshaiyer and J. D. Humphrey. A sub-domain inverse finite element characterization of hyperelastic membranes including soft tissues. *Journal of Biomechanical Engineering-Transactions of the ASME*, 125:363–371, 2003.

[129] R. T. Shield. Inverse deformation results in finite elasticity. *Journal of Applied Mathematics and Physics (ZAMP)*, 18:490–500, 1967.

[130] R. Skalak. Growth as a finite displacement field. In D. E. Carlson and R. T. Shield, editors, *Proceedings of IUTAM Symposium on Finite Elasticity*, pages 348–355. Martinus Nijhoff, Hague, 1981.

[131] R. Skalak, G. Dasgupta, M. Moss, E. Otten, P. Dullemeijer, and H. Vilmann. Analytical description of growth. *Journal of Theoretical Biology*, 94:555–577, 1982.

[132] R. Skalak, A. Tozeren, A. P. Zarda, and S. Chien. Strain energy function of red blood cell membranes. *Biophysical Journal*, 13:245–264, 1973.

[133] K. P. Soldatos. On universal relations in orthotropic material subclasses. *International Journal of Engineering Science*, 46:306–324, 2008.

[134] M. Sonka, F. Zhao, H. Zhang, A. Wahle, A. Stolpen, and T. Scholz. Early detection of aortic aneurysm risk from 4-D MR image data. In *Computers in Cardiology, 2006*, pages 69–72, 2006.

[135] A. J. M. Spencer. The static theory of finite elasticity. *IMA Journal of Applied Mathematics*, 6(2):164–200, 1970.

[136] A. J. M. Spencer. Constitutive theory for strongly anisotropic solids. In A. J. M. Spencer, editor, *Continuum Theory of the Mechanics of Fiber-Reinforced Composites*, pages 1–32. springer, 1984.

[137] J. Stålhand. Determination of human arterial wall parameters from clinical data. *Biomechanics and Modeling in Mechanobiology*, 2009 (in print).

[138] J. Stålhand and A. Klarbring. Aorta in vivo parameter identification using an axial force constraint. *Biomechanics and Modeling in Mechanobiology*, 3:191–199, 2005.

[139] J. Stålhand, A. Klarbring, and M. Karlsson. Towards in vivo aorta material identification and stress estimation. *Biomechanics and Modeling in Mechanobiology*, 2:169–186, 2004.

[140] J. Staubesand. Anatomie der Blutgefäße. I. Funktionelle morphologie der arterien, venen und arterio-venösen anastomosen. In M. Ratschow, editor, *Angiology*, chapter 2, pages 23–82. Thieme, Stuttgart, 1959.

[141] H. J. Steiger, R. Aaslid, S. Keller, and H. J. Reulen. Strength, elasticity and viscoelastic properties of cerebral aneurysms. *Heart Vessels*, 5:41–46, 1989.

[142] M. M. Stringfellow, P. F. Lawrence, and R. G. Stringfellow. The influence of aorta aneurysm geometry upon stress in the aneurysm wall. *Journal of Surgical Research*, 42:425–433, 1987.

[143] W. Sun and M. S. Sacks. Finite element implementation of a generalized fung-elastic constitutive model for planar soft tissues. *Biomechanics and Modeling in Mechanobiology*, 4:190–199, 2005.

[144] W. Sun, M. S. Sacks, and M. J. Scott. Effects of boundary conditions on the estimation of the planar biaxial mechanical properties of soft tissues. *ASME Journal of Biomechanical Engineering*, 127:709–715, 2005.

[145] L. A. Taber. Biomechanics of growth, remodeling, and morphogenesis. *Applied Mechanics Review*, 48:487–545, 1995.

[146] K. Takamizawa and K. Hayashi. Strain-energy density-function and uniform strain hypothesis for arterial mechanics. *Journal of Biomechanics*, 20:7–17, 1987.

[147] R. L. Taylor. FEAP User Manual: v7.5. Technical report, Department of Civil and Environmental Engineering, University of California, Berkeley, 2003.

[148] M. Tóth, G. L. Nádasy, I. Nyáry, T. Kerényi, M. Orosz, G. Molnárka, and E. Monos. Sterically inhomogeneous viscoelastic behavior of human saccular cerebral aneurysms. *Journal Vascular Research*, 35:345–355, 1998.

[149] L. R. G. Treloar. The elasticity of a network of long chain molecules I. *Transactions of the Faraday Society*, 39:36–41, 1943.

[150] L. R. G. Treloar. The elasticity of a network of long chain molecules II. *Transactions of the Faraday Society*, 39:241–246, 1943.

[151] L. R. G. Treloar. Strains in an inflated rubber sheet, and the mechanism of bursting. *Institution of the Rubber Industry Transactions*, 19:201–212, 1944.

[152] L. R. G. Treloar. Stress-strain data for vulcanized rubber under various types of deformation. *Transactions of the Faraday Society*, 40:59–70, 1944.

[153] L. R. G. Treloar. Stresses and birefringence in rubber subjected to general homogeneous strain. *Proceedings of the Physical Society*, 60:135–144, 1948.

[154] L. R. G. Treloar. *The Physics of Rubber Elasticity.* Clarendon Press, Oxford, 3rd edition, 1975.

[155] L. R. G. Treloar. The mechanics of rubber elasticity. *Proceedings of the Royal Society of London, Series A*, 351:301–330, 1976.

[156] C. Truesdell and W. Noll. The non-linear field theories of mechanics. In S. Flügge, editor, *Handbuch der Physik*, volume Bd. 3/3. Springer-Verlag, Berlin, New York, 1965.

[157] H. Ujiie, K. Sato, H. Onda, A. Oikkawa, M. Kagawa, K. Atakakura, and N. Kobayashi. Clinical analysis of incidentally discovered unruptured aneurysms. *Stroke*, 24:1850–1856, 1993.

[158] H. Ujiie, H. Tachibana, O. Hiramatsu, A. L. Hazel, T. Matsumoto, and Y. Ogasawara et al. Effects of size and shape (aspect ratio) on the hemodynamics of saccular aneurysms: a possible index for surgical treatment of intracranial aneurysms. *Neurosurgery*, 45:119–130, 1998.

[159] H. Ujiie, Y. Tamano, K. Sasaki, and T. Hori. Is the aspect ratio a reliable index for predicting the rupture of a saccular aneurysm? *Neurosurgery*, 48:495–503, 2001.

[160] R. N. Vaishnav, J. T. Young, J. S. Janicki, and D. J. Ratel. Nonlinear anisotropic elastic properties of the canine aorta. *Biophysical Journal*, 12:1008–1027, 1972.

[161] K. C. Valanis and R. F. Landel. The strain-energy function of a hyperelastic material in terms of the extension ratios. *Journal of Applied Physics*, 38:2997–3002, 1967.

[162] T. J. Van Dyke and A. Hoger. A new method for predicting the opening angle for soft tissues. *ASME Journal of Biomechanical Engineering*, 124:347–354, 2002.

[163] R. van Mastrigt, B. Coolsaet, and W. van Duyl. Passive properties of the urinary bladder in the collection phase. *Medical and Biological Engineering and Computing*, 16(5):471–482, 1978.

[164] H. Vaughan. Pressurizing a prestretched membrane to form a paraboloid. *International Journal of Engineering Science*, 18:99–107, 1980.

[165] A. I. Veress, J. A. Weiss, G. T. Gullberg, D. G. Vince, and R. D. Rabbitt. Strain measurement in coronary arteries using intravascular ultrasound and deformable images. *Journal of Biomechanical Engineering*, 124:734–41, 2002.

[166] S. D. Waldman and J. M. Lee. Boundary conditions during biaxial testing of planar connective tissues: Part 1: Dynamic behavior. *Journal of Materials Science: Materials in Medicine*, 13:933–938, 2002.

[167] S. D. Waldman, M. S. Sacks, and J. M. Lee. Boundary conditions during biaxial testing of planar connective tissues: Part II: Fiber orientation. *Journal of Material Science Letters*, 21:1215–1221, 2002.

[168] H. Watanabe, K. Akiyama, T. Saito, and F. Oki. A finite deformation theory of intravesical pressure and mural stress of the urinary bladder. *The Tohoku Journal of Experimental Medicine*, 135(3):301–307, 1981.

[169] J. A. Weiss, R. D. Rabbitt, and A. E. Bowden. Incorporation of medical image data in finite element models to track strain in soft tissues. *SPIE*, 3254:477–484, 1998.

[170] J. A. Weiss, A. I. Veress, G. T. Gullberg, N. S. Phatak, Q. Sun, D. Parker, and R. D. Rabbitt. Strain measurement using deformable image registration. In G. A. Holzapfel and R. W. Ogden, editors, *Mechanics of Biological Tissue*, pages 489–501. Springer Berlin Heidelberg, 2006.

[171] D. O. Wiebers, J. P. Whisnant, T. M. Sundt, and W. M. O'Fallon. The significance of unruptured intracranial saccular aneurysms. *Journal of Neurosurgery*, 66:23–29, 1987.

[172] A. Wineman and M. Gandhi. On local and global universal relations in elasticity. *Journal of Elasticity*, 14:97–102, 1984.

[173] A. Wineman, D. Wilson, and J. W. Melvin. Material identification of soft tissue using membrane inflation. *Journal of Biomechanics*, 12:841–850, 1979.

[174] C. H. Wu and D. Y. P. Peng. On the asymptotically spherical deformation of arbitrary membranes of revolution fixed along an edge and inflated by large pressures - a nonlinear boundary layer phenomenon. *SIAM Journal of Applied Mathematics*, 23:133–152, 1972.

[175] T. Yamada. Finite element procedure of initial shape determination for rubber-like materials. Technical Report No. 20, Res. Lab. Eng. Mat. Tokyo Inst. Tech., 1995.

[176] W. H. Yang and W. W. Feng. On axisymmetrical deformations of nonlinear membranes. *ASME Journal of Applied Mechanics*, 37:1002–1011, 1970.

[177] T. Yasui, K. Sasaki, Y. Tohno, and T. Araki. Tomographic imaging of collagen fiber orientation in human tissue using depth-resolved polarimetry of second-harmonic-generation light. *Optical and Quantum Electronics*, 37:1397–1408, 2005.

[178] E. A. Zerhouni, D. M. Parish, W. J. Rogers, A. Yang, and E. P. Shapiro. Human heart: tagging with MR imaging–a method for noninvasive assessment of myocardial motion. *Radiology*, 169(1):59–63, 1988.

[179] X. Zhou and J. Lu. Inverse formulation for geometrically exact stress resultant shells. *International Journal for Numerical Methods in Engineering*, 74:1278–1302, 2008.

[180] X. Zhou and J. Lu. Estimation of vascular open configuration using finite element inverse elastostatic method. *Engineering with Computers*, 25:49–59, 2009.

[181] M. A. Zulliger, P. Fridez, K. Hayashi, and N. Stergiopulos. A strain energy function for arteries accounting for wall composition and structure. *Journal of Biomechanics*, 37:989–1000, 2004.

[182] M. A. Zulliger, A. Rachev, and N. Stergiopulos. A constitutive formulation of arterial mechanics including vascular smooth muscle tone. *American Journal of Physiology - Heart Circulatory Physiology*, 287:H1335–H1343, 2004.